A machine learning approach to identifying and classifying volcanic deposits

Myrto Niki Trouva

Delft University of Technology

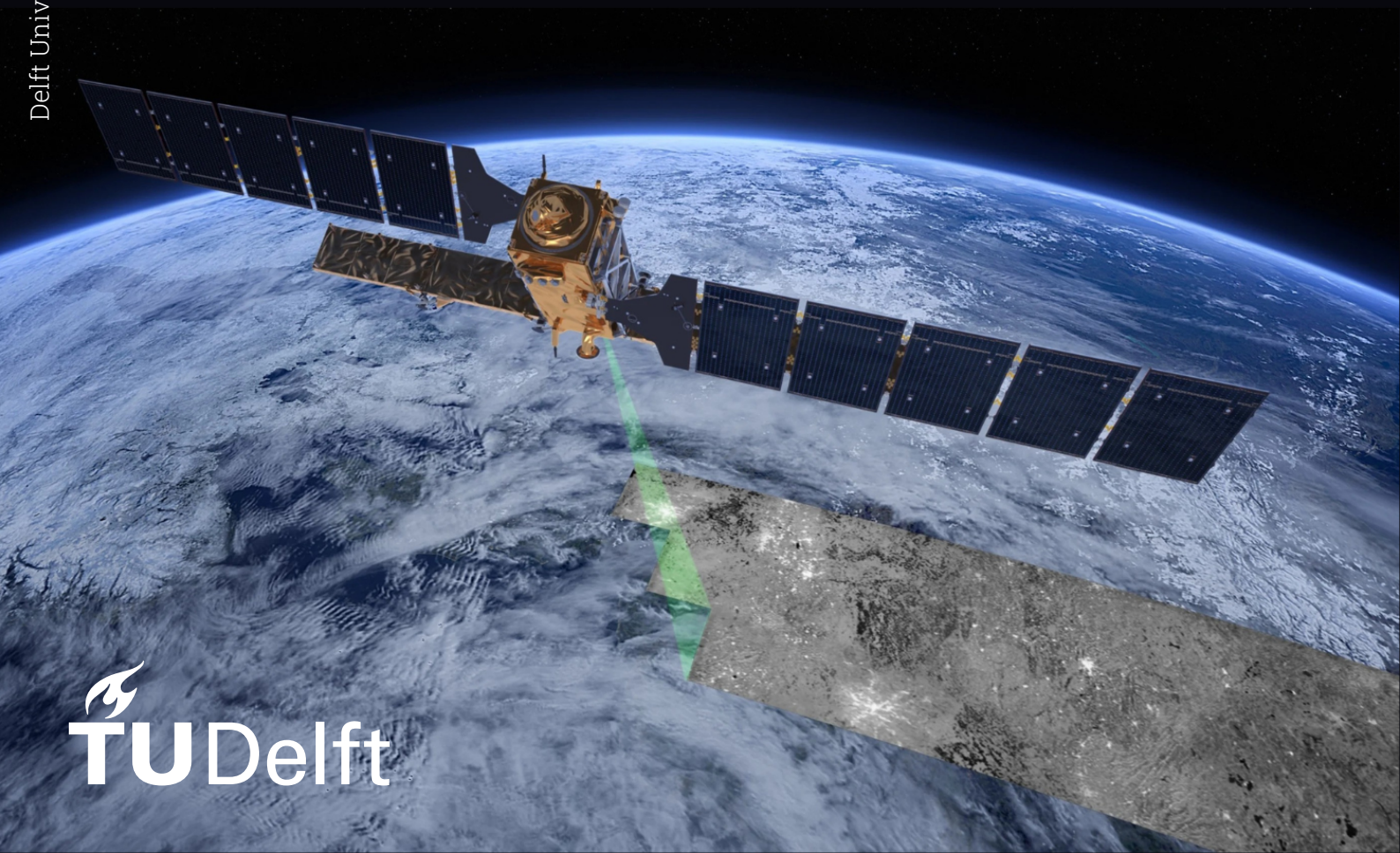

TU Delft

A machine learning approach to identifying and classifying volcanic deposits

by

Myrto Niki Trouva

Student Name	Student Number
Myrto Niki Trouva	5608090

Supervisor: P. Lopez Dekker
Committee: SJ de Vet, M.A. Schleiss
Faculty: Faculty of Applied Earth Sciences, Delft

TU Delft

Summary

The thesis develops a framework using exclusively Synthetic Aperture Radar (SAR) data to identify and classify volcanic deposits into Pyroclastic Density Currents (PDCs) and lava flows, which is crucial for planetary exploration where direct sampling is infeasible. Confirming the existence of PDCs on a planetary body provides insights into its geologic and atmospheric evolution, volatile content, and even potential for habitability.

The study uses high-resolution, dual-polarised Level-1 Ground Range Detected (GRD) SAR C-band imagery from the Sentinel-1 mission. Case studies from Sinabung (Indonesia), Fuego (Guatemala), Kilauea (Hawaii), and Nyiragongo (Congo) offer a diverse dataset.

The framework involves preprocessing steps suitable for highly variable topographic terrain, including calibration, despeckling, and radiometric and geometric corrections to produce reflectivity estimates in VV and VH polarisations. Texture features are derived using the Gray Level Co-occurrence Matrix (GLCM) method, including contrast, homogeneity, dissimilarity, and angular second moment (ASM). They are used as input to the first classifier alongside more straightforward metrics like polarisation ratio, Normalised Difference Index (NDI), and local variance. The first model distinguishes deposit pixels from the scene's background. The deposit pixels are further classified as PDCs or lava flows by an extreme gradient boosting classifier using the same features.

The models demonstrated high F1 scores, indicating a good balance between precision and recall, though both exhibited high RMSE. The first model's high RMSE (0.35) is not concerning for this application, considering an accurate outline is unnecessary. The second model's RMSE (0.42) coupled with a high False Negative rate (25%) reduces the method's reliability. Nonetheless, when tested on unseen data from Soufriere Hills (Montserrat) and Pahoa (Hawaii), the models produced accurate results with at least double the pixels correctly identified as their respective deposit type.

Including GLCM-derived texture features significantly enhanced accuracy, validating their use in volcanic deposit classification. This study's contributions to remote sensing in volcanology provide a foundation for understanding remote worlds. Future research could explore the impact of resolution on classification and test different texture measures as complementary or substitute features. Integrating part of the workflow into satellite firmware could enable near real-time monitoring and enhance hazard assessment and mitigation strategies.

Contents

1 Introduction

Volcanic activity plays a crucial role in shaping planetary surfaces, influencing atmospheres, and providing key insights into the internal processes of planets. By studying volcanic deposits, scientists can reconstruct the history of planetary bodies, understand the evolution of their interiors, and even predict future volcanic activity. Characterising the morphology and physical properties (e.g., grain size, density, componentry) of volcanic deposits such as lava flows, tephra and pyroclastic density currents (PDCs) is critical to gaining insights into the eruption dynamics and emplacement processes that formed these deposits [9], [23]. Such insight is essential for interpreting volcanic regions' historical and potential future activity.

> *"Distinguishing between different flow types contributes to the understanding of geodynamic processes taking place in the subsurface [33]."*

For instance, the presence of **PDCs** suggests high volatile content in the mantle released via volcanism; subsurface pressure and temperature conditions allow for the accumulation of these volatiles [64]. Effusive volcanism (**lava flows**) could indicate a mantle composition rich in basaltic magma, implying a lower gas content and higher fluidity.

Historically, volcanic monitoring has faced numerous challenges. From field missions to remote sensing, various techniques have been employed to track and analyse volcanic activities and mitigate associated risks [13], [76]. Deposit areas are typically extensive and can be difficult and dangerous to access due to eruptive activity, inaccessible terrain or other restrictive conditions, even long after an eruption has concluded [9]. While in-situ observations, when feasible, provide precise classification of volcanic deposits, they are often expensive and require significant time investment. Consequently, remote sensing has become a vital tool in volcanology, substantially enhancing our ability to study volcanic activity and deposits from a safe distance efficiently.

Optical sensors, such as those on GeoEye, WorldView, Quickbird, and Pléiades, are widely used for their high-resolution capabilities, providing sub-meter image pixels that are excellent for detailed surface observations on Earth [84]. However, when it comes to planetary bodies with thick atmospheres, like Venus, these sensors face significant limitations. Optical imaging is ineffective in such environments due to its inability to penetrate dense atmospheric layers and obstructions such as clouds, smoke, or ash; all commonly present in humid, tropical environments where many volcanoes are located [81].

Synthetic Aperture Radar (SAR) addresses these issues by collecting data regardless of time of day or lighting conditions, and most critically, it can penetrate thick atmospheres and other obstructions, making it *the only viable option* for observing the surface of planets like Venus [88].

In this context, previous studies have utilised several data sources and satellite or airborne missions, such as ALOS/PALSAR [84], COSMO-SkyMed (CSK) [22], multi-sensor unoccupied aerial systems (UAS), thermal infrared (TIR) cameras [9], and their combinations. Most

of the studies focus on detailed classifications of a *single* volcanic scene, analysing the various sub-types of lava or PDCs. However, this type of analysis can often lead to non-generalising models as they are case-specific and very localised. In their work, Dualeh et al. [22], created a semi-automatic classification method from backscatter imagery. However the results were significantly less accurate compared to a manual method. The discrepancies were especially prominent in smaller flows, due to the difficulty of distinguishing backscatter signals from surrounding noise. In addition, the classification of the outlines required a time-series of images - both before and after the eruption - in order to detect changes in the signal over-time which required repeat-pass acquisitions of the same area.

Identifying and classifying volcanic deposits remotely with limited information is the only option for planetary bodies where direct geological sampling is unfeasible. On Earth, geological fieldwork has allowed us to catalogue and understand the relationships between different types of volcanoes and their associated deposits. In contrast, extraterrestrial missions face significant logistical, technical, and financial challenges, with exponentially higher costs and complexities [15], [74]. Thus, accurately classifying volcanic deposits using remote sensing technologies like SAR becomes indispensable.

1.1. General Objectives

Recognising the limitations of multiple data sources in space missions, where bandwidth and payload capacities restrict data volume [82], this thesis presents a simplistic approach to classifying volcanic deposits. However, this simplicity is not a limitation; it is a strength. It aims to develop a framework based on a *single* source of information: **SAR image data**.

The primary research question addressed in this thesis is:

> *Can we identify and distinguish PDCs and lava flows on a planetary body using exclusively remote sensing SAR data?*

With sub-questions following the main research question:

- *Does the proposed framework indicate the presence of deposits in the scene?*
- *Is the resolution of Sentinel-1 SAR data sufficient for deposit classification?*

To address these questions, this work develops a framework which includes appropriate preprocessing steps and two binary classifiers based on SAR Sentinel-1 data. This approach maximises the utility of minimal information, ensuring the feasibility of deploying such techniques in planetary missions.

1.2. Broader Implications

The remote classification of volcanic deposits contributes to our understanding of a planet's geodynamic processes [72] without costly and technically challenging physical sample returns. It allows us to conduct planetary geology at a distance, opening up new possibilities for understanding extraterrestrial volcanism.

The discovery of *PDCs* on a planetary body, as discussed in NASA Technical Reports [33], signifies active or past volcanic activity and aids in understanding the planet's geologic and atmospheric evolution. Identifying *PDCs* can provide insights into the volatile content of the planet's magmas and the nature of past eruptions, which are vital to interpreting the planet's surface features and potential for habitability [32]. The relationship between habitability and volatile content is complex, with volcanic outgassing playing a crucial role in regulating planetary climates; for those interested in a deeper understanding, sources like [44], [99] and [52] provide further details. The ability to recognise and study such phenomena can also, refine our models of planetary evolution [12] and aid in selecting landing sites for future missions to ensure scientific value. Although atmospheric and environmental conditions may vary, within

the framework of comparative planetology, the findings of this study can be carefully extrapolated and applied to other planetary bodies with comparable characteristics to Earth, such as Venus.

2

Background Information

This chapter introduces the geomorphological characteristics of each deposit type observed on Earth. Although an in-depth evaluation of the deposits' physical properties is outside the scope of this study, I owe the reader a brief overview of their textural attributes to facilitate reading. The two main categories of volcanic deposits are PDCs and Lava Flows. These two deposit types are selected due to their distinct emplacement mechanisms and resultant surface morphologies, which are governed by physical properties such as viscosity, temperature, gas and particle content. Their differences manifest in surface roughness and texture, parameters effectively captured by SAR imaging.

2.1. Pyroclastic Density Currents

In the context of volcanology, PDCs are hot, fast-moving mixtures of gas and volcanic particles (ash and rock debris) that flow "hugging" the ground due to their higher density relative to the surrounding air and the influence of gravity [67], [61]. They extend until they run out of momentum. They typically originate from the collapse of eruption columns, lava domes, or lava flow fronts and explosive lateral blasts [21].

Subcategories of PDCs relevant to the context of this study are introduced below.

Block-and-Ash Flows (BAFs) Block-and-ash flows (BAFs) are a common type of PDC formed by the gravitational collapse of hot lava domes, lava lakes (molten or solidified lava in volcanic craters or depressions [80]), and perched pyroclastic debris [23]. These flows are characterised by a concentrated basal avalanche, which carries the bulk of the mass and momentum, overlain by a dilute turbulent ash cloud surge, making them a complex dense–dilute system [23]. A typical BAF deposit example is shown in Figure 2.1.

Figure 2.1: BAF deposit texture with angular and fractured andesite clasts from the Waiweranui unit, Maero Formation, Mt. Taranaki. Image retrieved from [30].

Lahars Lahars are a conglomerate of rock debris, mud and water that travel rapidly downslope under the influence of gravity [86]. They can progress through different phases with

varying water content. In all phases, the liquid portion supports the solid particles and enables the rapid movement of the flow down the volcano's slope [85]. Figure 2.2 shows a large lahar formation on the slopes of Mount Saint Helens.

Figure 2.2: Lahars at Mount Saint Helens. Image retrieved from [73].

Pyroclastic Surges and Pyroclastic Flows Pyroclastic flows are dense and contain a high concentration of solid volcanic fragments. Pyroclastic surges are more dilute, with fewer solid particles and more turbulent nature as depicted in Figure 2.3a. The lower concentration of fragments increases its mobility and allows for surmounting topographical features as indicated in Figure 2.3b. In both cases, the gas phase partially supports the solid particles, contributing to their high mobility [85].

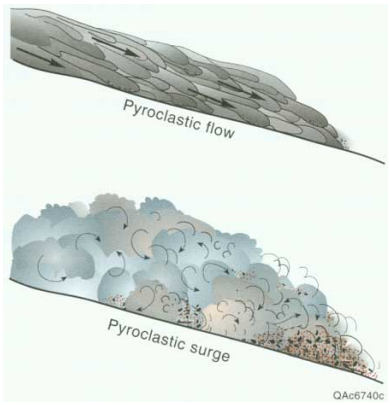

(a) Pyroclastic flow vs pyroclastic surge representation. Image retrieved from [78].

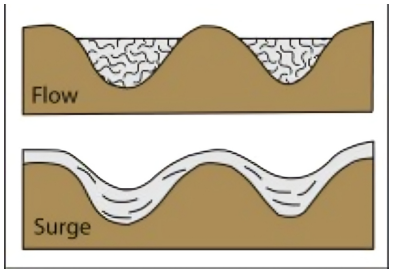

(b) Pyroclastic flow vs pyroclastic surge deposits. Image retrieved from [45].

Figure 2.3: Comparison of pyroclastic flow and surge.

Block or debris avalanches Block and debris avalanches are massive, gravity-driven volcanic rock, debris, and soil movements. They occur when the structural integrity of a volcanic flank collapses, often due to volcanic activity such as dome intrusion, phreatic explosions, or caldera wall slumping [1]. These avalanches consist predominantly of block facies and matrix facies and can travel at high speeds, picking up soil, stream gravels and wood, causing significant damage to the surrounding landscape [89].

- **Block facies:** Consist of coherent (solid, intact), unconsolidated (loose, uncemented, minor compaction or hardening) or poorly consolidated (partially compacted) volcanic fragments. They often retain their internal stratification and intrusive contacts [1].

- **Matrix facies:** Comprise of a mixture of volcanic clasts from the source volcano, typically poorly sorted, angular, highly fractured, often fitting together [1].

2.2. Lava flows

Lava flows are streams of molten rock (liquid), crystals (solids), gas (bubbles), and other voids that emerge from a volcano and solidify as they cool [43]. The temperature at which lava solidifies depends on its composition (approximately 800 degrees Celsius) [87]. This study considers three (3) primary types of lava flow subcategories.

Pāhoehoe Pāhoehoe lava flows exhibit smooth, glass-like surfaces, often characterised by folds called “ropes” and an undulating, “hummocky” or “billowy” topography. The surface texture may include small bumps and mounds due to the entrapment of crystals, and it produces a characteristic crunching sound when walked on due to the fragile glassy rind that spalls off [43]. The term “pāhoehoe” comes from the Hawaiian word “hoe,” meaning to paddle, which likely refers to the resemblance of the ropy texture of this type of lava to the swirling eddies created by paddle strokes in the water as shown in Figure 2.4. These flows form when lava erupts at a low rate and moves slowly over gentle slopes. Pāhoehoe flows can travel as sheets, through lava channels, or within lava tubes, often advancing as small lobes or toes that break out from the crust. Subtypes of pāhoehoe include smooth, ropy, hummocky, shelly, slabby, spiny, toothpaste, and entrail [79]. Several of these types are presented in Figure 2.4 and Figure 2.5.

(a) Ropy lava flow formed on La Palma, Canary Islands in 1949. This wrinkled surface is the result of the interior lava flow moving quicker than the exterior due to the difference in temperature. Image retrieved from [70].

(b) A close up image of Pāhoehoe rope lava with visible red-hot interior. Image retrieved from [79].

Figure 2.4: Examples of ropy pāhoehoe - the most well-known type, formed due to shear stress accumulation at the surface. The cooling crust is dragged downstream by the hot interior.

‘A‘ā ‘A‘ā lava flows have rough, jagged, or clinkery surfaces composed of angular, spiny fragments as shown in Figure 2.6. These flows are characterised by their irregular, sharp clasts of lava formed when the lava is too viscous or flowing too quickly to maintain a smooth surface [79]. Instead, it tears apart due to shear strain, creating a brecciated surface layer that encloses a coherent core [43]. They typically advance as sheets or within channels faster than pāhoehoe and are more common [79]. Figure 2.7 showcases an example of both ‘a‘ā and pāhoehoe formations.

Blocky Blocky lava flows, typically composed of andesitic and basaltic-andesitic materials, feature larger blocks than ‘a‘ā lava [70]. Their surface is smooth, lacking the rough, spiny texture of ‘a‘ā. Their shape is polyhedral with defined angles. Internally, they have a dense core, often rich in crystals or bands of obsidian and pumice. They are also distinguishable from ‘a‘ā due to their much higher thickness [43]. Examples of blocky lava flow deposits are presented in Figure 2.8.

(a) Basaltic pāhoehoe formation in Hawaii. Image retrieved from [70].

(b) Pāhoehoe lava formation after cooling in Hawaii. Image retrieved from [70].

(c) Pāhoehoe ”toes” on an active lava flow from Kīlauea Volcano in Hawaii. This sub-type rapidly cools down when exposed to the atmosphere. Image from [79].

(d) Texture example of spiny pāhoehoe lava. It forms from viscous lavas with gas bubbles. Location: Kīlauea, Hawaii. Image from [79].

Figure 2.5: Pāhoehoe lava flow types. Images retrieved from [79], [70].

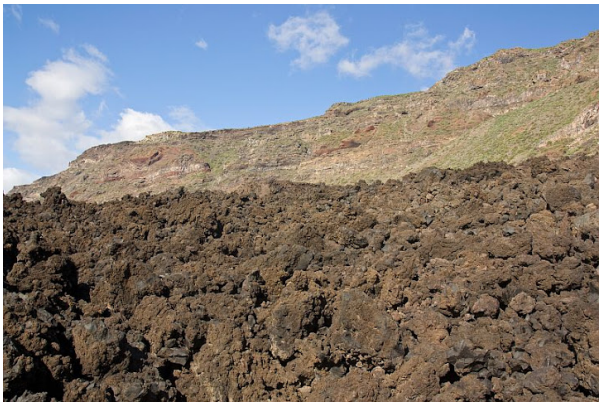

(a) ‘A‘ā lava in the foreground in La Palma, Canary Islands formed during the Cumbre Vieja eruption in 1712 [70].

(b) A close up view of ‘a‘ā showing the incandescent interior and the cooled rubbly,clinkery surface [79].

Figure 2.6: ‘A‘ā lava flow examples.

Figure 2.7: Both pāhoehoe and ‘a‘ā lava formations as seen in Hawaii. When the flow rates are high and the slopes are steep the formation of ‘a‘ā lava is favored. [70]

(a) Blocky lava at Nea Kameni (new burnt) island in the caldera of Santorini, Greece [70].

(b) A close up of blocky lava at Nea Kameni island in Greece [70].

Figure 2.8: Blocky lava flow can be tens of meters high with very large rock formations.

3
Data & Methods

This chapter outlines the overall approach developed to attain the study's objectives, which involves a preprocessing step and two classification pipelines. First, the case studies are presented in the context of their key physical properties that are relevant to the classification. Following this discussion, the data products selected for these cases are introduced, leading to a detailed explanation of the methods employed.

3.1. Case studies

There are four case studies used as input for classification. The selection is made to incorporate different lava and PDC subtypes to ensure diversity. In addition, since the operation year of Sentinel-1 is 2014, eruptions prior to that date were disconsidered.

3.1.1. Case Study 1: Sinabung Volcano, Indonesia

Mount Sinabung is an andesitic stratovolcano in the North Sumatra Province of Indonesia [54]. The phreatic eruption on August 27, 2010 [35], marked the beginning of Sinabung's first historical activity. The eruption was followed by a prolonged period of dome growth, lava flows, and frequent explosive events. Notably, major PDC events occurred in November 2016, with eight (8) recorded explosions and February 19, 2018, with the latter removing the summit lava dome [100], [65], [7]. An effusive eruption on January 31 2014, created a 100-meter-thick and three (3) km-long andesitic (blocky type) lava flow on the SE flank, which has remained prominently visible [7], [36].

The collected data for this location are from April 21, 2018, following an eruption that produced fresh PDCs reaching about 3.5 km down the SE flank. The outline includes avalanche blocks and fine-grained ashes embedded in between [37], [38]. This timing allows for assessing the freshly deposited materials without the interference of significant erosion or vegetation regrowth. It is worth mentioning that the thick lava flow of January 2014 is visible in the SAR image.

The unique coexistence of lava flows and PDCs within the same volcanic scene at Sinabung creates a layered geological structure that challenges and complicates classification. Due to the multiple eruptions taking place after the deposition of lava, the question is raised:

Should we consider the lava flow region as "lava," "PDC," or a new combined category?

In later sections, we will discuss the model's performance in each case. This volcano was specifically selected to examine the algorithm's performance in distinguishing complex volcanic scenes and diversifying the sub-types of PDC deposits, a critical step towards understanding volcanic behaviour and developing more accurate models.

The shapefiles with the outlines for this case were provided by Brett et al. [7]. The PDC outline was extended to incorporate additional pixels that were left out. Figure 3.1 illustrates both the original and revised outlines. Considering the limited PDC data points, incorporating these

additional pixels was crucial to enrich the dataset for training and validation purposes.

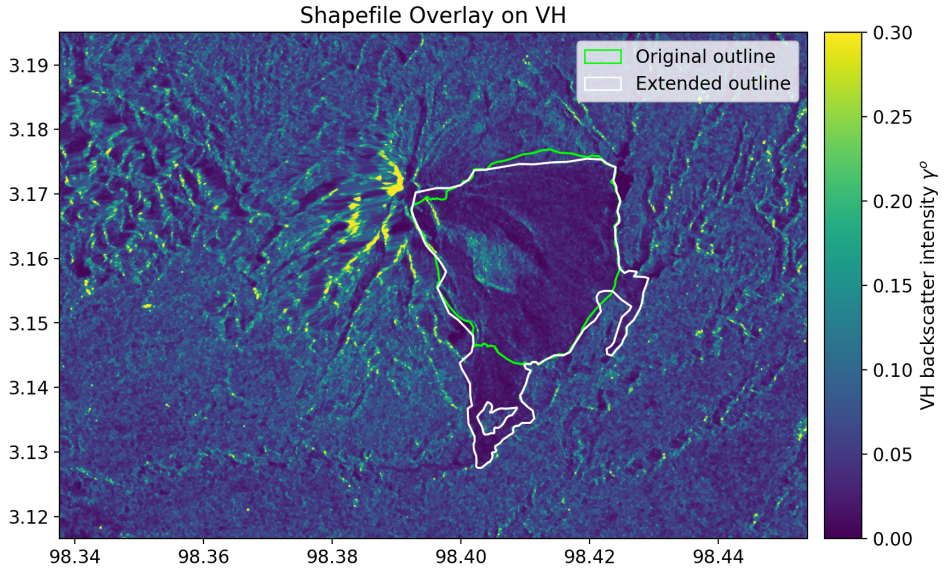

Figure 3.1: In light green, the original outline capturing a smaller part of the deposit. In white, additional patches of PDC areas are added.

3.1.2. Case Study: Fuego Volcano, Guatemala

Volcán de Fuego - Spanish for "Volcano of Fire", is a stratovolcano in Guatemala primarily producing basaltic and andesitic flows, with recent eruptions producing more mafic material, rich in silicate minerals or magnesium and iron [95]. Notable eruptions have produced pyroclastic flows, lahars and block avalanches [40]. This work examines the activity related to the major eruption on June 3, 2018, and subsequent minor eruptions in the following days. As observed in satellite data, multiple explosions generated an ash plume throughout the day, reaching 15.2 km in altitude [39]. Large pyroclastic flows descended several ravines on the volcano's flanks [10]. On June 5, additional explosions increased the number of pyroclastic flows and block avalanches, which travelled up to 1 km downslope [39]. Ash plumes and pyroclastic flow debris led to persistent ash clouds. Heavy rainfall starting June 6 led to over sixty (60) lahars that month, caused by the interaction of rain and freshly deposited volcanic material [22]. Figure 3.2 shows a SAR image depicting ground surface changes in the area.

Rainfall significantly influences radar backscatter properties by altering the moisture content of volcanic deposits. When the subsurface transitions from dry to wet, radar penetration decreases, and the radar signal reflects more from the near-surface scatterers, increasing backscatter intensity [22]. Sentinel-1 SAR data used in this study was carefully selected from June 8, 2018, to capture the deposits as fresh as possible before any significant erosion; however, rainfall events could alter the backscatter signals and, consequently, the accuracy of the classification.

Due to its clear and isolated PDC signatures, the Fuego scene presents an ideal opportunity for training models to distinguish PDCs from other volcanic deposits. A rough outline for this volcanic scene was provided by Dualeh et al. [22]. It was then carefully redrawn based on the mean of a collection of cloud-filtered Sentinel-2 images. This new outline improved data fidelity by closely adhering to the deposit boundaries and correcting the original contour, which included extraneous background pixels.

3.1.3. Case Study: Kilauea, Hawaii

The 2018 eruption of Kilauea, a shield volcano known for its gentle slopes and active history [71], was a significant event. Lasting from May 3 until August 9, this eruption saw a transition in

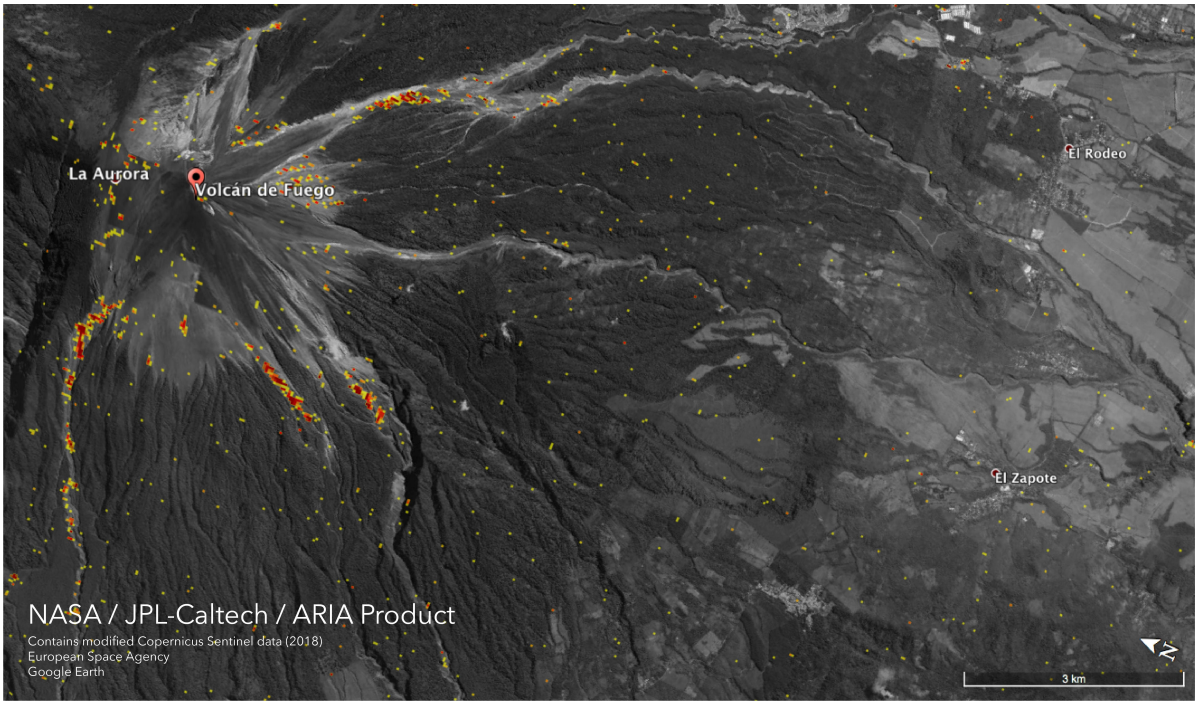

Figure 3.2: Damage map derived from SAR images by the Copernicus Sentinel-1 satellites (ESA), taken before (June 1, 2018) and after (June 7, 2018) the volcanic eruption. The map covers 91 by 21 km with each pixel representing about 30 meters. Color variation from yellow to red indicates increasing ground surface change. Image courtesy of NASA JPL [59].

lava composition from evolved basalt and andesite to more mafic basalt. This shift indicated a change in magma source from the rift zone to nearby magma reservoirs [24]. The high-temperature mafic lava, with its higher effusion rate, formed channelized pāhoehoe and ’a’ā lava flows [24], adding to the diversity of lava flow subtypes in the dataset.

The eruption produced over twenty (20) fissures and significant seismic activity, leading to large-scale magma drainage through the summit, rapid deflation, and extensive lava flows reaching the ocean [56]. The United States Geological Survey (USGS) carefully mapped the extent of the eruption and generated detailed shapefiles for the outline of each flow [93]. The data selected for this area are shortly after the last effusive activity on the 15th of August to avoid erosion and excessive rainfall compacting the deposit. The same scene contains lava flows from a past eruption that took place between June 2014 and June 2016, and they were used to test the accuracy of the model based on unseen data.

The outlines for the training data were retrieved from U.S. Geological Survey [93] and [92]. It is worth noting that older deposits in the (training) scene were included to enrich the dataset with more diverse lava flow points. Figure 3.3 shows the location of these older flows, which were subsequently integrated into the original outline.

3.1.4. Case Study: Nyiragongo, Democratic Republic of Congo

The eruption at Mt. Nyiragongo, an active stratovolcano in the Republic of Congo, took place on May 22, 2021, and shortly after, the Copernicus Emergency Management Service mapped it to analyse the lava and its impact [14]. The SAR image for this study is dated June 6, 2021. Basaltic lava flowed South through three (3) fissures near the lava lake present in the summit crater [34]. According to Innocent et al. [47] who performed a geochemical characterisation of the deposits, the 2021 eruption produced “ultrabasic” lava, highly alkalic with low magnesium, calcium and iron contents. Such alkaline, basic magma is rarely observed, making this an interesting case to diversify the portfolio of lava types. The type of lava flow produced during this eruption can be inferred from Figure 3.4, where one can recognise the rough, spiny texture

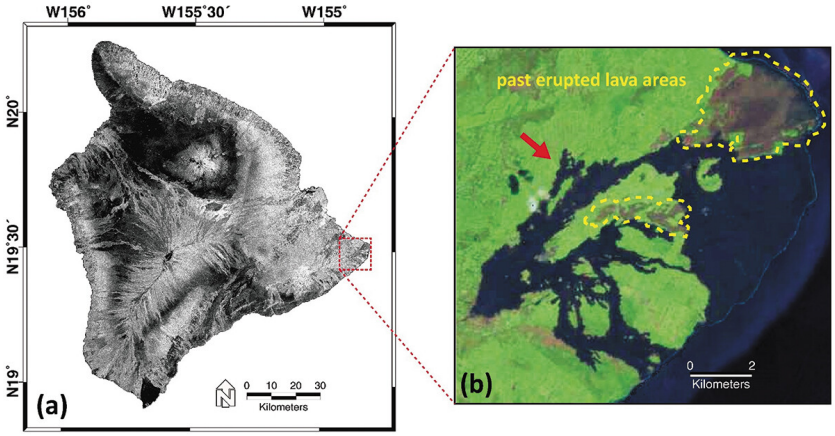

Figure 3.3: Map of Hawaii island (left). The dotted rectangle is the area of interest located in the East rift zone. The optical image on the right shows the lava flow area, with the yellow dotted polygons highlighting previously deposited lava [50].

with irregular shapes and sizes characteristic of ‘a‘ā lava. The GIS shapefiles for this event were retrived from Copernicus Emergency Management Service [14].

Figure 3.4: Nyiragongo eruption deposits as captured by The Washington Post [90].

3.2. Data

The data utilised in this research comprises Synthetic Aperture Radar (SAR) C-band imagery from the Sentinel-1 mission, a component of the Copernicus European joint initiative by the European Commission and the European Space Agency [2]. All images are obtained from the Alaska Satellite Facility (https://search.asf.alaska.edu/), specifically in Interferometric Wide (IW), high-resolution mode from Sentinel-1A.

Ground Range Detected (GRD) GRD data, categorised as Level-1 products, include a degree of pre-processing and present multi-looked backscatter intensity information projected to ground range using the WGS84 Earth ellipsoid model [97], [2]. The selected images feature dual polarisations, VV and VH. While the data of IW High Resolution are provided with a pixel spacing of 10 m x 10 m, the spatial resolution is 20 m x 22 m (range x azimuth).

3.3. Methodology

Sentinel-1 GRD data were preprocessed using the Sentinel Application Platform (SNAP), following a systematic workflow to ensure the data’s accuracy and reliability for further analysis. As mentioned earlier in this section, the information contained in the GRD product of each

scene is *amplitude*, A, and *intensity*, I, which are related by

$$I = A^2. \tag{3.1}$$

3.3.1. Preprocessing Workflow

Figure 3.5 is a block diagram that schematically depicts the preprocessing workflow. The final output includes γ_0, referred to as "gamma nought", in VV and VH polarisations. It represents a reflectivity estimate derived from radar brightness after calibration and radiometric corrections. For clarity, and because some of the readers might not be familiar with these terms, an explanation of the different reflectivity estimates is given in Figure 3.6, where it is visible that σ_0 and γ_0 are trigonometric transformations of radar brightness (β_0).

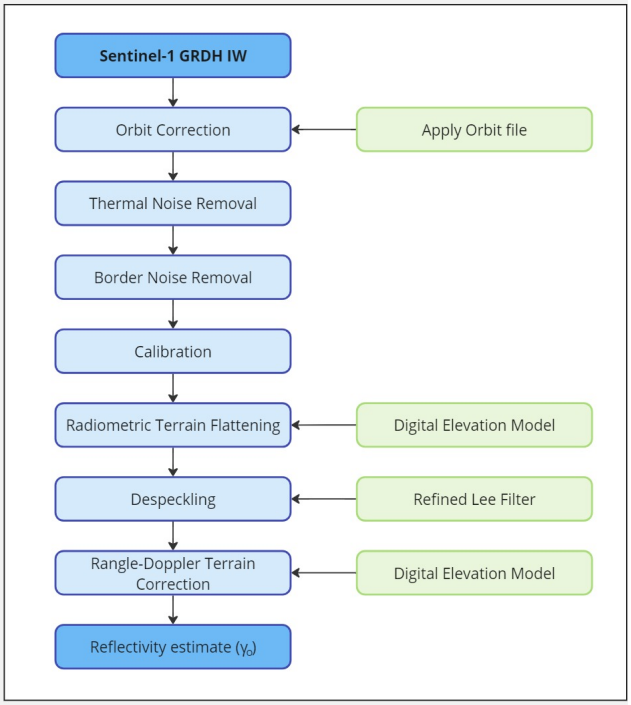

Figure 3.5: Block diagram of the preprocessing workflow.

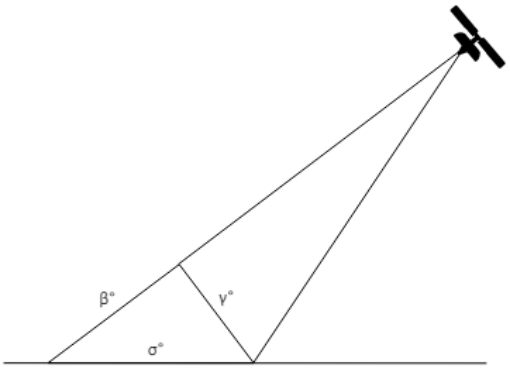

Figure 3.6: Brightness expressions for radar backscattering. The most common backscattering term for geoscientists is σ_0. γ_0 and σ_0 are reflectivity estimates and they differ in the way they are normalised. Image from [66].

Specifically, σ_0 measures the mean reflectivity of a patch of distributed scatterers per unit area of a horizontal surface, measured along the ground range. On the other hand, γ_0 represents the reflectivity of distributed scatterers per unit area of the incident wave front and has the

advantage of maintaining relatively constant reflectivity over a wide range of incident angles for rough surfaces [66]. To make it clear, Figure 3.7 illustrates the definitions of ground range and incident angle. Therefore, the calibrated backscatter values γ_0 are used throughout this study to represent backscatter intensity.

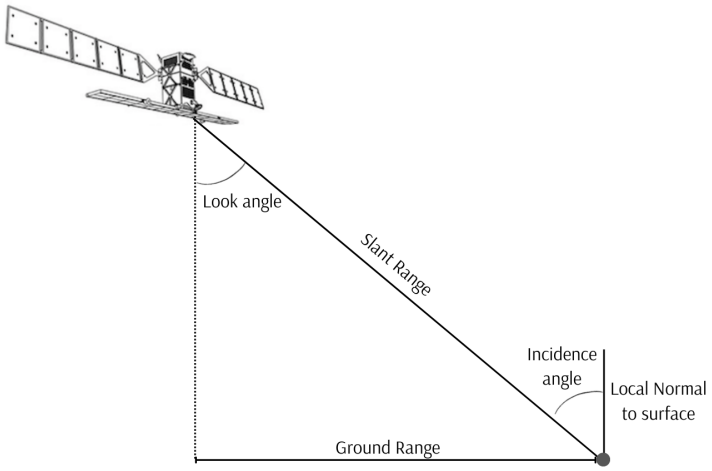

Figure 3.7: Definition of some common terms in SAR.

1. Orbit Correction

This step involves updating the satellite's orbit information to ensure accurate geolocation through orbit state vectors stored in the metadata of the GRD product [28].

2. Thermal Noise Removal

Thermal noise is inherent in radar systems and can be pronounced in images with low intensities, especially in cross-polarisation channels [5]. It is present in all electrical systems, caused by the random motion of charge carriers (most typically electrons, or electron holes) regardless of any applied voltage and increases proportionally with temperature [63]. Practically, in SAR imaging, thermal noise can affect the quality of the images. The noise appears as random variations in the brightness or pixel values.

3. Border Noise Removal

Radiometric artefacts, which affect the edges of the SAR image, are removed to prevent them from affecting the analysis. The operator in SNAP removes low-intensity noise and invalid data at the border [28].

4. Calibration

Calibration converts the pixel values to backscatter coefficients (σ_0, γ_0 and β_0). This step ensures the data reflect only the true backscatter intensity from the Earth's surface. In β_0, the influence of the incidence angle is still present [27]. For this study, β_0 is selected as an output of this operator and it is calculated as

$$\beta^0 = \frac{\mathrm{DN}^2}{\mathrm{LUT}_{\beta^0}} \quad , \tag{3.2}$$

where LUT_{β^0} is the calibration vector available in the annotation files of the Sentinel-1 product and DN is the pixel *Digital Number*; in the case of GRD products it represents the pixel amplitude found in the measurement file [26].

5. Radiometric Terrain Flattening

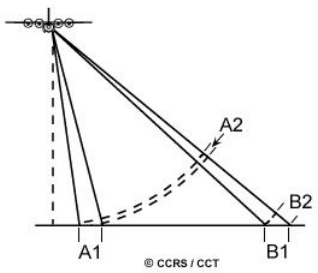

Figure 3.8: Slant range distortion representation. Inspite A1 and B1 targets having the same size on the ground, their apparent dimensions, as seen by the radar, (A2 and B2) are different. Image courtesy of Natural Resources Canada [60]

This step corrects for radiometric distortions caused by terrain variations, resulting in γ_0 and σ_0 values that are more accurate for hilly or mountainous areas. The Terrain Flattening operator in SNAP utilises an algorithm by Small [83], which does not use the (local) incidence angle but the area illuminated by the sensor of each pixel. Correcting the angles prior to this step could lead to overestimating the influence of the surface orientation towards the sensor [27], thus the angles are calibrated to β_0 prior to this step.

6. Despeckling

This step reduces speckle - a granular, noise-like signal inherent to SAR images and any coherent source. Speckle arises from the constructive and destructive interference of the coherent radar signal, resulting in a grainy appearance that can obscure fine details in the data and reduce interpretability [66]. This workflow employs the Refined Lee filter with a 7x7 pixel window to mitigate its effect. The resulting images have improved radiometric resolution at the expense of spatial resolution [49]. The choice of the particular window size is due to its commonality in SAR image processing, because it provides sufficient neighbourhood information to effectively reduce speckle while minimising the loss of spatial resolution.

7. Range-Doppler Terrain Correction

This step corrects geometric distortions caused by the side-looking (slant) radar geometry, using a Digital Elevation Model (DEM) to accurately geocode the data. Radar imagery suffers from geometric distortions due to its viewing geometry and the radar's nature as a distance-measuring device, causing slant-range scale distortion and varying image scale from near to far range as depicted in Figure 3.8. Additionally, the presence of hills and valleys can introduce geometric shifts known as foreshortening, layover, and radar shadow. Range-Doppler Terrain Correction addresses these issues by shifting all pixels to their correct locations according to an input DEM, ensuring accurate ground-range representation. [25], [3], [60].

3.3.2. Classification

The classification approach encompasses a two-step strategy designed to improve accuracy in classifying volcanic deposits. This strategy involves the construction of two separate models:

- **Model 1:** This model classifies pixels as either *deposit* or *background*.
- **Model 2:** This model further classifies the deposit pixels and distinguishes between the two types: *PDCs* and *lava flows*.

This sequential method reduces the overall decision space and minimises the potential for "confusion" between classes. Isolating the deposit pixels from the background reduces the complexity of the overall classification task. When trialling the implementation of a single model with three classes (lava flows, PDCs and background), many PDC pixels were misclassified as background, adding to the motivations for adopting the two-step approach.

Implementation Both models are implemented in Python. The exact selection of parameters can be found in the Appendix A.

Model 1	Model 2
Classifier: Random Forest **Library:** Scikit-learn [16] **Function:** For a detailed explanation of how a Random Forest classifier works, the reader can study the overview given by Belgiu and Drăguț [6].	**Classifier:** Extreme Gradient Boosting **Library:** XGBoost [20] **Function:** Wade and Glynn [96] provide more information on extreme gradient boosting.

Table 3.1: Model selection for each step and libraries used to implement them in Python.

Motivation for model choices The particular setup was selected based on performance and practical considerations:

- Random Forest performed well in distinguishing between background and deposit pixels due to its ability to handle large feature spaces and capture complex patterns. However, its computational cost made it less suitable for the second step, considering that more adjustments were necessary to achieve satisfactory performance.
- Extreme gradient boosting was preferred for the second step due to its computational efficiency and ease of tuning without overfitting. These traits were important for handling the more refined task of distinguishing between PDCs and lava flows.

Alternatives A single decision tree for Model 1 was considered, but it could not sufficiently differentiate between deposits and background. Convolutional Neural Networks (CNNs) were considered for Model 2 due to their potential to capture the complex relationships between lava flow and PDC textures. However, due to data limitations (only four images would not suffice for such methods), an implementation was not attempted.

Feature Extraction

The model considers various *basic* features computed exploiting both the VV and VH polarisations, as well as a set of features representing texture utilising the Gray Level Co-occurrence Matrix (GLCM) concept as described in [57]. Rodrigo et al. [69] have also used GLCM texture features for land cover classification, where a high level of accuracy was achieved, confirming the value of this method. In both cases, the authors use GLCM to compute and create a texture characteristics map of the original γ_0 images in VV and VH.

***Basic* features** The first two (2) features are the γ_0 VV and VH channels, based on which the following four (4) features are calculated.

- **Polarisation ratio:** This ratio helps identify the terrain's scattering mechanisms and surface roughness characteristics. Higher ratios typically indicate increased surface roughness or volume scattering, which is common in areas with dense vegetation or rough surfaces. Computed as shown in (3.3).

$$\text{Pol Ratio} = \frac{\gamma_{0,\text{VH}}}{\gamma_{0,\text{VV}}} \tag{3.3}$$

- **Normalised Difference Index (NDI):** This index highlights the relative difference between the VV and VH polarisations, providing insights into surface properties and structure. A higher NDI value indicates a greater difference between the polarisations, often

corresponding to more distinct surface features. Calculated using the formula provided in (3.4).

$$\text{NDI} = \frac{\gamma_{0,\text{VV}} - \gamma_{0,\text{VH}}}{\gamma_{0,\text{VV}} + \gamma_{0,\text{VH}}} \tag{3.4}$$

- **Local Variance:** Calculated separately for the VV and VH channels using a 4x4 moving window approach. This feature measures the spread or dispersion of pixel values within the window. In this study, local variance is calculated using a *smooth* function [91]. This function smooths the data using a convolution with a specified window. It computes the weighted sum of the data points at each position. It effectively performs moving average smoothing, which aids in reducing noise and highlighting underlying trends in the data. Mathematically, the mean of the squared pixel values and the square of the mean pixel values are calculated for each window and polarisation. The local variance is then given by the difference between the two quantities as shown in (3.5).

$$\sigma^2_{\text{local}} = \overline{\gamma^2} - (\bar{\gamma})^2 \tag{3.5}$$

Lastly, the normalised local variance is expressed by:

$$\sigma^2_{\text{norm}} = \frac{\sqrt{\sigma^2_{\text{local}}}}{\bar{\gamma}}, \tag{3.6}$$

where $\bar{\gamma}$ is the average pixel value in the specified window as calculated through the *smooth* function.

***GLCM* features** The Gray Level Co-occurrence Matrix (GLCM) is a statistical method used to examine the spatial relationship between pixels in an image. It represents how often pairs of pixels with specific values and spatial relationships occur within an image or sub-image [48], [57], [69]. Using the GLCM, one can derive *texture feature maps*. These texture features are critical for representing the complex surface properties of volcanic deposits and can help enhance classification accuracy [69]. This directly ties back to the physical properties of lava flows and PDCs discussed earlier, as the texture features captured by GLCM are influenced by factors such as surface roughness and composition. By selecting case studies with diverse volcanic deposit types, the analysis leverages these GLCM-derived features to improve the accuracy of distinguishing between different volcanic surfaces.

In the 1970s, Haralick, Shanmugam, and Dinstein [42] systematised most of the GLCM texture calculations used in Remote Sensing. They proposed fourteen different measures and recommended calculating them in four directions and using each measure's mean and range in classification problems. Directionality has not been widely applied, with most researchers opting for a single, "invariant" spatial direction as the average of the four [41], inline with the suggestions of the authors. This study makes use of four texture features: contrast, homogeneity, dissimilarity, and angular second moment (ASM). A detailed description on the computation of the GLCM and the extraction of features is provided in Appendix B.

An integral part of the workflow is the normalisation method applied to the γ_0 VV and VH images used as input for the GLCM calculations. For this application, the images were normalised based on an *Equal Probability Quantisation* approach described in detail in Appendix B. The rationale behind this non-trivial choice is explained here.

Haralick, Shanmugam, and Dinstein [42] highlighted a general challenge in grey-tone normalisation of images: *texture is independent of tone*. For instance, an image might depict the same texture in different tones, as shown in Figure 3.9. While humans can easily recognise

the similarity in texture despite tonal differences, a machine would either need the images to be probability quantised (not just quantised) to derive the GLCM and its features, or the features themselves to be invariant under monotonic grey-tone transformations. ASM is one such invariant feature, whereas contrast, dissimilarity, and homogeneity are sensitive to overall brightness or contrast changes. Specifically, monotonic transformations, whether linear or non-linear, preserve the order of pixel intensities and consequently the probabilities of occurrence in the GLCM are preserved too. ASM is calculated based on the squared probabilities which is why it remains invariant under these transformations. In summary, unless the input image is probability quantised or normalised in such a way so that the distribution of intensities is considered, most texture features are not invariant to monotonic grey-tone transformations.

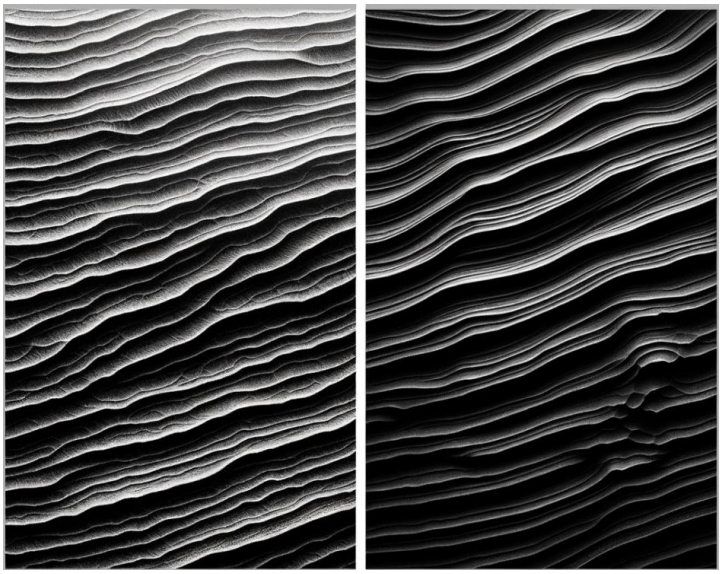

Figure 3.9: The image on the left is developed with light and thin tones, while the image on the right consists of dark and heavy tones. Despite the differences in tone, the texture pattern of the lines remains the same in both images. This illustrates how texture can be invariant to monotonic grey-tone transformations. Images created using chatGPT 4o.

Moving Window Approach

A moving window approach is used to apply the GLCM features across the entire image. A window of predefined size (e.g., 3x3, 5x5 pixels) ”slides” across the image, and the GLCM and subsequent texture features are computed for each window position. The results are *texture feature maps* representing each feature’s spatial distribution across the image. For this work, a window size 5x5 was selected, representing a 2500 square meter area. The window size choice strikes a balance between capturing detailed local textural variations, while maintaining computational efficiency.

In total, the reader is now familiar with ten features, all of which are used in both models along with their respective logarithmic transformation to account for the wide range of values and enhance the model’s sensitivity to minor variations.

Training the models

The models were trained using all features described in the previous paragraphs as input. In the first model, pixels were labelled as *deposit* if they fell within the outlined areas. In the second model, they were further labelled according to their case study as *lava* or *PDC*. To ensure data fidelity, in some cases, a subset of the background pixels was pre-selected to exclude small patches or streams of deposits not captured by the outlines. For example, Figure 3.10 illustrates an optical image of Volcán de Fuego layered with a red outline encapsulating the fresh 2018 deposits. One can discern that the outline does not include the smaller streams downhill of the mountain nor the older deposits at the top near the crater.

The output of Model 1 is a *binary classification map* where each pixel is labelled as either *deposit* or *background*. The identified deposit pixels are further classified by Model 2 into *lava* or *PDC*, resulting in a *a refined classification map* as the final output of the overall framework.

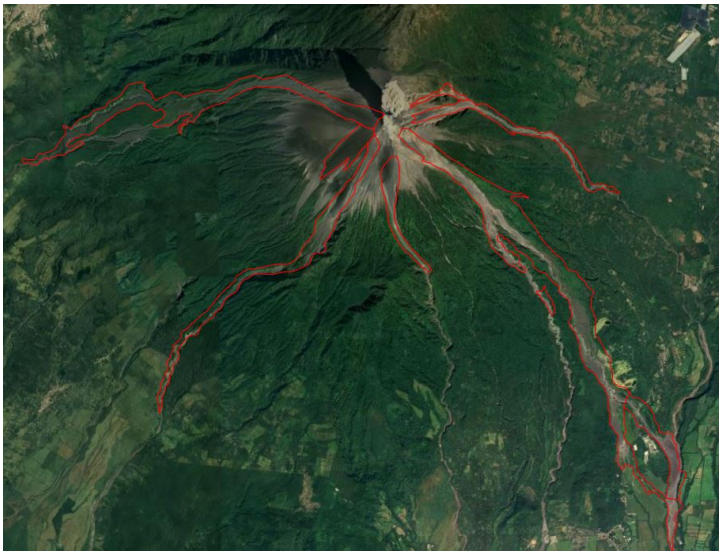

Figure 3.10: Optical image of Volcán de Fuego overlayed with the rough outline. Smaller streams of PDC runouts are not included.

Balancing the datasets

Due to the high imbalance between the classes, each model's pipeline includes a sampling strategy.

- **Oversampling:** SMOTE (Synthetic Minority Over-sampling Technique) was applied to the minority classes (*deposit* and *PDC* pixels) of both models.
- **Undersampling:** The majority class (*background* pixels) of Model 1 was under-sampled in order to match the number of pixels in the minority class [46]. In total, one million values for each class were considered.
- **Pipeline Setup:** The resampling techniques were incorporated into a pipeline to ensure a balanced training set. Using a pipeline is particularly useful when performing cross-validation methods. It ensures that the resampling steps are performed within each cross-validation fold, leading to a more robust model performance evaluation.

Performance metrics

Selecting the appropriate performance metrics is a nontrivial task and a critical factor in evaluating the quality of a classifier. The scientific community consenses that one should select those metrics according to the specific criteria of their application; however, those requirements might not be known in advance [101]. Yangguang et al. [101] performed a statistical analysis using Pearson linear correlation and Spearman rank correlation to explore the relationship among widely employed metrics. They categorise the metrics into three groups: threshold, probability and rank metrics. Table 3.2 shows the different metrics, their calculation and grouping. An explanation of the variables is provided below:

- **TP**: True Positives - the number of correctly predicted positive instances.
- **TN**: True Negatives - the number of correctly predicted negative instances.
- **FP**: False Positives - the number of incorrectly predicted positive instances.
- **FN**: False Negatives - the number of incorrectly predicted negative instances.
- **M**: Total number of instances (positive and negative).

- P_0: Prediction accuracy of a classifier - the proportion of times the classifier correctly predicts the true class.
- P_e: Agreement probability due to chance - the proportion of times that agreement is expected by chance.
- **Precision**: The ratio of correctly predicted positive observations to the total predicted positives expressed as $\frac{TP}{TP+FP}$.
- **Recall**: Represents how accurately the model identifies the positive class and it is expressed as $\frac{TP}{TP+FN}$.
- y_i: Actual (true) value for instance i.
- $\hat{y}_i$: Predicted value for instance i.
- **N**: Total number of negative instances (FN and TN).

According to their findings, metrics within the same category are highly correlated, while metrics from different categories are not as strongly correlated. Hence, when evaluating a classifier, it is advisable to select multiple metrics, ensuring that at least one is chosen from each category, especially if the specific evaluation criteria are not predetermined. Additionally, they conclude that it is not critical for a classifier to achieve optimal performance across all metric categories. Instead, as long as the classifier meets the performance requirements for the application as measured by certain groups of metrics, it is recommended to adopt it even if its performance in other metric groups is less satisfactory.

Table 3.2: Performance Metrics with Calculation Methods

Category	Metric	Calculation Method
Threshold Metrics	Accuracy	$\frac{\mathrm{TP+TN}}{\mathrm{M}}$
	Kappa Statistic	$\frac{\mathrm{P_0-P_e}}{\mathrm{1-P_e}}$
	F-Score	$2 \cdot \frac{\mathrm{Precision \cdot Recall}}{\mathrm{Precision+Recall}}$
Probability Metrics	Mean Absolute Error (MAE)	$\frac{1}{\mathrm{M}} \sum_{i=1}^{M} \lvert y_i - \hat{y}_i \rvert$
	Root Mean Square Error (RMSE)	$\sqrt{\frac{1}{\mathrm{M}} \sum_{i=1}^{M} (y_i - \hat{y}_i)^2}$
Rank Metrics	Area Under the ROC Curve (AUC-ROC)	$\int_0^1 \mathrm{Recall} \times d(\frac{\mathrm{FP}}{\mathrm{N}})$
	Area Under the PR Curve (AUPRC)	$\int_0^1 \mathrm{Precision} \times d(\mathrm{Recall})$

Considering the above and that the important class for this application is the minority class, this study explores a variety of metrics, focusing on f-score, RMSE, AUC-ROC and AUC-PRC. In order to not exclude the most widely used metric (i.e., accuracy), it is calculated and presented in the results section; however, alone, it is not a reliable metric for this application because it can be biased towards the majority class [53].

In addition to the performance metrics described here, there are more tools one can leverage to assess the quality and performance of a machine learning model. For this work, those are: the confusion matrix, tree depth analysis, feature and permutation feature importance and k-fold cross-validation.

Confusion Matrix The confusion matrix is a typical tool used in machine learning to visualize a model's behaviour in supervised classification. For binary classification, the matrix is a 2 x 2 matrix that provides a detailed breakdown of the model's performance by showing the counts of true positive (TP), false positive (FP), true negative (TN), and false negative (FN) predictions [8].

Tree Depth Analysis Tree depth analysis involves examining the depths of individual trees. The average tree depth indicates the complexity of the model, while the distribution of tree depths provides insight into the diversity of the trees. Tree depth affects model flexibility, with deeper trees fitting more complex functions and improving training set performance. Nevertheless, this could lead to overfitting and reduced generalization on the test data. Increasing depth decreases bias while increasing variance; random forests mitigate this increase by averaging multiple trees, though they are still susceptible to overfitting [11]. It is worth mentioning that in the context of machine learning, bias refers to the error introduced by false assumptions of the algorithm, which can cause it to miss relevant patterns and underfit the data. Variance, on the other hand, captures how sensitive the model is to small fluctuations in the training data, which can lead to overfitting.

> This concept gives rise to the well-known "bias-variance tradeoff," where increasing model complexity reduces bias but increases variance, and vice versa.

The challenge in model development is finding the optimal balance between bias and variance, ensuring that the model is complex enough to capture the underlying patterns in the data without overfitting the noise and specificities of the training set [98].

Feature Importance Feature importance measures the contribution of each feature to the model's predictions. It is calculated by averaging the decrease in impurity across all trees using the Gini splitting index [17]. This tool identifies the most influential features, providing insights into the factors that most affect deposit classification.

Impurity-based feature importance can be misleading in several situations, mainly when dealing with high cardinality features. Considering that our dataset contains many unique values within a feature space, another metric, called *permutation feature importance*, can support our understanding of which features play a significant role in constructing the model. It works by shuffling the values of each feature and noting the change in the model's score; this indicates how much the model relies on that feature [18], [19]. The score metric used is the *f1-score* for all the reasons discussed earlier in this section.

K-fold cross validation It is a resampling procedure used to detect overfitting by assessing how the results of a statistical analysis will generalise to an independent dataset [29]. It also supports robust model selection and hyperparameter tuning. The general procedure is the following:

1. Random shuffling of the dataset.
2. Split into k-amount of groups (folds) of approximately equal size.
3. For each group:
    - Use the group as validation (test) dataset.
    - Use the remaining (k-1) groups as training datasets.

- Fit a model on the training set and evaluate on the validation.
- Calculate the evaluation score (performance metrics).

4. Aggregate the k-scores to get a single estimate of the model's performance. This involves computing their mean and standard deviation to understand not only performance but consistency, too [29].

4

Results

The initial phase of this study involved preprocessing the raw Ground Range Detected (GRD) data from Sentinel-1 to mitigate various sources of noise and distortions, as outlined in chapter 3. Intermediate preprocessing results are omitted as they fall outside the primary scope of this work. This chapter introduces the case studies, detailing the feature images (*basic* and *GLCM*) employed in model training. Additionally, the classification outcomes and performance metrics for each model are presented.

Figure 4.1 provides an overview of the four case study areas, with deposit outlines overlayed on each. Red polygons delineate the deposit regions used for training the models, while the blue outline in Figure 4.1b highlights the old lava flow that is still visible today, as previously discussed.

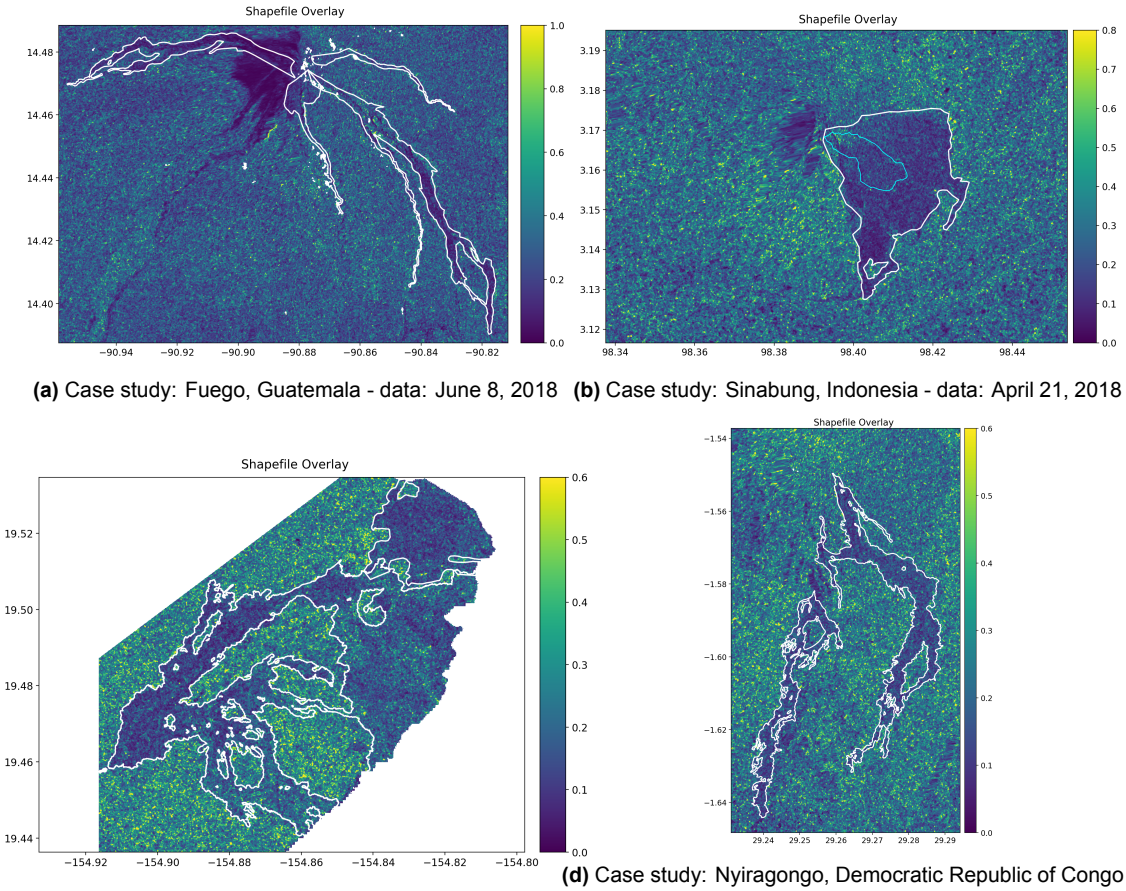

(a) Case study: Fuego, Guatemala - data: June 8, 2018 **(b)** Case study: Sinabung, Indonesia - data: April 21, 2018

(c) Case study: Kilauea, Hawaii - data: August 15, 2018 **(d)** Case study: Nyiragongo, Democratic Republic of Congo - data: June 6, 2021

Figure 4.1: Deposit outlines overlayed on polarisation ratio maps for each volcanic scene. Note the difference in colormap scales. (a) PDC deposit on Volcán de Fuego; (b) PDC deposit and the older lava pertaining to the 2014 eruption on Mt. Sinabung; (c) Kilauea, Hawaii with the lava flow outline of the 2018 eruption and older lava flows; (d) Lava flow deposit on Nyiragongo.

4.1. Basic Features

Figure 4.2, Figure 4.3, Figure 4.4 and Figure 4.5 explore each case in more detail, illustrating the six *basic* features: $\gamma_{0,\mathrm{VV}}$, $\gamma_{0,\mathrm{VH}}$, NDI, Polarisation Ratio, and Local Variance. The VV polarisation images generally exhibit low contrast, making it difficult to discern the deposit outlines, except in the Sinabung case (Figure 4.3a), where the old lava flow is distinctly visible and prominent compared to the PDC.

In contrast, the VH polarization images provide superior segregation of deposits from the background in all cases. However, finer details and smaller deposits tend to be less distinct (e.g., Figure 4.2b). The NDI and polarisation ratio images offer enhanced contrast between background and deposit pixels, where one can easily discern the outlines. Notably, in the Sinabung case (Figure 4.3c, Figure 4.3d), the lava flow becomes indistinguishable from the PDC, verifying the challenge in differentiating deposit types using these first-order texture measures.

Lastly, the local variance maps capture distinct patterns in the PDC scenes - for instance, in Figure 4.2f and Figure 4.3f, highlighting areas of significant variation. Contrariwise, they do not reveal clear deposit patterns in the lava flow scenes. Despite this apparent lack of information, this distinction is informative. The absence of discernible patterns in the lava flow areas might still contribute valuable information, especially in the second model, which aims to distinguish between the two deposit types. The presence of patterns in the PDC scenes versus the absence of such patterns in the others can be a critical distinguishing feature for accurate classification.

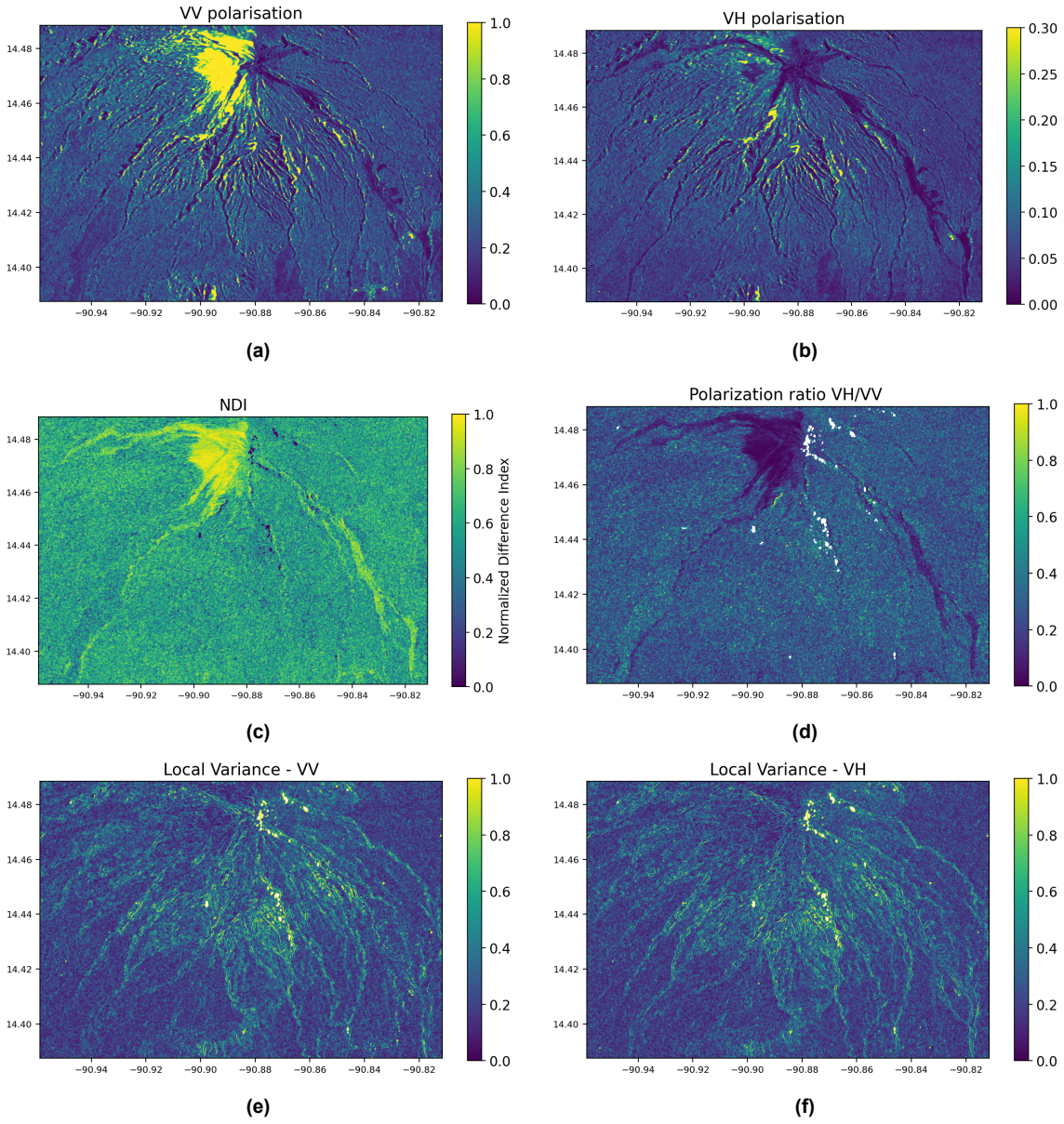

Figure 4.2: Fuego case study site *basic* features. (a) VV polarisation γ_0; (b) VH polarisation γ_0; (c) Normalised Difference Index (NDI); (d) Polarisation ratio; (e) and (f) local variance calculated based on VV and VH, respectively.

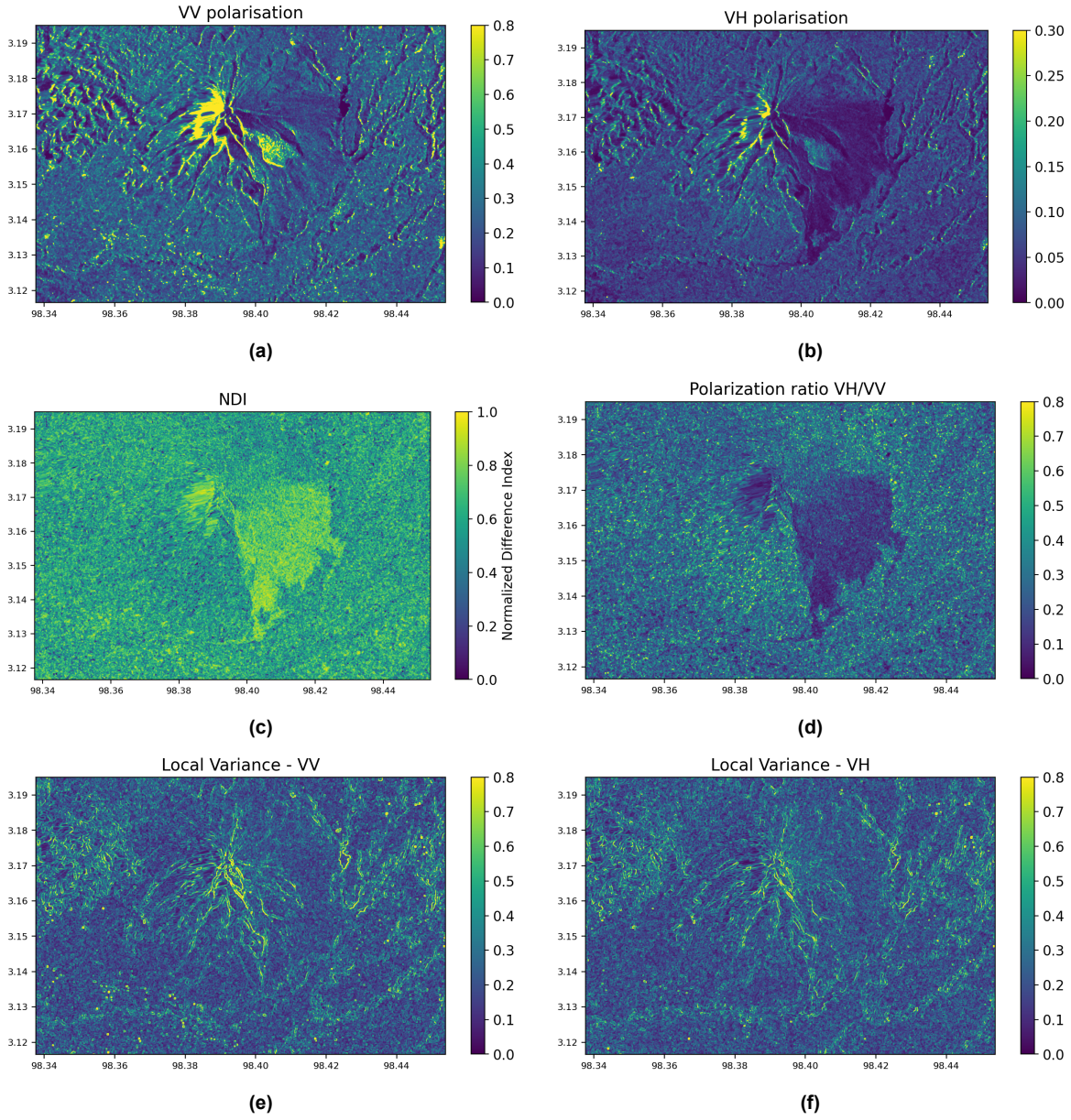

Figure 4.3: Sinabung case study site *basic* features. (a) VV polarisation γ_0; (b) VH polarisation γ_0; (c) Normalised Difference Index (NDI); (d) Polarisation ratio; (e) and (f) local variance calculated based on VV and VH, respectively.

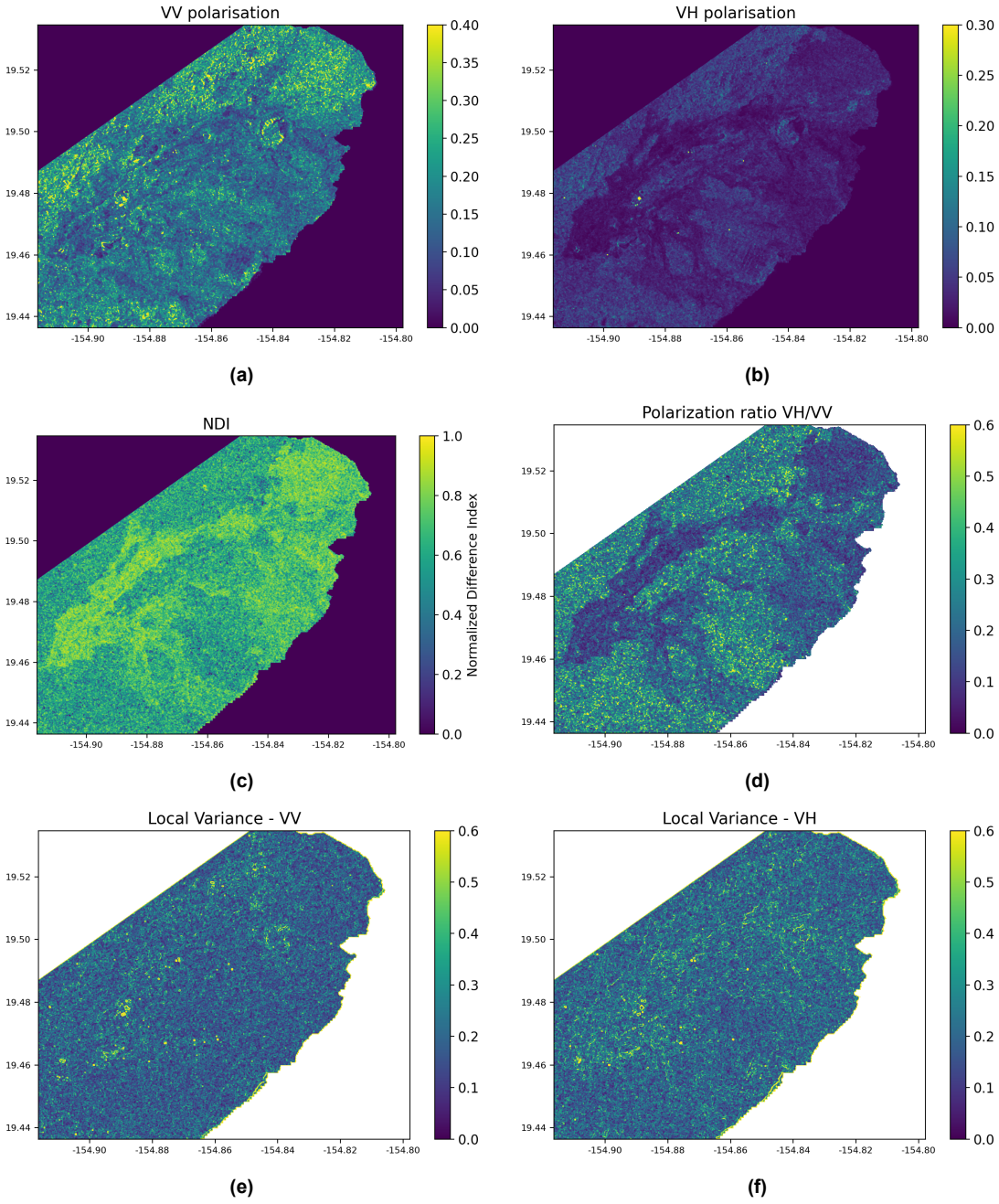

Figure 4.4: Kilauea case study site *basic* features. (a) VV polarisation γ_0; (b) VH polarisation γ_0; (c) Normalised Difference Index (NDI); (d) Polarisation ratio; (e) and (f) local variance calculated based on VV and VH, respectively.

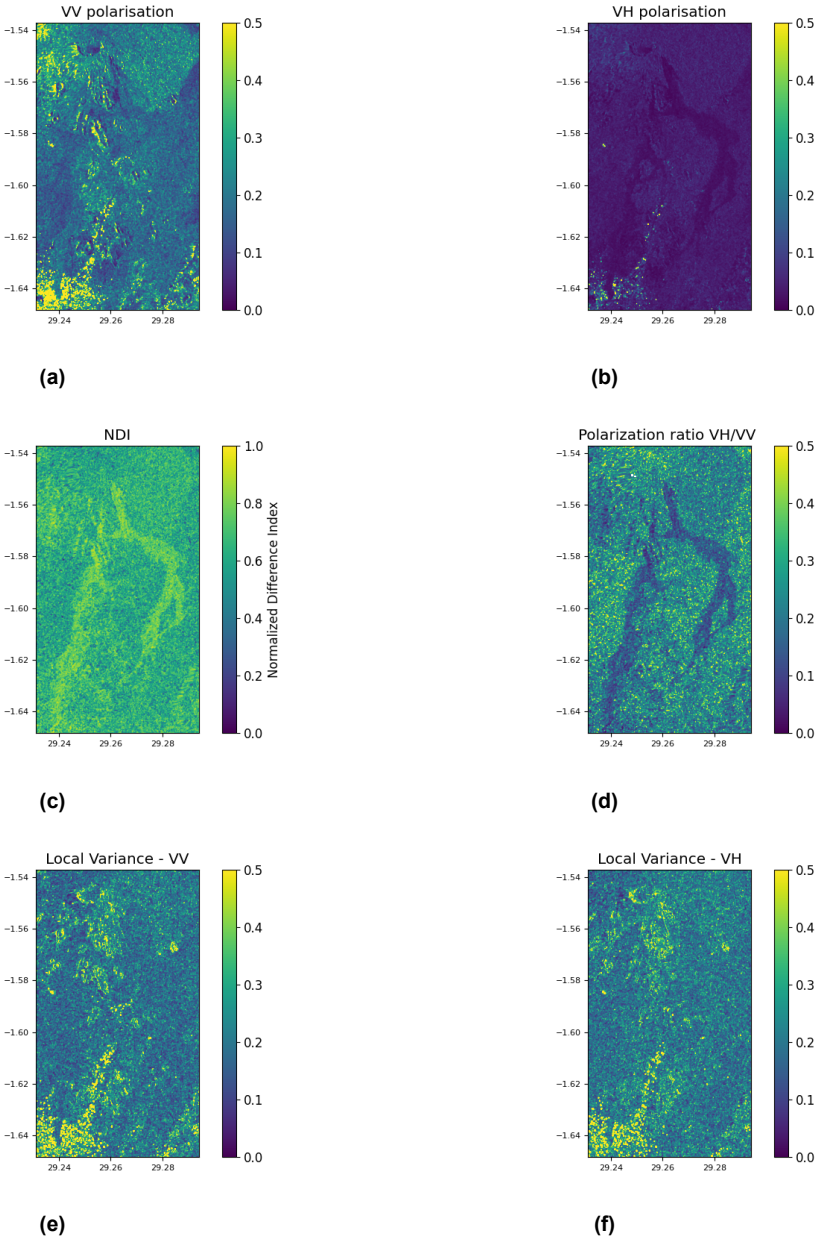

Figure 4.5: Nyiragongo case study site *basic* features. (a) VV polarisation γ_0; (b) VH polarisation γ_0; (c) Normalised Difference Index (NDI); (d) Polarisation ratio; (e) and (f) local variance calculated based on VV and VH, respectively.

4.2. GLCM features

Due to the extensive number of GLCM feature images, only a selection of the most pertinent ones is presented here. The remaining features are available in the Appendix C. This pre-selection was made based on logical criteria to highlight key findings and interesting patterns observed in the data.

Figure 4.6, depicting the Fuego volcano, consists of four texture maps in grayscale for the ASM feature in VH polarization across the four principal angles. The images are almost identical, indicating that ASM is not directional. This similarity is expected considering that ASM measures texture uniformity by summing the squared probabilities of pixel pairs in the GLCM as explained in Appendix B. Since all pixel pairs contribute equally to the value within a window without considering their spatial arrangement, ASM generally does not exhibit directional properties.

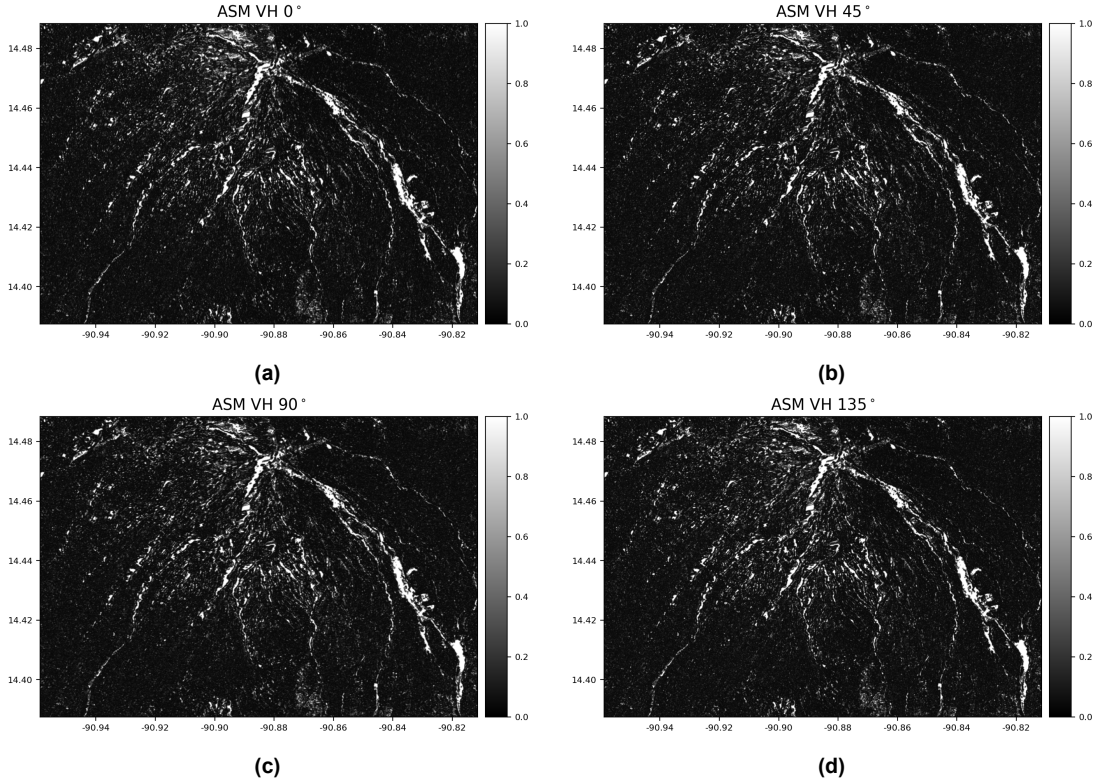

Figure 4.6: GLCM ASM texture maps in VH polarisation and all directions; (a) Horizontal, (b) diagonal, (c) vertical and (d) anti-diagonal. The maps are almost identical.

Overall, the deposits exhibit higher values of ASM, suggesting that the texture of PDC deposits is more uniform compared to the background vegetation. The deposits have a consistent particle distribution, while the background, likely due to leaves, branches, and shadows, entails a more complex and varied structure. Other ASM calculations for the VH polarisation follow a similar pattern and can be found in the Appendix C.

On the other hand, in most cases, ASM calculated based on the VV polarisation does not offer a visible difference between classes. Some examples are presented in Figure 4.7. This outcome is anticipated because the original VV images provide little-to-no distinguishing information. The low contrast contributes to the homogeneous appearance of the area, making the deposits appear ”blending” into their respective backgrounds.

Next, Figure 4.8 illustrates mean GLCM contrast texture maps based on VH polarisation. One can discern that, where visible, the contrast of the deposit is lower compared to the contrast of the surroundings. For Sinabung, the lava flow with the PDC deposit is distinguishable, however, its values are similar to those of the background.

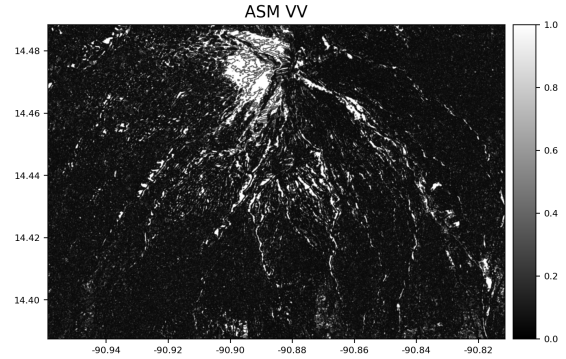

(a) Fuego volcano.

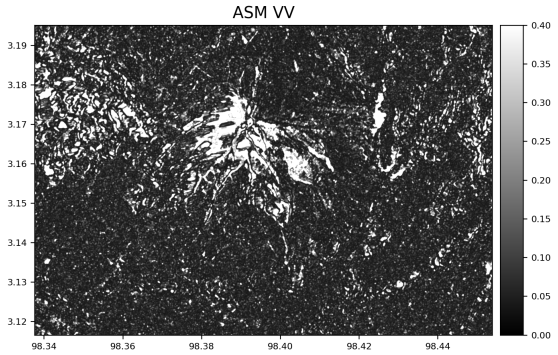

(b) Sinabung volcano.

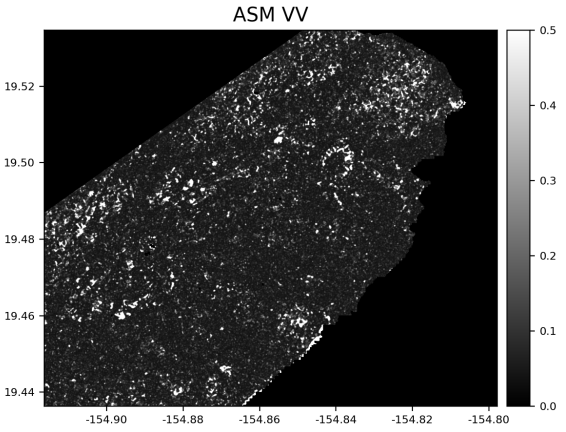

(c) Kilauea volcano.

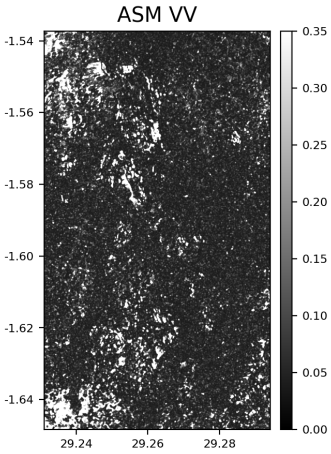

(d) Nyiragongo volcano.

Figure 4.7: Mean ASM VV texture maps for all case studies. Note the scale difference in colormaps. VV polarisation does not appear to ”highlight” the deposits from the background.

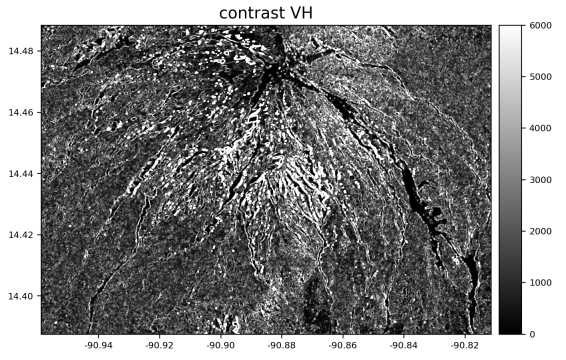

(a) Fuego volcano.

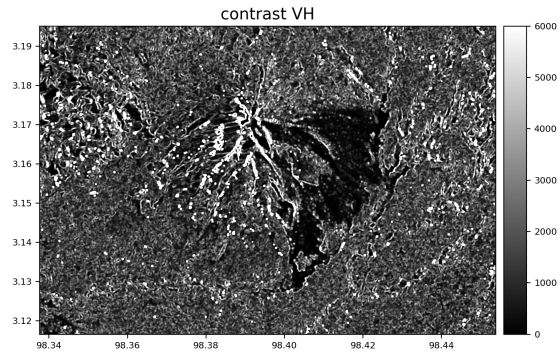

(b) Mt. Sinabung.

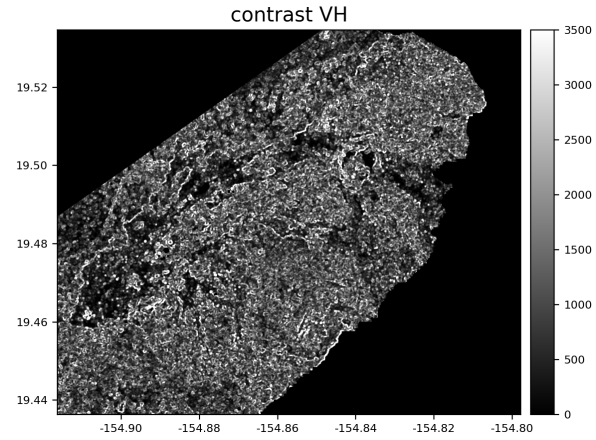

(c) Kilauea.

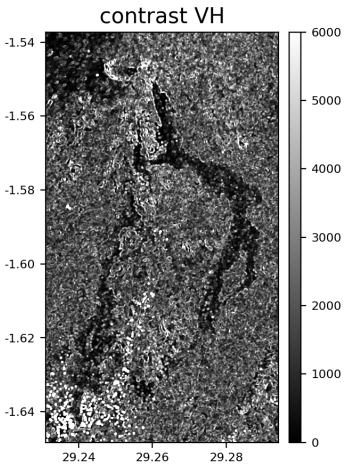

(d) Mt. Nyiragongo.

Figure 4.8: Mean contrast maps in VH polarisation for all case studies.

Additionally, we may focus on a specific case and discuss directionality. Figure 4.9 shows the contrast texture maps for Sinabung in two (2) directions: horizontal and diagonal, where one can observe the difference in brightness levels - an indicator of directional variation in texture. The dark areas representing the PDC deposit remain low in contrast in both cases, indicating uniformity in pixel intensities. The bright areas - background - represent regions with high contrast, where the intensities change with direction. These variations suggest a textural anisotropy in the background, meaning the vegetation around the deposit exhibits different properties in different directions. This directional variation of the background as opposed to the stable low values of contrast irrespective of direction for deposits, can contribute in differentiating the two.

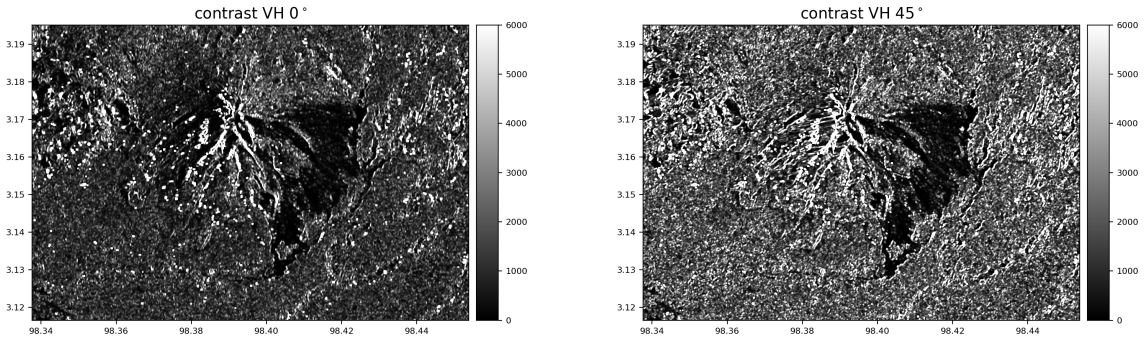

(a) Horizontal direction. **(b)** Diagonal direction.

Figure 4.9: The case of Sinabung - Contrast texture maps in two directions.

Fuego provides an interesting case for dissimilarity due to its evident directionality. Figure 4.10 highlights the differences between the diagonal (45°) and off-diagonal (135°) directions in the texture maps. The diagonal image has pronounced bright lines and features, suggesting higher dissimilarity in this direction. These differences indicate that the texture has directional components, with the diagonal being the dominant direction. However, both directions contribute to the pool of information needed in classification. For instance, only in the 135° image is the thin stream of PDC visible (right red circle).

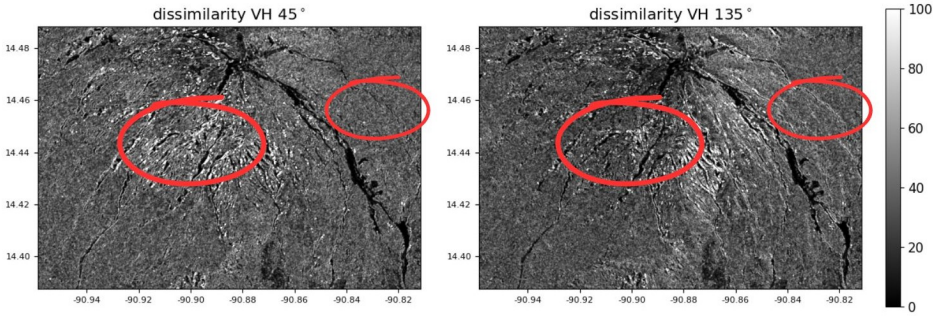

Figure 4.10: The highlighted differences suggest that the texture is anisotropic. The 45° image may highlight certain linear features or edges more prominently, resulting in higher dissimilarity values and stronger texture variations. The 135° direction may not align with these features or edges as strongly, leading to lower dissimilarity values in these areas.

Similarly, when juxtaposing the 0° and 90° dissimilarity texture maps (Figure 4.11), one can notice that the background exhibits directional anisotropy, with some brighter areas highlighted in the vertical direction. The brightness level of the deposit remains relatively stable in all directions.

Ankita et al. [4] follow an alternative method to evaluate directionality using percentage differences. They characterised rocks using GLCM features and suggested that an isotropic scene

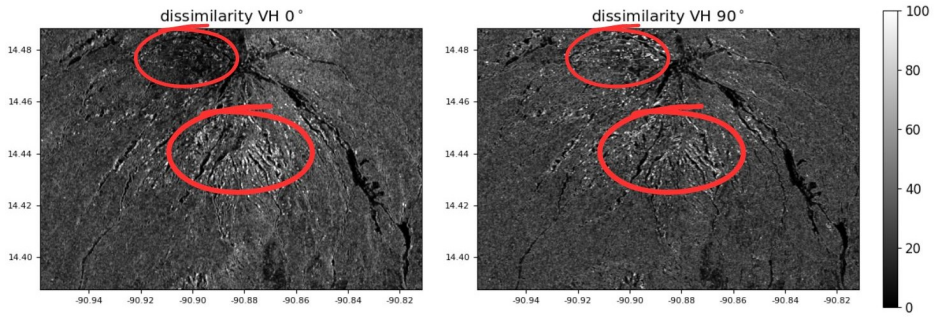

Figure 4.11: Highlighted differences in red for the dissimilarity texture maps in 0° and 90° directions; a sign of directional anisotropy mainly in the background.

would exhibit similar GLCM feature values in perpendicular directions (0° vs 90° and 45° vs 135°). Conversely, an anisotropic scene would show more considerable differences in these features.

Using the Fuego example, the mean dissimilarity VH observed in each direction is:

- Mean Dissimilarity 0°: 26.88
- Mean Dissimilarity 45°: 35.95
- Mean Dissimilarity 90°: 25.50
- Mean Dissimilarity 135°: 33.47

The percentage differences between orthogonal and diagonal directions are:

- Percentage Difference 0° vs 90°: 5.4%
- Percentage Difference 45° vs 135°: 7.4%

These results confirm the conclusions made visually: the diagonal direction is the dominant texture direction for this feature. However, it is worth noting that part of the larger percentage difference observed in the diagonal directions (45° vs 135°) can be attributed to the greater distance between pixels in these directions, which increases the dissimilarity values. To clarify, vertical or horizontal adjacent pixels have a distance of one pixel unit, while the distance between diagonally adjacent pixel pairs is $\sqrt{2}$ pixel units.

Lastly, Figure 4.12 illustrates the mean homogeneity feature in VH polarisation. The figure reveals a clear visual distinction between the deposits and their surroundings in most cases. The deposits appear bright, with values close to one for PDCs, indicating high uniformity and smooth texture. Lava flows also demonstrate high homogeneity, although not as pronounced as the PDCs.

An interesting observation from Figure 4.12c and other Kilauea images in Appendix C is the low contrast between background and deposit. The latter is barely discernible, despite the clear distinctions evident in the quantised images used as input for the GLCM calculations. The quantised image in VH polarisation is demonstrated in Figure 4.13. This discrepancy could be attributed to the choices pertaining the normalisation technique described in Appendix B. It is also plausible that the window size (5 x 5) used in the co-occurrence matrix calculation is the limiting factor.

4.3. Performance

Figure 4.14 portrays the confusion matrices for model 1 and model 2. They perform relatively well, evidenced by the percentages of True Positive (TP) and True Negative (TN) rates. Their accuracy scores are comparable (0.832 and 0.794). The first model has a high False Positive

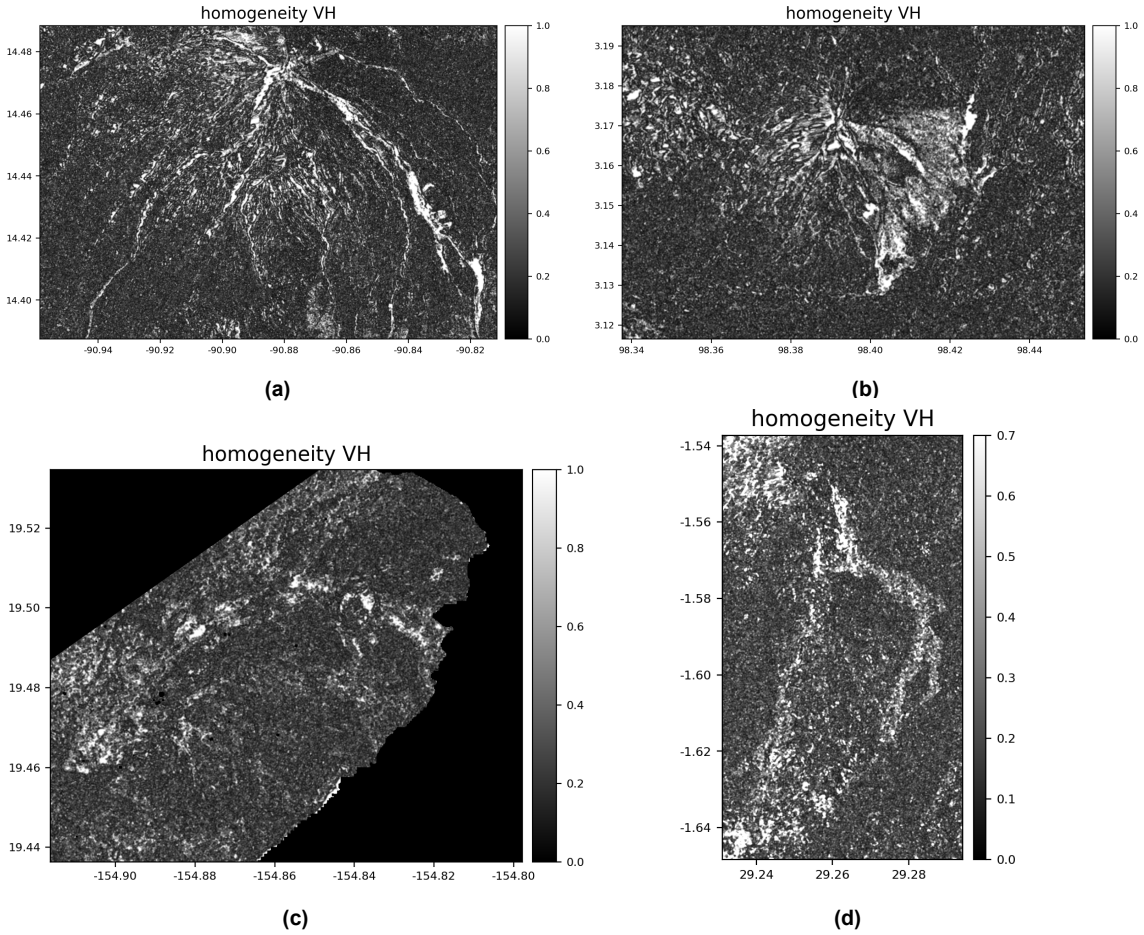

Figure 4.12: Mean homogeneity texture maps in VH polarisation for all case studies.

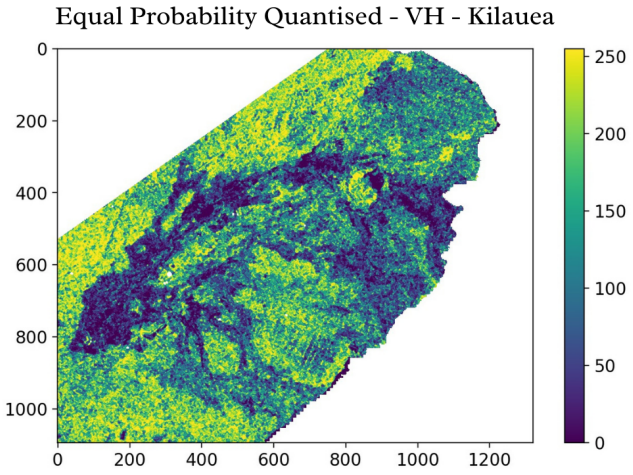

Figure 4.13: Equal Probability Quantised image of γ_0 - VH polarisation - Kilauea. The image exhibits high contrast between deposit and background.

(FP) rate of 26%; approximately one fourth of the *deposit* pixels are mistakenly recognised as *background*. This might not pose a significant problem for our application since ”losing” some deposit pixels is not crucial for our objective. One can fill-in the gaps with techniques such as spatial or density-based clustering, watershed algorithms and canny edge detection.

Model 2, with classes *lava* and *PDC*, demonstrates a high level of accuracy in correctly identifying *PDC* pixels. During parameter tuning for the second model high TP and low FP rates

were intentionally pursued. The high False Negative (FN) rate for *lava* predictions suggests a risk of overlooking lava events, which is essential for high-reliability applications.

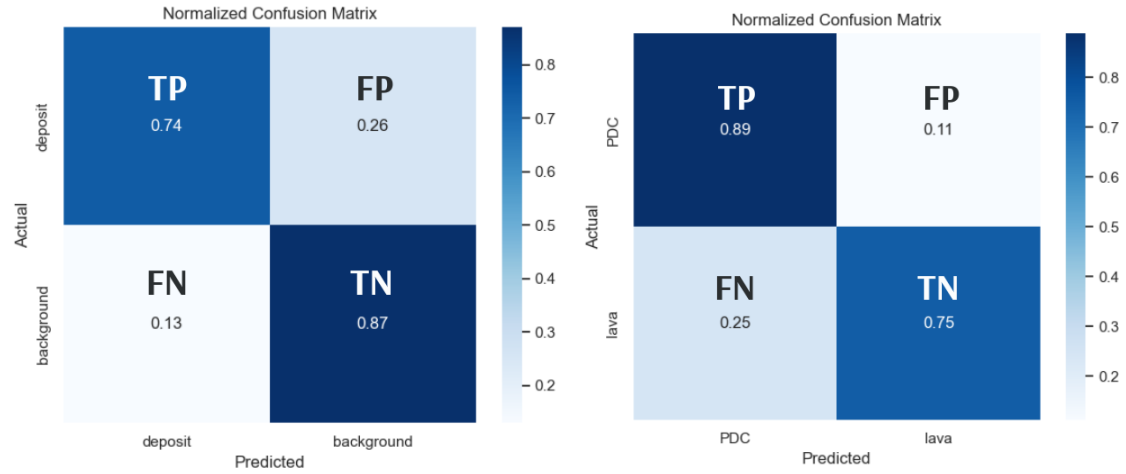

(a) Normalised confusion matrix of model 1 with classes *deposit* and *background*.

(b) Normalised confusion matrix of model 2 with classes *lava* and *PDC*.

Figure 4.14: In model 1 (a) there is a true positive rate of 74% for identifying the *deposit* class. In model 2, (b), 11% of the PDC pixels were mistakenly classified as lava.

Table 4.1 is a summary of the performance metrics for both models. The accuracy on the validation (test) set for the first model is 0.832, suggesting that it correctly predicts the outcome for approximately 83.2% of the cases. However, as mentioned in chapter 3, there might be better metrics for highly imbalanced datasets than accuracy. The F1 scores for the first model suggest balanced precision and recall, especially for the negative (*background*) class, while the scores of the second model are slightly lower. Regarding the RMSE values, in the context of binary classification 0.35 and 0.42 are relatively high. This suggests that, on average, the predicted probabilities deviate from the actual binary outcomes by approximately 0.4. Given that the maximum possible deviation is 1 (e.g., predicting 0 when the actual label is 1 or vice versa), the deviation is substantial.

Table 4.1: Performance Metrics of the Models

Metric	**Model 1**	**Model 2**
Accuracy	0.832	0.794
	F1 Scores	
Positive Class Negative Class	0.73 (deposit) 0.88 (background)	0.72 (PDC) 0.84 (lava)
RMSE	0.35	0.42
AUC-PRC	0.94	0.96
AUC-ROC	0.89	0.91

A key metric for this application is the Area Under the Precision-Recall Curve (AUC-PRC). Both models exhibit high values, which indicates excellent performance, especially when positive class instances are a smaller subset of the total population (class imbalance). The Precision-Recall Curve for model 1 illustrated in Figure 4.15 showcases that the model maintains high precision across varying levels of recall, making it reliable for predicting the positive class even in imbalanced datasets. The Receiver Operating Characteristic (ROC) curve presented in the same figure, also affirms the model's quality, with an AUC of 0.89. It suggests that the model distinguishes well between the classes across different thresholds. The curve stays well above the diagonal line of no-discrimination, confirming that the model significantly improves

over random guessing. The curves for model 2 are presented in Figure 4.16 and they indicate similar behaviour.

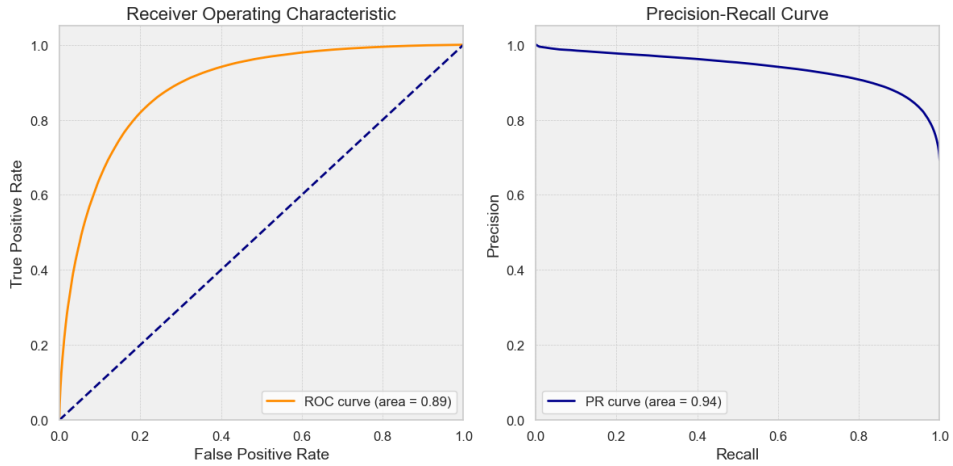

Figure 4.15: Left: Receiver Operating Characteristic (ROC) curve; right: Precision-Recall Curve (PRC) for Model 1.

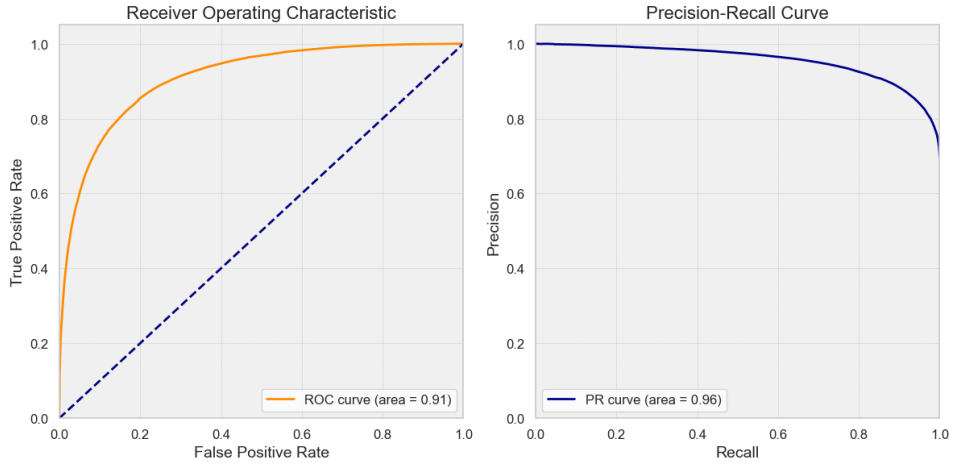

Figure 4.16: Left: Receiver Operating Characteristic (ROC) curve; right: Precision-Recall Curve (PRC) for Model 2.

The tree depth histogram of the first model is presented in Figure 4.17. The distribution appears slightly right-skewed, indicating that there are a few trees with much higher depth than the majority. A deep tree distribution can lead to better performance on the training dataset. At the same time, it risks overfitting, where the model would learn the noise and specific details of the training set and might not generalise well to unseen data. However, this would reflect in a large gap between training and validation performance metrics, which has not been the case.

By definition, random forests introduce a randomness component during training to avoid overfitting, decrease correlation between the trees and enable generalisation. While reducing randomness (e.g., by using all data or all features during training) might enhance the strength of individual trees, increasing tree depth can also achieve a strong tree while maintaining diversity among the ensemble. According to Ren et al. [68], deep trees contribute significantly to the strength of a random forest, so the increased depth of the model is not concerning. Another perspective, as described by Lin and Jeon [55], states that the averaging process in random forests reduces variance but does not significantly lower bias. Random forests are most effective with large trees, where each tree has a small bias. Nevertheless, having negligible bias does not always equate to the best performance and some form of regularisation is

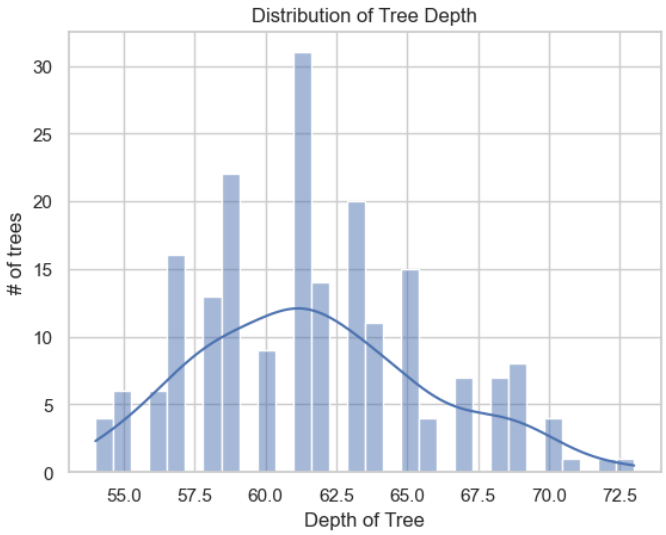

Figure 4.17: Distribution of tree depths for the Random Forest model. High an average tree depth of 62 the complexity of the model is high.

advised.

Feature importances indicate the relative contribution of each feature to the predictive power of the model. For model 1, the results demonstrate that $\gamma_{0,\text{VH\_log}}$ and $\gamma_{0,\text{VH}}$ are the most significant features, with mean decreases in impurity of 0.08 and 0.075, respectively. However, the high standard deviations associated with these importances suggest variability in their contribution across different trees within the forest (Figure 4.18). No single feature stands out as overwhelmingly superior, as indicated by the spread of importances across several features. Interestingly, the top ten features are all the *basic* features. The lack of GLCM-derived features as main contributors in the first model may arise due to the ”blending” effect of applying a moving window in the calculations, leading in a loss of fine details at the edges. GLCM calculations are performed in the entire image (containing both background and deposit) and not in ”cropped-first” images. In addition, the *basic* features often clearly highlight the deposit location.

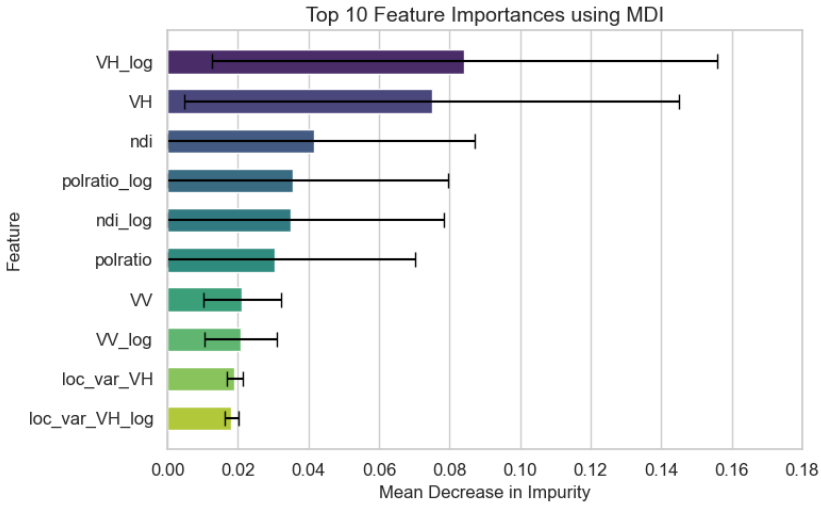

Figure 4.18: The 10 most important features for model 1. The features are nearly equally ”valuable” in predicting the outcome.

On the other hand, model 2 utilises the *GLCM* texture maps to differentiate between deposit types, particularly with ASM and Homogeneity maps. It appears that overall *uniformity* is a

differentiating factor between *lava* and *PDC*, especially in the vertical direction. As seen in Figure 4.19 there is no clear main contributing feature. This could indicate that the selected features provide redundant information, are not strong individually, or that the relationships between them and the target are non-linear and complex. It could also mean that multiple features are equally important in predicting the target variable.

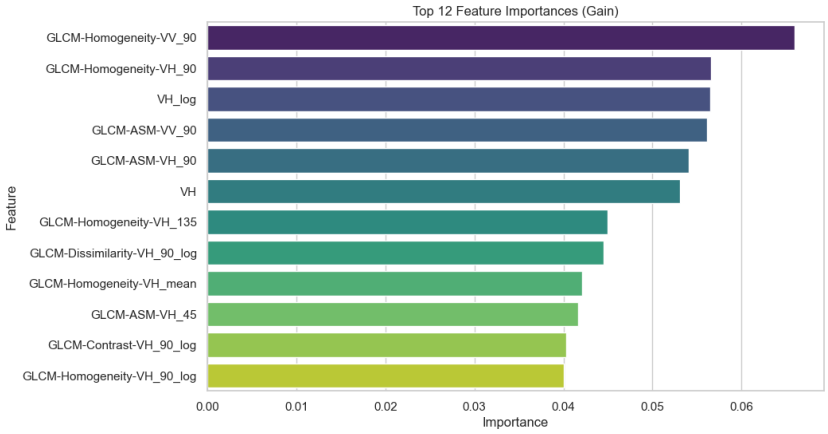

Figure 4.19: The 12 most important features for model 2.

Boxplots of the top four *GLCM* features are presented in Figure 4.20 to gain an insight into their distributions. Figure 4.20a illustrates the boxplot of the Homogeneity feature in VV polarisation and vertical direction. The *PDC* class has overall higher values with the median at approximately 0.35, where the third quartile of *lava* ends. For *PDC*, the interquartile range (IQR) is wider, and the whiskers extend throughout the range of values for that feature. The same feature in the VH polarisation exhibits a similar phenomenon. The ASM boxplots show that 75% of the *lava* pixels have a value lower than 0.1, which is less than the median of the positive class. Both classes contain outliers, with the negative class having relatively more. The *PDC* regions tend to have both higher values and higher variability, which may seem contradictory since ASM measures uniformity. However, this means there is a range of homogeneity levels within the *PDC* class, potentially reflecting natural variations in the texture of PDC deposits. On the other hand, most lava samples have a similar degree of inhomogeneity (low variability), indicating more consistency in the texture despite being overall non-uniform.

Lastly, the permutation feature importances for the second model are presented in Figure 4.21. The analysis was conducted using ten (10) repeats with $\gamma_{0,\mathrm{VH}}$ exhibiting the highest importance, outperforming the other features. Local variance VV has the second highest score, confirming assumptions made earlier regarding the absence of variations in the lava deposit scenes as opposed to visible patterns in the PDC case studies. Overall, the permutation feature scores are well distributed, indicating that the model does not heavily rely on a single feature. The model therefore, captures complex interactions between features, where their combination is more critical than any individual one.

4.4. Visual Assessment

To visually inspect the results and identify the areas with inaccurate predictions, accuracy maps are constructed for all case studies. Figure 4.22 depicts the correctly (blue) and incorrectly (yellow) identified pixels. In the two PDC scenes one can observe that in the borders of the outline there are instances of misclassifications. Sinabung has the highest percentage of correctly identified pixels (87%). There is a big cluster of misclassified pixels within the old lava flow area, which could be related to the difficulty of distinguishing the lava flow from the background as seen in some of the features. The southern most background patch of Fuego shows two streams of yellow pixels, classified as deposit. This is not necessarily an inaccuracy, because in the original image there are some very thin streams of PDC that could

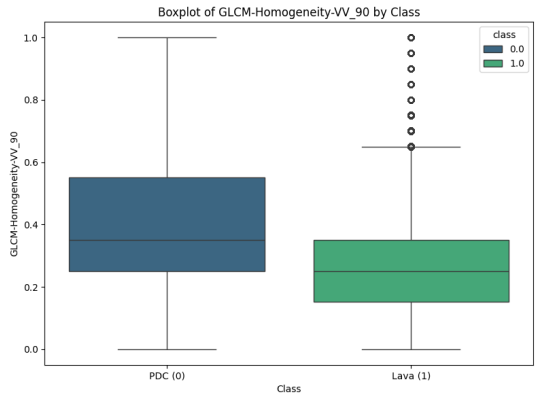

(a) Homogeneity VV 90°.

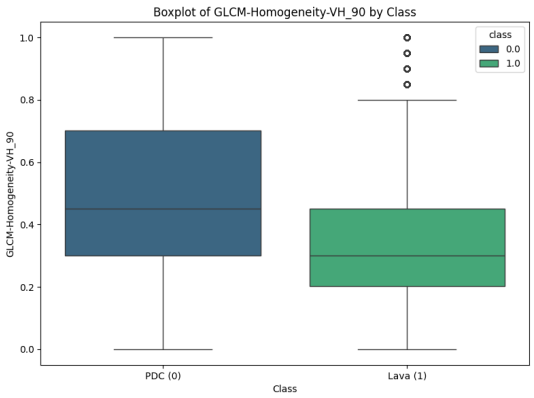

(b) Homogeneity VH 90°.

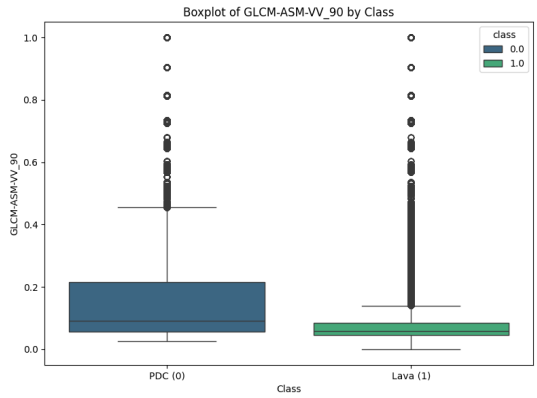

(c) ASM VV 90°.

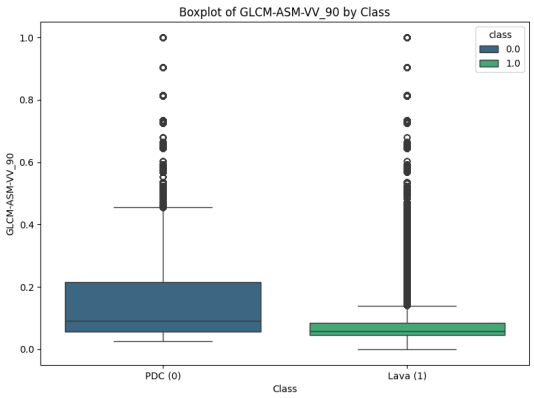

(d) ASM VH 90°.

Figure 4.20: Boxplots for the top four *GLCM* features.

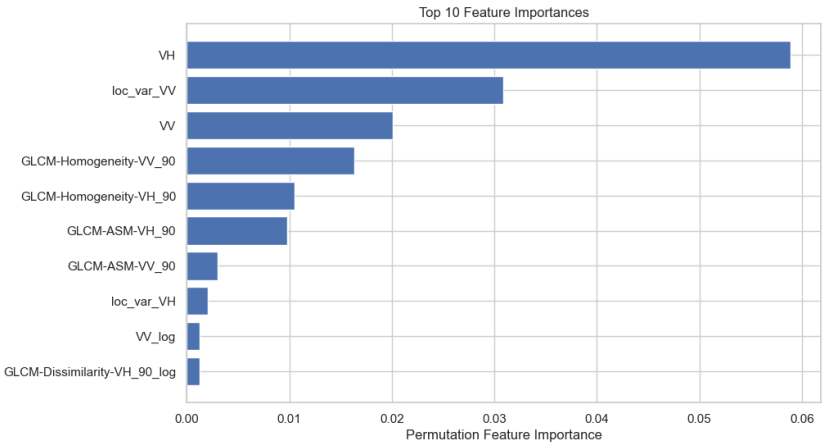

Figure 4.21: Top ten (10) permutation feature importances for model 2.

not be captured by the outline. With respect to the lava flow scenes, the lowest percentage of correct predictions belongs to Kilauea at 78%, with many of them found clustered in the area of the older deposit.

The second model has identified the *PDC* deposits with great accuracy as shown in Figure 4.23a. Sinabung has 85% accurately identified pixels, while Fuego 92%. The two lava deposits have slightly lower correct percentages. Nyiragongo has the lowest percentage at 68%, however it is evident from Figure 4.23b that the main misclassification is happening close to the source of the deposit, possibly due to the steepness of the topography close to the lava lake skewing the results.

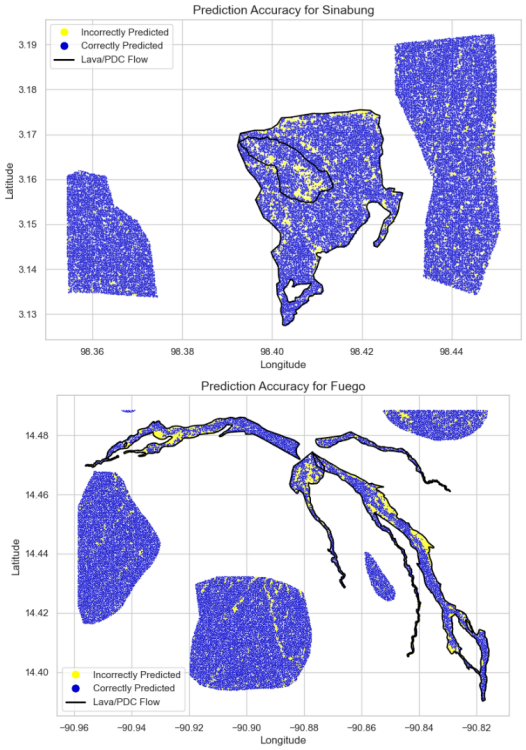

(a) Prediction maps of PDC case studies. Top: Sinabung, Bottom: Fuego.

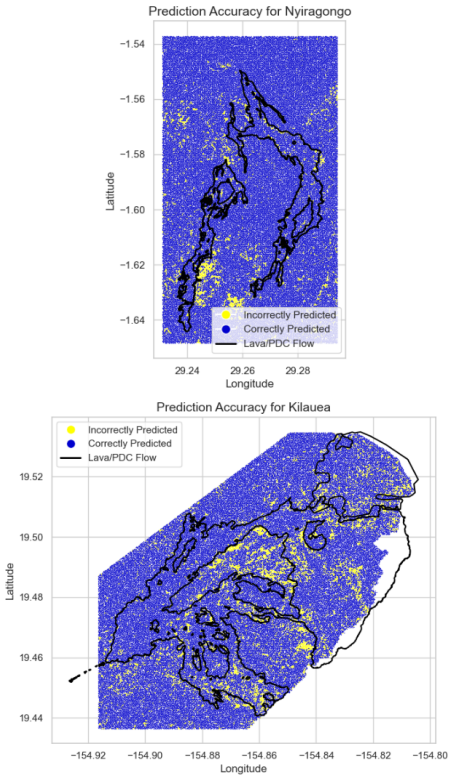

(b) Prediction maps of lava case studies. Top: Nyiragongo, Bottom: Kilauea.

Figure 4.22: Prediction maps of model 1. Blue are correctly identified instances.

4.4.1. The Sinabung case

Three different models were trained to answer the question posed in chapter 3 regarding the lava patch of Sinabung. Including the lava as a third category (*both*) was suboptimal due to the insufficient number of pixels representing this class. Even with oversampling, the results were not promising. Classifying the lava as *lava* yielded slightly better results but reduced the accuracy of predictions for lava deposits in other case studies. Ultimately, labelling the lava patch of Sinabung as *PDC* proved to be the best choice. Figure 4.24 is an image of the thick lava patch at the top of the volcano, visible in the centre. The lava formation appears covered with material from subsequent explosions. This part of the scene remains complex even when used as PDC because the backscatter signal also contains information on scatterers of lower layers due to radar penetration at the surface.

4.5. Unseen data - Case study: Soufrière Hills, Montserrat

The Soufrière Hills stratovolcano has been extensively studied and mapped, particularly focusing on the deposits associated with its activity between 1995 and 2010. The Montserrat Volcano Observatory provided the dataset for this case, which comprises of 29 maps sourced from scientific literature. However, the corresponding researcher indicated that the individual geometries primarily emphasize on deposition areas, meaning the impacted area from dilute flows could be more extensive (Jose M. Marrero, personal communication). Additionally, some maps exhibit significant horizontal deviations in geographic precision. Due to the lower precision of these geometries and the fact that the deposits predate the first Sentinel data, this location was not suitable for training. Nonetheless, the area remains valuable for validation purposes, given the presence of large PDC deposits visible in the optical image shown in Figure 4.25a.

Since the last eruptions, vegetation has overtaken several parts of the island in-between the

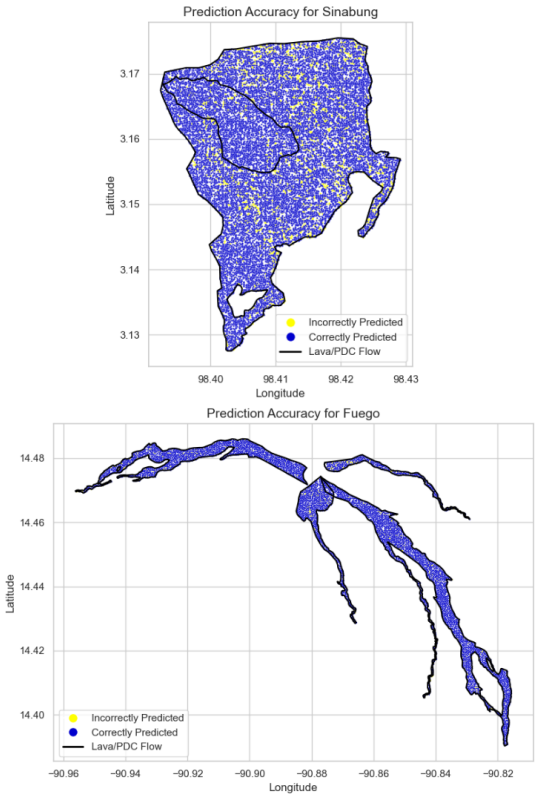

(a) Prediction maps of PDC case studies. Top: Sinabung, Bottom: Fuego.

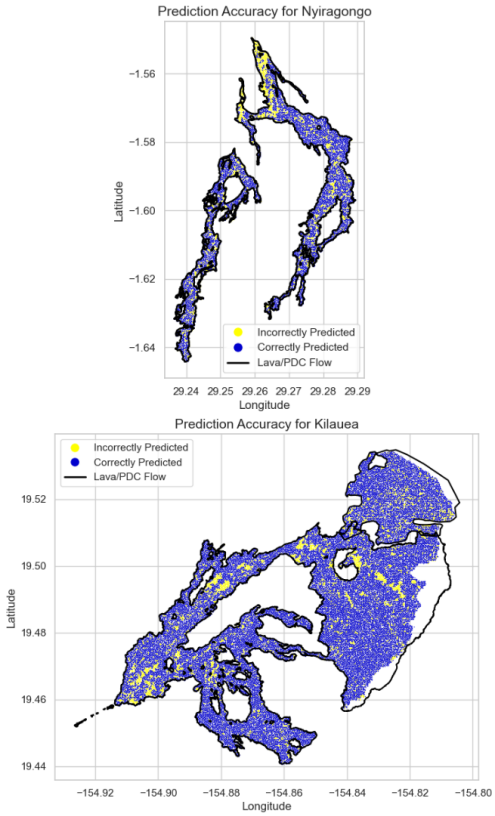

(b) Prediction maps of lava case studies. Top: Nyiragongo, Bottom: Kilauea.

Figure 4.23: Prediction maps of model 2. Blue are correctly identified instances.

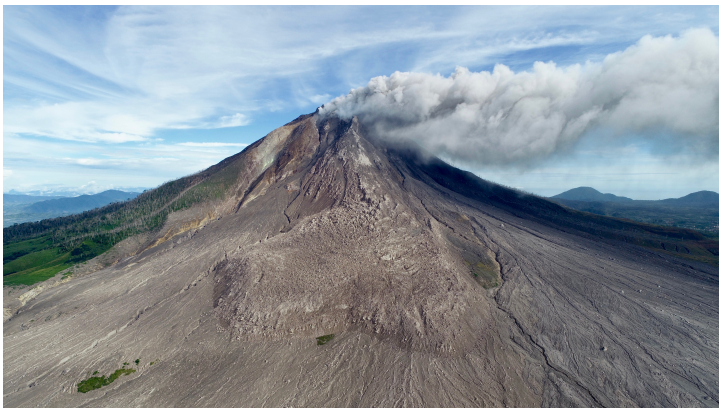

Figure 4.24: Closeup of Sinabung - the 100 m. thick lava is visible at the centre of the image.

flows and this is prominent in Figure 4.25b. The outline is superimposed on the optical image and while it encloses the general area of the PDCs, it is only shown as reference for understanding the results of the classification.

Results from step 1 of the classification workflow indicate a good accuracy as seen in Figure 4.26a. Despite of the prominent deposit, the background areas remain noisy with several pixels classified as *deposit*. Smaller flows are not captured effectively and they are ”lost” in the noise. Before applying step 2, the pixels classified as *background* are discarded. Interestingly, the misclassified background pixels are mainly classified as *lava*, while the main PDC deposit is clearly visible. The PDC areas are noisy, however, the amount of PDC classified pixels within the rough outline is higher than the amount of lava pixels.

(a) True color image from Sentinel hub [77].

(b) True color image [77] overlayed with a rough outline of the deposits.

Figure 4.25: Soufrière Hills volcano in Montserrat.

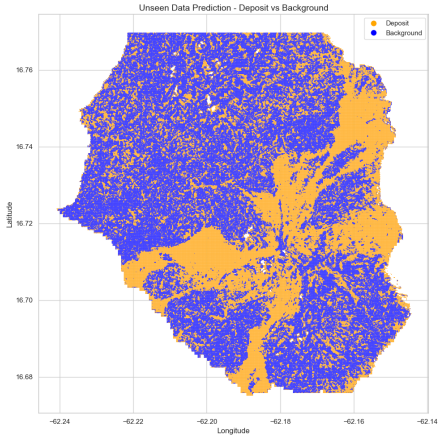

(a) Step 1 of the classification process. Model 1 is used to distinguish between deposit and background pixels.

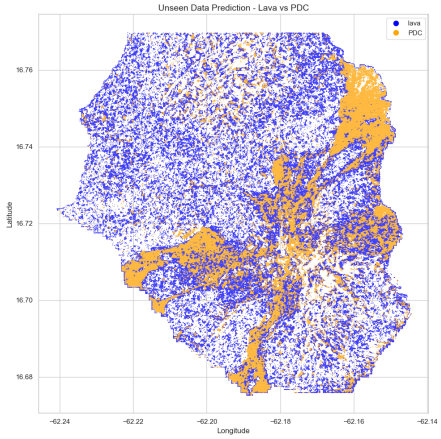

(b) Step 2 of the classification process. Model 2 is used to classify the deposit.

Figure 4.26: Prediction maps of Soufrière Hills, Montserrat.

4.6. Unseen data - Case study: Kīlauea volcano, Pāhoa, Hawaii

In the same region as the Kilauea case study, USGS has mapped the lava flow associated with the ”June 27th” lava flow (Pu’u ’Ō’ō eruptive episode 61e) that was active at the Kīlauea volcano from June 27, 2014 to June 8, 2016. The geological lines were mapped on the ground or during helicopter reconnaissance flights using a GPS [94]. Figure 4.27 shows the mapped lava flows on the polarisation ratio map of the area. Only part of the flows within the area are attributed to the aforementioned event, however, there is another large lava deposit extending to the coast. Figure 4.28 represents the prediction maps for step 1 and step 2 of the classification process. The *deposit* class has been well separated from the background pixels with minimal noise. The second step contains significant noise, however within the mapped lava flow area the amount of *lava* pixels is much higher than the *PDC* predictions.

In both ”unseen” data case studies, the second model showed a considerable amount of false positives (positive being PDC for Soufrière Hills and lava for Pāhoa). Despite this discrepancy, the number of true positives is double that of false positives, demonstrating sufficient model performance for this application.

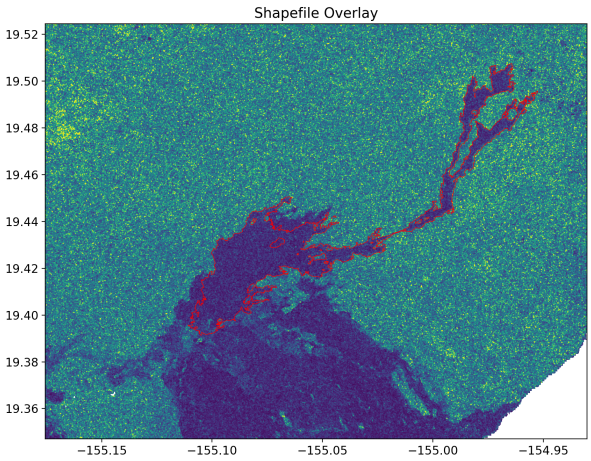

Figure 4.27: Pāhoa region, mapped lava flows in red outline overlayed on polarisation ratio.

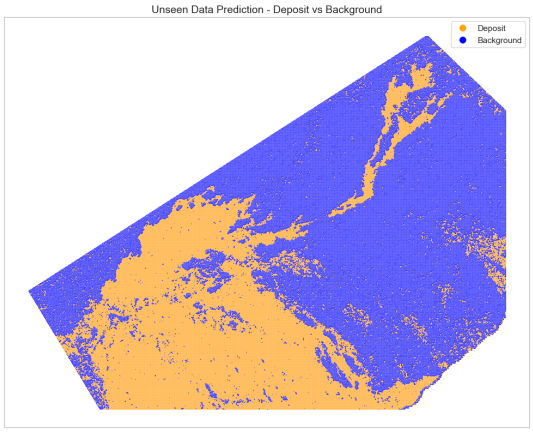

(a) Prediction map of Pāhoa case study for step 1. The deposit has been predicted with with remarkable accuracy.

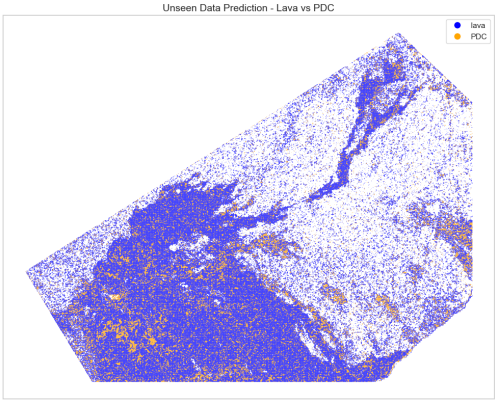

(b) Prediction map of Pāhoa case study for step 2. The majority of the pixels are classified as *lava*.

Figure 4.28: Prediction maps of model 2. Blue are correctly identified instances.

5
Discussion

This thesis presents a unique, simplistic approach to classifying volcanic deposits using machine learning techniques applied to SAR data. This chapter discusses several key findings, with observations relating to various stages of data preprocessing, feature selection, model selection, training, and evaluation.

Classifying deposit types into two broad categories, PDCs and lava flows, is a challenging task. Chapter 2 demonstrates that subtypes of PDCs might exhibit similar textural characteristics to lava flows, whose subtypes also have very different patterns. Despite the complexity, the results seem promising, with the texture features helping greatly in the final classification step, evident by Figure 4.19 indicating their importance.

The framework developed and presented here successfully addresses the main research question posed in chapter 1 by identifying and distinguishing PDCs from lava flows with sufficient accuracy using SAR data. The study's objective is to determine whether a volcanic deposit is present in the scene and, if so, to confidently classify it as either a PDC or a lava flow. The focus is not on achieving perfect per-pixel classification but making a reliable binary distinction between the two deposit types.

Overall, the Sentinel-1 datasets' resolution is adequate to capture the morphological characteristics of the deposits. While the presence of noise in the output classification maps is concerning, it does not prohibit the application. In both cases of "unseen data," the model effectively indicated the presence of deposits in the scenes. Moreover, despite the noise, the correct deposit type was identified in double the number of pixels, instilling confidence in the methods' reliability.

5.1. Limitations, Uncertainties and Future Research

The difficulty in achieving a low RMSE without overfitting and increasing the classification output's signal-to-noise ratio (SNR) could indicate that the derived features cannot effectively capture the relationships between the classes. Several reasons, such as feature quality and relevance, may contribute to this effect. However, for this work, it is presumed that there may be too many irrelevant or redundant features (e.g., NDI and polarisation ratio or contrast and dissimilarity). This can dilute the importance of the ones that matter most and lead to overfitting. Feature selection techniques such as Principal Component Analysis (PCA) can help limit the features or reduce dimensionality to improve model performance.

Another study limitation that could be addressed in future work is that the background pixels used for training mainly represent vegetated areas. Considering that the framework is intended for comparative planetology and applied on planetary landforms where vegetation is absent, the first model, which distinguishes between background and deposits, would benefit from retraining with data from bare soil environments instead of vegetated regions. This adjustment leverages the modular nature of the two-step model approach, allowing for targeted retraining of just the first model without altering the overall framework.

In addition, it has been established that microwaves penetrate Earth's top layers and provide information on scatterers below the surface [22]. It is commonly cited that pre-eruption land cover affects the backscatter signal, complicating classification and interpretation by introducing another unknown variable. The returning signal from the C-band SAR data is a composite signal from the top few centimeters of the surface depending on the surface material and conditions. For the application in this study, pre-eruption land cover is not expected to influence the results considering that the deposited formations are typically thicker than Sentinel-1's penetration depth. On the other hand, variability in moisture content can reduce interpretability in the SAR signal. If surface roughness remains unchanged, radar backscatter increases with increasing moisture content. The relationship between the two is generally non-linear and affects both *basic* and *GLCM*-derived features. In addition, with heavy rainfall, the main contributors to the signal are near-surface scatterers. Despite the added complexity, *GLCM* texture map features such as homogeneity and ASM are designed to be resilient to uniform changes in pixel values - both of which were ranked high in feature importance. Lastly, rainfall as we experience it on Earth is not present on most other planetary bodies, including Venus, so it is not expected to be a limiting factor for those cases.

Despeckling filters, spatial resolution, and GLCM-related parameter choices may also limit performance, and they will be discussed in the following paragraphs. Certainly, the access to only four case studies as input adds to the challenge. Initially, more locations were considered, such as the Stromboli volcano in Italy, the Merapi volcano in Indonesia, Colima in Mexico, Alamagan in the Mariana Islands and Mt. Helens in Washington. However, they were deemed unsuitable for various reasons, including scattered deposits, encroaching vegetation, and the age of the eruptions.

With sufficient time and computational resources, one could extract additional texture maps using various sliding window sizes rather than relying solely on initial assumptions. Selecting a single window size suitable for all deposits is challenging. For example, PDC deposits can be both homogeneous with fine details (lahars) and non-uniform due to the mix of ash, pumice and coarser rock fragments. Small window sizes (e.g., 3x3, 5x5) capture fine-scale details and high-frequency variations, making them sensitive to localised texture changes. Conversely, larger window sizes are sensitive to large-scale variations and are likely better suited for more uniform surfaces, such as that of pahoehoe lava.

Spatial resolution subtleties Another deciding factor in the window size is the spatial resolution. The effective spatial resolution of the GRD dataset in IWH mode is approximately 20 x 20 meters, but it is oversampled and provided with a finer pixel spacing of 10 x 10 meters. That does not signify that adjacent pixels contain identical values, as oversampling uses interpolation techniques that introduce variations and provide a smooth transition. Therefore, the smallest window in GLCM can represent 30 by 30 meters on the ground. However, that might not be optimal, considering each pixel's actual detail is limited to 20 meters. Adding to the complexity, the GLCM "searches" for spatial patterns at a specified pixel distance, which in this case is one. A distance of two may capture more relevant texture information and better reflect the true spatial resolution. Optimally, multiple distances and window sizes should be used to capture the patterns at varying scales, providing a more comprehensive representation of the assorted textures in volcanic deposits.

A convolutional neural network (CNN) could theoretically "learn" the optimal filters and window sizes for this task, adapting to various texture scales. However, this approach requires large datasets to train the network effectively. In the absence of such datasets, it is still recommended to manually create the additional texture feature maps to ensure comprehensive texture analysis.

Noise and mitigation One way to address the noisiness in the output classification maps is to apply image processing techniques. A centroid or density-based clustering algorithm could help accurately delineate the deposit and produce a visually appealing classification map. Moreover, object-based classification and edge-detection algorithms could be fitted within the workflow to reduce noise output and improve data fidelity, especially after applying the first model.

The role of filters in comparability The process known as *despeckling* is an integral part of preprocessing SAR data. Various filters are available, and the one used here is the *Refined Lee* filter, which is an improvement to the original Lee filter. The latter reduces speckle by performing a smoothing operation within a sliding window based on local statistics, and the former incorporates edge detection and directional filtering for better edge preservation [51]. *Refined Lee* is an adaptive filter based on local image patterns, which can enhance quality; however, in the context of image classification, it might reduce comparability and consistency between the datasets. This is an effect of its adaptive nature since it applies different degrees of smoothing and edge preservation across the image, reducing uniformity in preprocessing. Considering that the applied models perform pixel-by-pixel classification, the need for edge and fine detail preservation is not imperative. Although the selection of filters is not critical to the classification process, a more effective approach, in hindsight, would consist of a more straightforward filter such as Lee or Gamma Map Filter.

5.2. Theoretical implications and contributions

The use of traditional (*basic*) features complemented by *GLCM*-derived texture features in deposit classification has proven useful for complex classification tasks. This study emphasises the potential of incorporating multi-scale texture analysis to capture the diverse textural properties of volcanic deposits. By utilising a sliding window approach, the research highlights the necessity of adapting window sizes to better capture fine details in rough textures, such as those found in ’a’ā lava, and broader patterns in smoother textures, such as pāhoehoe lava.

Ultimately, this study’s findings support the hypothesis that volcanic deposits on planetary bodies can be classified using only one source of information, namely SAR data. This validation has implications for planetary geology, particularly as we look toward future missions to Venus, such as the proposed NASA VERITAS and ESA EnVision missions, which will carry advanced SAR instruments like VenSAR. These missions will provide high-resolution SAR data that could be instrumental in detecting and classifying various volcanic landforms on Venus [31]. For example, large-scale features such as lava plains and large lava flow fields should be relatively easy to detect due to their extensive coverage and distinct radar signatures. Smaller, thinner and less extensive lava flows and PDCs should be moderately challenging to detect and distinguish due to their intricate details and subtle differences in surface roughness. The most difficult features to detect should be thin lava flows, especially those emplaced in narrow channels or depressions, as they may blend with their surroundings. Ash-fall deposits with fine-grained pyroclastic materials may also be particularly challenging due to their smooth surface spanning a substantial area, potentially more extensive than a single SAR image.

Moreover, this study prompts further investigation into how spatial resolution impacts classification accuracy. Future research should explore whether lower resolutions suffice for planetary geology or if the resolution provided by Sentinel-1 represents the minimum threshold necessary. Addressing these questions could refine the application of SAR data in planetary geology and optimise resource utilisation and payload requirements in future mission planning.

This study contributes to the field’s theoretical understanding and practical capabilities by advancing the methodology for volcanic deposit classification and highlighting the practical applications of SAR data.

6

Conclusions

This study developed and evaluated a framework for classifying volcanic deposits using information exclusively from SAR data. The methodology encompasses several critical steps: pre-processing workflow suitable for regions with significant topographic variability, extraction of *basic* features from VV and VH polarisations, appropriate image normalisation, the use of *GLCM* to calculate texture features that reveal underlying patterns within the deposits and a two-step approach in classification.

The framework utilises Sentinel-1 GRD data of four case studies, beginning with a series of preprocessing steps: orbit correction, thermal and border noise removal, calibration, radiometric terrain flattening, despeckling, and Range-doppler terrain correction. This sequence results in reflectivity estimates in VV and VH polarisations. Subsequently, both polarization images are used to calculate first and second order texture measures, specifically: NDI, polarization ratio, local variance, and GLCM-derived texture measures. These features serve as inputs to a random forest classifier, which distinguishes deposit pixels from background pixels. The deposit pixels are then further classified into lava flows and PDCs using extreme gradient boosting. The final output is a classification map indicating which areas contain background, lava or PDCs.

The first model exhibits high complexity due to the increased tree depth, despite a clear visual distinction between the deposit and background in several features. However, a deeper tree distribution is not necessarily inadequate. The False Positive rate is relatively high at 26%, but this is acceptable for the application. Given the high values of AUC-PRC and AUC-ROC metrics, the model does not show signs of overfitting. Nevertheless, the RMSE of 0.35 is concerning, considering the maximum deviation in binary classification is 1. The second model faces a similar issue with an RMSE of 0.42 but predicts PDC deposits with a high True Positive rate of 89%.

Overall, the results obtained through ”unseen data” from Montserrat, Soufriere Hills, and Pahoa, Hawaii are noisy but adequately distinguish deposits from the background. The second model is also successful as it correctly classifies the majority of deposit pixels as their respective type. While noise was expected, the crucial aspect is that the method works. The approach of using texture features derived from SAR data to confidently identify deposits is suitable for this application and could be further improved.

Feature Selection and improvement A critical enhancement would involve a more systematic selection of features to ensure a streamlined and non-redundant dataset. Notably, the Normalized Difference Index (NDI) and polarisation ratio features convey comparable information. They both capture the relative differences in polarisation backscatter. However, NDI normalizes these differences, so inclusion over the polarisation ratio is recommended. In addition, images constructed based on VV polarisation often lack the contrast necessary to distinguish between background and deposit. Discarding those features from the first model could enhance its predictability.

Furthermore, the texture measures contrast and dissimilarity are constructed similarly, with only minor differences in the weights applied in their final calculations. Contrast is more sensitive to pronounced differences in intensity compared to dissimilarity. Similarly, Angular Second Moment (ASM) and homogeneity are closely related. Therefore, using only ASM and contrast may be sufficient to represent the necessary texture information. Exploring additional GLCM texture features, such as entropy or correlation is also advisable.

This study confirms that texture features can add value in differentiating between lava and PDCs. Analysing the directionality of deposits using four principal angles in GLCM calculations revealed that the vertical direction is particularly useful. Varying the window sizes and distances in GLCM calculations may enhance performance and uncover additional inter-class relationships. Different texture measures can substitute or complement the GLCM features. Methods such as Local Binary Patterns (LBP) or Wavelet Scattering Transforms can capture different aspects of texture, potentially enriching the dataset with diverse textural information.

Broader Impact This study contributes to the broader field of remote sensing in volcanology by demonstrating the efficacy of SAR data for deposit classification. This contribution underscores the importance of texture analysis in advancing our understanding of geological processes and improving hazard assessment in volcanically active regions. High-resolution imagery might not always be available, especially in planetary missions. The methodologies developed here also offer potential applications in planetary exploration, providing a foundation for future research in planetary geology. Further research is needed to understand the role of spatial resolution in this application. If it is critical for pattern detection, missions could perform initial reconnaissance to locate deposits and subsequently conduct high-resolution surveys at those locations.

Future work could explore the capability of these techniques to discriminate between subtypes of lava and PDCs, potentially with higher-resolution imagery. Incorporating part of this framework directly onboard the satellite, such as on an FPGA, could significantly reduce processing time and enable near real-time output. This real-time capability would facilitate timely monitoring and rapid response during volcanic events, enhancing the effectiveness of hazard assessment and mitigation strategies.

References

[1] Lomoschitz A. et al. “Characterisation of a Pleistocene debris-avalanche deposit in the Tenteniguada Basin, Gran Canaria Island, Spain”. In: *Landslides* 5 (May 2008), pp. 227–234. DOI: 10.1007/s10346-008-0115-6.

[2] European Space Agency. *Sentinel-1 Mission Overview*. https://sentiwiki.copernicus.eu/web/sentinel-1. Accessed: 2024-05-26. 2024. URL: https://sentiwiki.copernicus.eu/web/sentinel-1.

[3] Alaska Satellite Facility. *What is SAR?* Accessed: 2024-06-06. 2024. URL: https://asf.alaska.edu/information/sar-information/what-is-sar/#sar_concepts.

[4] Singh Ankita et al. “Rock Characterization Using Gray-Level Co-Occurrence Matrix: An Objective Perspective of Digital Rock Statistics”. In: *Water Resources Research* 55.3 (2019), pp. 1912–1927. DOI: https://doi.org/10.1029/2018WR023342. eprint: https://agupubs.onlinelibrary.wiley.com/doi/pdf/10.1029/2018WR023342. URL: https://agupubs.onlinelibrary.wiley.com/doi/abs/10.1029/2018WR023342.

[5] Korosov Anton et al. “Thermal Denoising of Cross-Polarized Sentinel-1 Data in Interferometric and Extra Wide Swath Modes”. In: *IEEE Transactions on Geoscience and Remote Sensing* 60 (2022), pp. 1–11. DOI: 10.1109/TGRS.2021.3131036.

[6] Mariana Belgiu and Lucian Drăguț. “Random forest in remote sensing: A review of applications and future directions”. In: *ISPRS Journal of Photogrammetry and Remote Sensing* 114 (2016), pp. 24–31. ISSN: 0924-2716. DOI: https://doi.org/10.1016/j.isprsjprs.2016.01.011. URL: https://www.sciencedirect.com/science/article/pii/S0924271616000265.

[7] Carr Brett et al. “The Stability and Collapse of Lava Domes: Insight From Photogrammetry and Slope Stability Models Applied to Sinabung Volcano (Indonesia)”. In: *Frontiers in Earth Science* 10 (May 2022). DOI: 10.3389/feart.2022.813813.

[8] Olivier Caelen. “A Bayesian interpretation of the confusion matrix”. In: *Annals of Mathematics and Artificial Intelligence* 81.3-4 (2017), pp. 429–450. ISSN: 1012-2443. DOI: 10.1007/s10472-017-9564-8. URL: https://doi.org/10.1007/s10472-017-9564-8.

[9] Brett B. Carr et al. “Mapping and classification of volcanic deposits using multi-sensor unoccupied aerial systems”. In: *Remote Sensing of Environment* 264 (2021), p. 112581. ISSN: 0034-4257. DOI: https://doi.org/10.1016/j.rse.2021.112581. URL: https://www.sciencedirect.com/science/article/pii/S0034425721003011.

[10] Sylvain J. Charbonnier et al. “Unravelling the dynamics and hazards of the June 3rd, 2018, pyroclastic density currents at Fuego volcano (Guatemala)”. In: *Journal of Volcanology and Geothermal Research* 436 (2023), p. 107791. ISSN: 0377-0273. DOI: https://doi.org/10.1016/j.jvolgeores.2023.107791. URL: https://www.sciencedirect.com/science/article/pii/S0377027323000483.

[11] Stats Exchange Community. *Why by decreasing the depth of the random forest, the overall accuracy decreases*. Accessed: 2024-06-08. 2018. URL: https://stats.stackexchange.com/questions/328795/why-by-decreasing-the-depth-of-the-random-forest-the-overall-accuracy-decreases.

[12] Kent C. Condie. “Chapter 3, 4 and 10”. In: *Earth as an Evolving Planetary System (Third Edition)*. Ed. by Kent C. Condie. Third Edition. Academic Press, 2016, pp. 43–88, 89–133, 317–367. ISBN: 978-0-12-803689-1. DOI: https://doi.org/10.1016/B978-0-12-803689-1.00010-9. URL: https://www.sciencedirect.com/science/article/pii/B9780128036891000109.

[13] Copernicus. *OBSERVER: Copernicus Sentinel satellites bring new insight to volcano monitoring*. Accessed: 2024-07-07. 2022. URL: https://www.copernicus.eu/en/news/news/observer-copernicus-sentinel-satellites-bring-new-insight-volcano-monitoring.

[14] Copernicus Emergency Management Service. *Copernicus Emergency Management Service Assesses Lava Hazard at Nyiragongo Volcano Three Years Later*. https://emergency.copernicus.eu/mapping/ems/copernicus-emergency-management-service-assesses-lava-hazard-nyiragongo-volcano-three-years. Accessed: 2024-05-26. 2021.

[15] National Research Council. *Assessment of Planetary Protection Requirements for Venus Missions: Letter Report*. Washington, DC: The National Academies Press, 2006. DOI: 10.17226/11584. URL: https://nap.nationalacademies.org/catalog/11584/assessment-of-planetary-protection-requirements-for-venus-missions-letter-report.

[16] scikit-learn developers. *RandomForestClassifier*. 2007-2024. URL: https://scikit-learn.org/stable/modules/generated/sklearn.ensemble.RandomForestClassifier.html.

[17] Scikit-learn developers. *Feature importances with a forest of trees*. Accessed: 2024-06-09. 2020. URL: https://scikit-learn.org/stable/auto_examples/ensemble/plot_forest_importances.html.

[18] Scikit-learn developers. *Permutation Feature Importance*. Accessed: 2024-06-09. 2020. URL: https://scikit-learn.org/stable/modules/permutation_importance.html#permutation-importance.

[19] Scikit-learn developers. *sklearn.inspection.permutation_importance*. Accessed: 2024-06-09. 2020. URL: https://scikit-learn.org/stable/modules/generated/sklearn.inspection.permutation_importance.html.

[20] xgboost developers. *XGBoost Documentation*. 2022. URL: https://xgboost.readthedocs.io/en/stable/.

[21] United Nations Office for Disaster Risk Reduction. *Pyroclastic Density Current*. https://www.preventionweb.net/understanding-disaster-risk/terminology/hips/gh0012. Accessed: 2024-05-26. 2024. URL: https://www.preventionweb.net/understanding-disaster-risk/terminology/hips/gh0012.

[22] E. W. Dualeh et al. “Analyzing Explosive Volcanic Deposits From Satellite-Based Radar Backscatter, Volcán de Fuego, 2018”. In: *Journal of Geophysical Research: Solid Earth* 126.9 (2021). e2021JB022250 2021JB022250, e2021JB022250. DOI: https://doi.org/10.1029/2021JB022250. eprint: https://agupubs.onlinelibrary.wiley.com/doi/pdf/10.1029/2021JB022250. URL: https://agupubs.onlinelibrary.wiley.com/doi/abs/10.1029/2021JB022250.

[23] Breard E.C.P., Dufek J., and Charbonnier S. “The fragmentation-induced fluidisation of pyroclastic density currents”. In: *Nature Communications* (2023). DOI: 10.1038/s41467-023-37867-1.

[24] Meredith E.S., Jenkins S.F., Hayes J.L., et al. “Damage assessment for the 2018 lower East Rift Zone lava flows of Kīlauea volcano, Hawai□i”. In: *Bulletin of Volcanology* 84.65 (2022). DOI: 10.1007/s00445-022-01568-2. URL: https://doi.org/10.1007/s00445-022-01568-2.

[25] European Space Agency. *Orthorectification*. Accessed: 2024-06-06. 2024. URL: https://step.esa.int/main/wp-content/help/versions/9.0.0/snap-toolboxes/org.esa.s1tbx.s1tbx.op.sar.processing.ui/operators/RangeDopplerGeocodingOp.html.

[26] European Space Agency. *Radiometric Calibration of Sentinel-1 Products*. Accessed: 2024-06-17. 2024. URL: https://sentinel.esa.int/documents/247904/685163/S1-Radiometric-Calibration-V1.0.pdf.

[27] European Space Agency. *Radiometric/Geometric Correction Workflow*. https://forum.step.esa.int/t/radiometric-geometric-correction-workflow/2540/71. Accessed: 2024-06-06. 2024.

[28] Filipponi Federico. “Sentinel-1 GRD Preprocessing Workflow”. In: *Proceedings* 18.1 (2019). ISSN: 2504-3900. DOI: 10.3390/ECRS-3-06201. URL: https://www.mdpi.com/2504-3900/18/1/11.

[29] James Gareth et al. *An Introduction to Statistical Learning: with Applications in R*. 2nd ed. Springer Texts in Statistics. Springer New York, NY, 2021. DOI: 10.1007/978-1-0716-1418-1. URL: https://doi.org/10.1007/978-1-0716-1418-1.

[30] Lerner Geoffrey, Cronin Shane, and Turner Gillian. “Evaluating emplacement temperature of a 1000-year sequence of mass flows using paleomagnetism of their deposits at Mt. Taranaki, New Zealand”. In: *Volcanica* 2 (Apr. 2019), pp. 11–24. DOI: 10.30909/vol.02.01.1124.

[31] Richard C. Ghail et al. “VenSAR on EnVision: Taking earth observation radar to Venus”. In: *International Journal of Applied Earth Observation and Geoinformation* 64 (2018), pp. 365–376. ISSN: 1569-8432. DOI: https://doi.org/10.1016/j.jag.2017.02.008. URL: https://www.sciencedirect.com/science/article/pii/S030324341730034X.

[32] Arney Giada et al. “Spatially resolved measurements of H2O, HCl, CO, OCS, SO2, cloud opacity, and acid concentration in the Venus near-infrared spectral windows”. In: *Journal of Geophysical Research: Planets* 119.8 (2014), pp. 1860–1891. DOI: https://doi.org/10.1002/2014JE004662. eprint: https://agupubs.onlinelibrary.wiley.com/doi/pdf/10.1002/2014JE004662. URL: https://agupubs.onlinelibrary.wiley.com/doi/abs/10.1002/2014JE004662.

[33] Lori S. Glaze, Stephen M. Baloga, and Jesse Wimert. “Explosive volcanic eruptions from linear vents on Earth, Venus and Mars: Comparisons with circular vent eruptions”. In: *National Aeronautics and Space Administration* (2010).

[34] Global Volcanism Program. *Report on Raung (Indonesia)*. https://volcano.si.edu/showreport.cfm?doi=10.5479/si.GVP.BGVN202106-223030. Accessed: 2024-05-26. 2021. DOI: 10.5479/si.GVP.BGVN202106-223030.

[35] Global Volcanism Program. “Report on Sinabung (Indonesia)”. In: *Bulletin of the Global Volcanism Network* 35.7 (2010). Ed. by Wunderman R. DOI: 10.5479/si.GVP.BGVN201007-261080. URL: https://doi.org/10.5479/si.GVP.BGVN201007-261080.

[36] Global Volcanism Program. *Report on Sinabung (Indonesia)*. https://volcano.si.edu/showreport.cfm?doi=10.5479/si.GVP.BGVN201401-261080. Accessed: 2024-05-26. 2014. DOI: 10.5479/si.GVP.BGVN201401-261080.

[37] Global Volcanism Program. *Report on Sinabung (Indonesia)*. https://volcano.si.edu/showreport.cfm?doi=10.5479/si.GVP.BGVN201804-261080. Accessed: 2024-05-26. 2018. DOI: 10.5479/si.GVP.BGVN201804-261080.

[38] Global Volcanism Program. *Report on Sinabung (Indonesia)*. https://volcano.si.edu/showreport.cfm?doi=10.5479/si.GVP.BGVN201809-261080. Accessed: 2024-05-26. 2018. DOI: 10.5479/si.GVP.BGVN201809-261080.

[39] Global Volcanism Program. *Report on Volcán de Fuego (Guatemala)*. https://volcano.si.edu/showreport.cfm?doi=10.5479/si.GVP.BGVN201808-342090. Accessed: 2024-05-26. 2018. DOI: 10.5479/si.GVP.BGVN201808-342090.

[40] Global Volcanism Program. *Volcán de Fuego*. https://volcano.si.edu/volcano.cfm?vn=342090. Accessed: 2024-05-26.

[41] Mryka Hall-Beyer. *GLCM Texture: A Tutorial*. Version v. 3.0. 2017. URL: https://prism.ucalgary.ca/server/api/core/bitstreams/8f9de234-cc94-401d-b701-f08ceee6cfdf/content.

[42] R. M. Haralick, K. Shanmugam, and I. Dinstein. "Textural Features for Image Classification". In: *IEEE Transactions on Systems, Man and Cybernetics* SMC-3.6 (1973), pp. 610–620. DOI: 10.1109/TSMC.1973.4309314.

[43] Andrew J.L. Harris and Scott K. Rowland. "Chapter 17 - Lava Flows and Rheology". In: *The Encyclopedia of Volcanoes (Second Edition)*. Ed. by Haraldur Sigurdsson. Second Edition. Amsterdam: Academic Press, 2015, pp. 321–342. ISBN: 978-0-12-385938-9. DOI: https://doi.org/10.1016/B978-0-12-385938-9.00017-1. URL: https://www.sciencedirect.com/science/article/pii/B9780123859389000171.

[44] Lammer Helmut et al. "What makes a planet habitable?" In: *Astronomy and Astrophysics Review* 17 (Apr. 2009), pp. 181–249. DOI: 10.1007/s00159-009-0019-z.

[45] Warren D. Huff, Lewis A. Owen, and Arianna Soldati. "2.13 - Volcanic Landforms". In: *Treatise on Geomorphology (Second Edition)*. Ed. by John (Jack) F. Shroder. Second Edition. Oxford: Academic Press, 2022, pp. 340–375. ISBN: 978-0-12-818235-2. DOI: https://doi.org/10.1016/B978-0-12-818234-5.00098-5. URL: https://www.sciencedirect.com/science/article/pii/B9780128182345000985.

[46] imbalanced-learn contributors. *RandomUnderSampler*. 2023. URL: URL:%20https://imbalanced-learn.org/stable/references/generated/imblearn.under_sampling.RandomUnderSampler.html.

[47] Mufungizi Innocent et al. "Petrography and geochemistry of Nyiragongo volcanic flows from 2002 and 2021: A comparative study". In: (2023). DOI: 10.21203/rs.3.rs-3794109/v1.

[48] James Jasperine et al. "Analysis of Features in SAR Imagery Using GLCM Segmentation Algorithm". In: *Data Science: Theory, Algorithms, and Applications*. Ed. by Verma Gyanendra K. et al. Singapore: Springer Singapore, 2021, pp. 253–266. ISBN: 978-981-16-1681-5. DOI: 10.1007/978-981-16-1681-5_16. URL: https://doi.org/10.1007/978-981-16-1681-5_16.

[49] Jet Propulsion Laboratory. "Chapter 1 Synthetic Aperture Radars (SAR) Imaging Basics". In: URL: https://api.semanticscholar.org/CorpusID:18199098.

[50] Lee Jeyun, Jung Seong-Woo, and Hong Sang-Hoon. "Mapping lava flow from the Kilauea eruption of 2018 in the east rift zone using space-based synthetic aperture radar". In: *GIScience & Remote Sensing* 60 (2023). DOI: 10.1080/15481603.2023.2176275.

[51] Lee Jong-Sen et al. "Improved Sigma filter for speckle filtering of SAR imagery". In: *IEEE Transactions on Geoscience and Remote Sensing* (2015). DOI: 10.1109/TGRS.2008.2002881.

[52] James F. Kasting and David Catling. “Evolution of a Habitable Planet”. In: *Annual Review of Astronomy and Astrophysics* 41.Volume 41, 2003 (2003), pp. 429–463. ISSN: 1545-4282. DOI: https://doi.org/10.1146/annurev.astro.41.071601.170049. URL: https://www.annualreviews.org/content/journals/10.1146/annurev.astro.41.071601.170049.

[53] Stapor Katarzyna. “Evaluating and Comparing Classifiers: Review, Some Recommendations and Limitations”. In: May 2017, pp. 12–21. ISBN: 978-3-319-59161-2. DOI: 10.1007/978-3-319-59162-9_2.

[54] I Kusmartini et al. “Elemental characterization of Mt. Sinabung volcanic ash, Indonesia by Neutron Activation Analysis”. In: *Journal of Physics: Conference Series* 860.1 (June 2017), p. 012005. DOI: 10.1088/1742-6596/860/1/012005. URL: https://dx.doi.org/10.1088/1742-6596/860/1/012005.

[55] Yi Lin and Yongho Jeon. “Random Forests and Adaptive Nearest Neighbors”. In: *Journal of the American Statistical Association* 101.474 (2006), pp. 578–590. ISSN: 01621459. URL: http://www.jstor.org/stable/27590719 (visited on 06/24/2024).

[56] Patrick M.R., Houghton B.F., Anderson K.R., et al. “The cascading origin of the 2018 Kīlauea eruption and implications for future forecasting”. In: *Nature Communications* 11.5646 (2020). DOI: 10.1038/s41467-020-19190-1. URL: https://doi.org/10.1038/s41467-020-19190-1.

[57] O’Byrne Michael et al. “Texture Analysis based Detection and Classification of Surface Features on Ageing Infrastructure Elements”. In: *BCRI2012 Bridge & Concrete Research in Ireland*. Cork, Ireland, 2012. URL: https://hal.science/hal-01009012.

[58] Iqbal N. et al. “Gray level co-occurrence matrix (GLCM) texture based crop classification using low altitude remote sensing platforms”. In: *PeerJ. Computer science* 7 (2021), e536. DOI: 10.7717/peerj-cs.536. URL: https://doi.org/10.7717/peerj-cs.536.

[59] NASA. *NASA Damage Map Shows Effects of Destructive Guatemala Volcano Eruption*. https://www.jpl.nasa.gov/images/pia22532-nasa-damage-map-shows-effects-of-destructive-guatemala-volcano-eruption. Accessed: 2024-05-26. 2018. URL: https://www.jpl.nasa.gov/images/pia22532-nasa-damage-map-shows-effects-of-destructive-guatemala-volcano-eruption.

[60] Natural Resources Canada. *Radar Image Distortions*. Accessed: 2024-06-06. 2024. URL: https://natural-resources.canada.ca/maps-tools-and-publications/satellite-imagery-elevation-data-and-air-photos/tutorial-fundamentals-remote-sensing/microwave-remote-sensing/radar-image-distortions/9325.

[61] Pacific Northwest Seismic Network. *Pyroclastic Flows*. https://www.pnsn.org/outreach/volcanichazards/pyroclastic-flows. Accessed: 2024-05-26. 2024. URL: https://www.pnsn.org/outreach/volcanichazards/pyroclastic-flows.

[62] Mark S. Nixon and Alberto S. Aguado. “Chapter 8 - Introduction to texture description, segmentation, and classification”. In: *Feature Extraction and Image Processing for Computer Vision (Third Edition)*. Ed. by Mark S. Nixon and Alberto S. Aguado. Third Edition. Oxford: Academic Press, 2012, pp. 399–434. ISBN: 978-0-12-396549-3. DOI: https://doi.org/10.1016/B978-0-12-396549-3.00008-2. URL: https://www.sciencedirect.com/science/article/pii/B9780123965493000082.

[63] Nuclear Power contributors. *Electron-Hole Pair - Properties of Semiconductors*. Accessed: 2024-06-17. 2024. URL: https://www.nuclear-power.com/nuclear-engineering/radiation-detection/semiconductor-detectors/what-are-semiconductors-properties-of-semiconductors/electron-hole-pair/.

[64] Roche Olivier et al. “Long-runout pyroclastic density currents: Analysis and implications”. In: *Geology* 50.10 (July 2022), pp. 1172–1176. DOI: 10.1130/G50215.1. URL: https://uca.hal.science/hal-03792847.

[65] Poland Michael P. “Synthetic aperture radar volcanic flow maps (SAR VFMs): a simple method for rapid identification and mapping of volcanic mass flows”. In: *Bulletin of Volcanology* 84.32 (2022). DOI: 10.1007/s00445-022-01539-7. URL: https://doi.org/10.1007/s00445-022-01539-7.

[66] Ardila López Juan Pablo. *Assessment and modeling of angular backscattering variation in ALOS ScanSAR images over tropical forest areas*. Accessed: 2024-06-06. 2008. URL: https://webapps.itc.utwente.nl/librarywww/papers_2008/msc/gfm/ardilalopez.pdf.

[67] Dellino Pierfrancesco, Dioguardi Fabio, Isaia Roberto, et al. “The impact of pyroclastic density currents duration on humans: the case of the AD 79 eruption of Vesuvius”. In: *Scientific Reports* 11 (2021). DOI: 10.1038/s41598-021-84456-7. URL: https://www.nature.com/articles/s41598-021-84456-7.

[68] Shaoqing Ren et al. “Global refinement of random forest”. In: *2015 IEEE Conference on Computer Vision and Pattern Recognition (CVPR)*. 2015, pp. 723–730. DOI: 10.1109/CVPR.2015.7298672.

[69] Caballero Gabriel Rodrigo et al. “Assessment of Multi-Date Sentinel-1 Polarizations and GLCM Texture Features Capacity for Onion and Sunflower Classification in an Irrigated Valley: An Object Level Approach”. In: *Agronomy* 10.6 (2020). ISSN: 2073-4395. DOI: 10.3390/agronomy10060845. URL: https://www.mdpi.com/2073-4395/10/6/845.

[70] Sandatlas. *Types of Lava Flows*. https://www.sandatlas.org/types-lava-flows/. Accessed: 2024-05-26. 2024. URL: https://www.sandatlas.org/types-lava-flows/.

[71] School of Ocean and Earth Science and Technology, University of Hawaii at Manoa. *Kilauea Lava*. https://www.soest.hawaii.edu/GG/ASK/kilauea-lava.html. Accessed: 2024-05-26. 2024.

[72] Richard A. Schultz et al. “Interpretation and analysis of planetary structures”. In: *Journal of Structural Geology* 32.6 (2010), pp. 855–875. ISSN: 0191-8141. DOI: https://doi.org/10.1016/j.jsg.2009.09.005. URL: https://www.sciencedirect.com/science/article/pii/S019181410900203X.

[73] Mount St. Helens Science and Learning Center. *Lahars Gallery*. https://www.mshslc.org/gallery/lahars/. Accessed: 2024-05-26. 2024. URL: https://www.mshslc.org/gallery/lahars/.

[74] National Academies of Sciences Engineering and Medicine. *Planetary Protection Considerations for Missions to Solar System Small Bodies: Report Series—Committee on Planetary Protection*. Washington, DC: The National Academies Press, 2023. ISBN: 978-0-309-69372-1. DOI: 10.17226/26714. URL: https://nap.nationalacademies.org/catalog/26714/planetary-protection-considerations-for-missions-to-solar-system-small-bodies.

[75] scikit-image contributors. *scikit-image: Image processing in Python*. 2023. URL: URL:%20https://scikit-image.org/docs/stable/api/skimage.feature.html#skimage.feature.graycomatrix.

[76] Valade Sébastien et al. “Towards Global Volcano Monitoring Using Multisensor Sentinel Missions and Artificial Intelligence: The MOUNTS Monitoring System”. In: *Remote Sensing* 11.13 (2019). ISSN: 2072-4292. DOI: 10.3390/rs11131528. URL: https://www.mdpi.com/2072-4292/11/13/1528.

[77] Sentinel Hub. *EO Browser*. Accessed: 2024-06-24. 2024. URL: https://apps.sentinel-hub.com/eo-browser.

[78] National Park Service. *Geology of Texas - Section 5: Cenozoic Era*. http://npshistory.com/publications/geology/state/tx/2000-DE02/sec5.htm. Accessed: 2024-05-26. 2024. URL: http://npshistory.com/publications/geology/state/tx/2000-DE02/sec5.htm.

[79] National Park Service. *Lava Flow Forms*. https://www.nps.gov/articles/000/lava-flow-forms.htm. Accessed: 2024-05-26. 2024. URL: https://www.nps.gov/articles/000/lava-flow-forms.htm.

[80] National Park Service. *Lava Lakes*. https://www.nps.gov/articles/000/lava-lakes.htm. Accessed: 2024-05-26. 2024. URL: https://www.nps.gov/articles/000/lava-lakes.htm.

[81] Carn Simon. "Application of synthetic aperture radar (SAR) imagery to volcano mapping in the humid tropics: a case study in East Java, Indonesia". In: *Bulletin of Volcanology* 61 (July 1999), pp. 92–105. DOI: 10.1007/s004450050265. URL: https://doi.org/10.1007/s004450050265.

[82] Marvin K. Simon. *Bandwidth-Efficient Digital Modulation with Application to Deep-Space Communications*. DESCANO, 2001.

[83] David Small. "Flattening Gamma: Radiometric Terrain Correction for SAR Imagery". In: *IEEE Transactions on Geoscience and Remote Sensing* 49.8 (2011), pp. 3081–3093. DOI: 10.1109/TGRS.2011.2120616.

[84] Akhmad Solikhin et al. "Mapping the 2010 Merapi pyroclastic deposits using dual-polarization Synthetic Aperture Radar (SAR) data". In: *Remote Sensing of Environment* 158 (2015), pp. 180–192. ISSN: 0034-4257. DOI: https://doi.org/10.1016/j.rse.2014.11.002. URL: https://www.sciencedirect.com/science/article/pii/S0034425714004386.

[85] U.S. Geological Survey. *Chapter 10: Summary and Conclusions*. https://pubs.usgs.gov/pp/1769/chapters/p1769_chapter10.pdf. Accessed: 2024-05-26. 2024. URL: https://pubs.usgs.gov/pp/1769/chapters/p1769_chapter10.pdf.

[86] U.S. Geological Survey. *Lahars: The Most Threatening Volcanic Hazard in the Cascades*. https://www.usgs.gov/observatories/cvo/science/lahars-most-threatening-volcanic-hazard-cascades. Accessed: 2024-05-26. 2024. URL: https://www.usgs.gov/observatories/cvo/science/lahars-most-threatening-volcanic-hazard-cascades.

[87] U.S. Geological Survey. *The Mobility of Basalt Lava Flows*. https://pubs.usgs.gov/of/1997/of97-724/lavacool.html. Accessed: 2024-05-26. 2024. URL: https://pubs.usgs.gov/of/1997/of97-724/lavacool.html.

[88] Terunuma T. et al. "Detection of traces of pyroclastic flows and lahars with satellite synthetic aperture radars". In: *International Journal of Remote Sensing* 26.9 (2005), pp. 1927–1942. DOI: 10.1080/01431160512331326576.

[89] Ui T. "Discrimination Between Debris Avalanches and Other Volcaniclastic Deposits". In: *Volcanic Hazards*. Berlin Heidelberg: Springer Berlin Heidelberg, 1989, pp. 201–209. ISBN: 978-3-642-73759-6.

[90] The Washington Post. *Mount Nyiragongo Eruption in Congo*. https://www.washingtonpost.com/photography/interactive/2021/mount-nyiragongo-volcano-eruption-congo/. Accessed: 2024-05-26. 2021.

[91] GRS TUDelft. *DRAMA GitLab Repository*. https://gitlab.tudelft.nl/drama/drama. Accessed: 2024-06-06. 2024.

[92] U.S. Geological Survey. *GIS Shapefiles for the June 27th Lava Flow at Kīlauea Volcano, Hawai'i, June 2014 - June 2016*. https://www.usgs.gov/data/gis-shapefiles-june-27th-lava-flow-kilauea-volcano-hawaii-june-2014-june-2016. Accessed: 2024-05-26. 2024.

[93] U.S. Geological Survey. *Kīlauea 2018 Lower East Rift Zone (LERZ) Eruption Locations*. https://www.sciencebase.gov/catalog/item/5cdd9871e4b029273746360f. Accessed: 2024-05-26. 2019.

[94] U.S. Geological Survey. *Lava Flow Hazard Map for Kīlauea, Island of Hawai'i, Hawaii, 2019*. Accessed: 2024-06-26. 2019. URL: https://data.usgs.gov/datacatalog/data/USGS:5cdd9871e4b029273746360f.

[95] *Volcán de Fuego*. https://www.wikiwand.com/en/Volcán_de_Fuego. Accessed: 2024-05-26.

[96] C. Wade and K. Glynn. *Hands-On Gradient Boosting with XGBoost and scikit-learn: Perform accessible machine learning and extreme gradient boosting with Python*. Packt Publishing, 2020. ISBN: 9781839213809. URL: https://books.google.nl/books?id=2tcDEAAAQBAJ.

[97] Li Weiran, Lhermitte Stef, and Lopez Dekker Paco. "The potential of synthetic aperture radar interferometry for assessing meltwater lake dynamics on Antarctic ice shelves". In: *The Cryosphere* 15 (Dec. 2021), pp. 5309–5322. DOI: 10.5194/tc-15-5309-2021.

[98] Wikipedia contributors. *Bias–variance tradeoff*. Accessed: 2024-06-08. 2023. URL: https://en.wikipedia.org/wiki/Bias%E2%80%93variance_tradeoff.

[99] R.D. Wordsworth. "Atmospheric nitrogen evolution on Earth and Venus". In: *Earth and Planetary Science Letters* 447 (2016), pp. 103–111. ISSN: 0012-821X. DOI: https://doi.org/10.1016/j.epsl.2016.04.002. URL: https://www.sciencedirect.com/science/article/pii/S0012821X16301583.

[100] Wulandari Y, Sagala S, and Sullivan Gavin. "The Role of Community-Based Organization in Disaster Response at Mt. Sinabung". In: *IOP Conference Series: Earth and Environmental Science* 158 (May 2018), p. 012035. DOI: 10.1088/1755-1315/158/1/012035.

[101] Liu Yangguang et al. "A Strategy on Selecting Performance Metrics for Classifier Evaluation". In: *Int. J. Mob. Comput. Multimed. Commun.* 6.4 (2014), pp. 20–35. ISSN: 1937-9412. DOI: 10.4018/IJMCMC.2014100102. URL: https://doi.org/10.4018/IJMCMC.2014100102.

A

Source Code

```
def calculate_texture_features_vectorized(image, window_size=5):
    """
    Calculate texture features for an image using a sliding window approach.

    Parameters:
    - image: 2D numpy array
        The input grayscale image for which texture features are to be calculated.
    - window_size: int, optional (default=5)
        The size of the sliding window. Must be an odd integer to ensure a center
            pixel.

    Returns:
    - features: dict
        A dictionary containing four 3D numpy arrays for texture features:
        'contrast', 'dissimilarity', 'homogeneity', and 'ASM' (Angular Second
            Moment).
        Each array has a shape (height, width, 5) where the third dimension
            contains
        the texture feature values for four angles and their mean.
    """

    # Pad the image to handle borders
    pad_width = window_size // 2
    padded_image = np.pad(image, pad_width, mode='reflect')

    # Create overlapping windows using view_as_windows
    windows = view_as_windows(padded_image, (window_size, window_size))

    # Initialize the feature dictionary
    shape = image.shape
    features = {
        'contrast': np.zeros((shape[0], shape[1], 5)),
        'dissimilarity': np.zeros((shape[0], shape[1], 5)),
        'homogeneity': np.zeros((shape[0], shape[1], 5)),
        'ASM': np.zeros((shape[0], shape[1], 5))
    }
    angles = [0, np.pi/4, np.pi/2, 3*np.pi/4]  # Define the angles for GLCM
        calculation

    for i in range(shape[0]):
        for j in range(shape[1]):

            window = windows[i, j]

            # Skip processing if any NaN values are found in the window
            if np.isnan(window).any():
                continue

            window = window.astype(np.uint8)  # Convert window to uint8 type

```

```
            # Calculate the Gray-Level Co-occurrence Matrix (GLCM)
            glcm = graycomatrix(window, [1], angles, levels=256, symmetric=True,
                normed=True)

            # Calculate texture properties from the GLCM
            for name in features.keys():
                prop_values = graycoprops(glcm, name)[0]
                for k in range(4):
                    features[name][i, j, k] = prop_values[k]
                features[name][i, j, 4] = np.mean(prop_values)  # Store the mean
                    value of properties

    return features
```

```
def equal_probability_quantisation(image, polarisation, global_max_VV,
    global_max_VH, num_levels=16):
    """
    Perform equal probability quantisation on an image based on the specified
        polarisation.

    Parameters:
    - image: 2D numpy array
        The input image to be quantised.
    - polarisation: str
        The polarisation type of the image, either 'VV' or 'VH'.
    - global_max_VV: float
        The global maximum value for 'VV' polarisation.
    - global_max_VH: float
        The global maximum value for 'VH' polarisation.
    - num_levels: int, optional (default=16)
        The number of quantisation levels.

    Returns:
    - full_quantised_image: 2D numpy array
        The quantised image with the same shape as the input image.
    """

    # Normalise the image based on the specified polarisation and its global
        maximum
    if polarisation == 'VV':
        normalised_image = (image / global_max_VV) * 255
    elif polarisation == 'VH':
        normalised_image = (image / global_max_VH) * 255
    else:
        raise ValueError("Polarisation must be either 'VV' or 'VH'")

    # Flatten the image, excluding NaN values
    flattened_image = normalized_image[~np.isnan(normalized_image)].ravel()

    # Calculate the histogram and cumulative distribution function (CDF)
    histogram, bin_edges = np.histogram(flattened_image, bins=256, range=(0, 256))
    cdf = histogram.cumsum()
    cdf_normalised = cdf / cdf[-1]

    # Determine quantisation thresholds using linear interpolation
    thresholds = np.interp(np.linspace(0, 1, num_levels + 1), cdf_normalised,
        bin_edges[:-1])

    # Initialise the quantised image array with NaN values
    quantised_image = np.full_like(flattened_image, np.nan)

    # Quantise the flattened image based on the determined thresholds
    for i in range(num_levels):
        low = thresholds[i]
        high = thresholds[i + 1]
```

```
        mask = (flattened_image >= low) & (flattened_image < high)
        quantised_image[mask] = int((i / (num_levels - 1)) * 255)

    # Create a full-size quantised image with the original NaN values
    full_quantised_image = np.full_like(normalised_image, np.nan)
    full_quantised_image[~np.isnan(normalised_image)] = quantised_image

    return full_quantised_image
```

```
from drama import utils as drtls

def moving_average(data, Naz, Nrg, downsample=False):
    """
    Apply a moving average filter to a 2D numpy array.

    Parameters:
    - data: 2D numpy array
        The input data to be filtered.
    - Naz: int
        The number of samples averaged in the azimuth (first) dimension.
    - Nrg: int
        The number of samples averaged in the range (second) dimension.
    - downsample: bool, optional (default=False)
        If True, downsample the data after averaging.

    Returns:
    - filt_data: 2D numpy array
        The filtered (and possibly downsampled) data.
    """
    # Apply smoothing in the range dimension
    filt_data = drtls.smooth(data, Nrg, axis=1)
    # Apply smoothing in the azimuth dimension
    filt_data = drtls.smooth(filt_data, Naz, axis=0)

    # Downsample the data if requested
    if downsample:
        filt_data = filt_data[int(Naz/2)::Naz, int(Nrg/2)::Nrg]

    return filt_data

# Calculate the local variance for the 'VV' polarisation
nrcs_var = moving_average(VV**2, 4, 4) - moving_average(VV, 4, 4)**2
loc_var_VV = np.sqrt(nrcs_var) / moving_average(VV, 4, 4)
```

```
#Model 1 implementation
from sklearn.model_selection import train_test_split
from sklearn.ensemble import RandomForestClassifier
from imblearn.pipeline import Pipeline as IMBPipeline
from imblearn.over_sampling import SMOTE
from imblearn.under_sampling import RandomUnderSampler
labels = {'deposit':0, 'background': 1}
sampling_strategy_oversample = {labels['deposit']: 1000000}  # Target number for
    PDC pixels
sampling_strategy_undersample = {labels['background']: 1000000}  # Target number
    for background pixels
X_train, X_test, y_train, y_test = train_test_split(X_all_df_no_nan, y_all_no_nan,
     test_size=0.2, random_state=29)
pipeline_step1 = IMBPipeline(steps=[
    ('oversample', SMOTE(sampling_strategy=sampling_strategy_oversample)),
    ('undersample', RandomUnderSampler(sampling_strategy=
        sampling_strategy_undersample)),
    ('classifier', RandomForestClassifier(n_estimators=200, n_jobs=-1,
        random_state=29))
])
# Training the model
```

```
pipeline_step1.fit(X_train, y_train)
# Predicting on the test set
y_pred_step1 = pipeline_step1.predict(X_test)
# Probability predictions for performance metrics
y_prob_step1 = pipeline_step1.predict_proba(X_test)[:, 1]
```

```
#Model 2 implementation
from xgboost import XGBClassifier
labels_step2 = {'PDC': 0, 'lava': 1}
sampling_strategy_oversample_2 = {labels_step2['PDC']: 540000}  # Target number for PDC pixels
X_train_2, X_test_2, y_train_2, y_test_2 = train_test_split(X_all_df_no_nan_2, y_all_no_nan_2, test_size=0.2, random_state=14)
pipeline_step2 = IMBPipeline(steps=[
    ('oversample', SMOTE(sampling_strategy=sampling_strategy_oversample_2, random_state=4)),
    ('classifier', XGBClassifier(n_estimators=200, max_depth=3, learning_rate=0.005, gamma=1, colsample_bytree=0.8, reg_alpha=1, reg_lambda=5, min_child_weight=5, n_jobs=-1, random_state=64))
])
# Training the model
pipeline_step2.fit(X_train_2, y_train_2)
# Predicting on the test set
y_pred_step2 = pipeline_step2.predict(X_test_2)
# Probability predictions for performance metrics
y_prob_step2 = pipeline_step2.predict_proba(X_test_2)[:, 1]
```

B

Appendix B

B.1. Equal Probability Quantisation

Equal probability quantisation (EPQ) is designed to map the pixel values of an image into a specified number of levels such that each level has an approximately equal number of pixels. This process involves the following steps:

1. Normalise the image: Scale the image values to a common range, usually 0-255 for grayscale images.
2. Compute Histogram and CDF: Calculate the histogram of the normalised image and the cumulative distribution function (CDF).
3. Determine Thresholds: Establish quantisation thresholds based on the CDF to ensure that each quantised level has an equal number of pixels.
4. Quantise the Image: Assign pixel values to quantised levels based on the determined thresholds.

The amount of levels used in this study are sixteen (16).

B.1.1. Impact on Relative Distribution

- **Original Relative Distribution:** The original relative distribution of pixel values reflects the natural variations in the intensity levels of the image.
- **After EPQ:** The EPQ method alters this distribution to achieve a uniform distribution across the quantised levels. This means that the original relative proportions of different intensity levels are not preserved. Instead, the intensity values are redistributed to ensure that each quantised level has an equal number of pixels.

A simple normalisation method includes dividing the image values by a global maximum and multiply them by 255. To understand the difference between simple normalisation and EPQ, Figure B.1 presents the case of Kilauea. The original distribution of pixel intensities is preserved during the simple normalisation, however, due to the use of a global maximum, the values are scaled only between 0 and 150, not taking advantage of all the available levels. With equal probability, the values are spread over the entire range.

To visually inspect the impact of equal probability quantisation on texture feature maps the case of Nyiragongo is presented in Figure B.2. It is evident that the equal probability technique has preserved the texture of the deposit better compared to the simple normalisation. This also results in more appealing results in the GLCM-derived features as shown in the contrast example in Figure B.3.

B.1.2. Advantages

- Uniform Quantisation Levels: EPQ ensures that each quantised level is equally represented, which can enhance the visibility of texture features by reducing the dominance

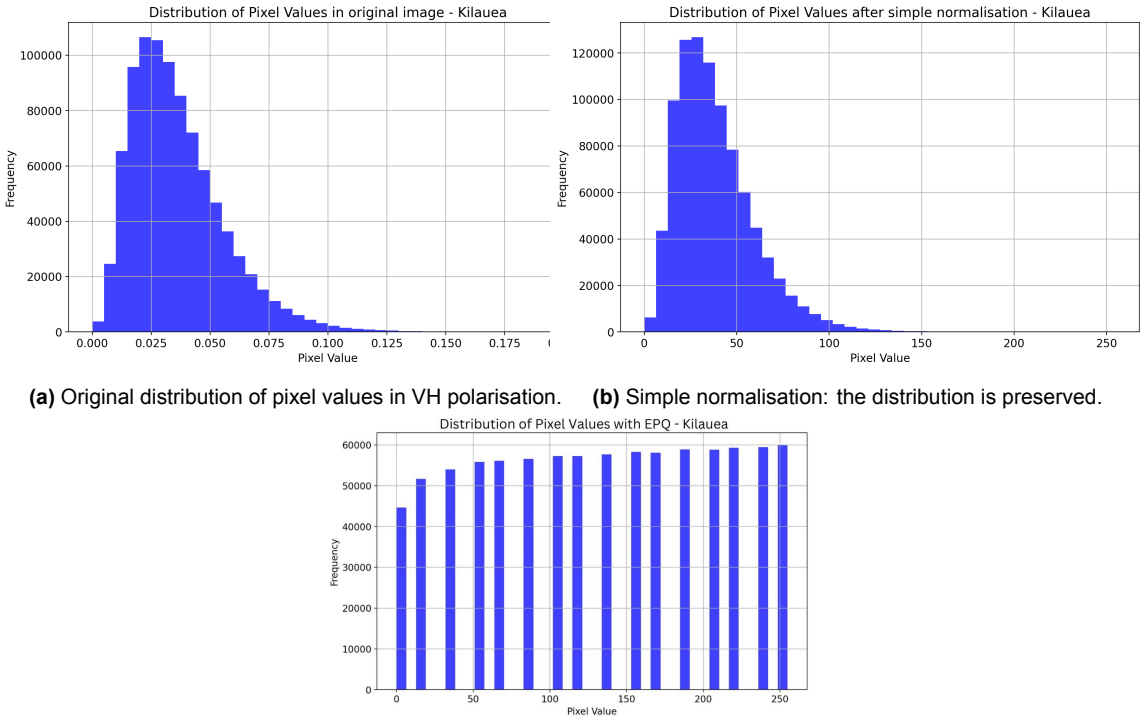

(a) Original distribution of pixel values in VH polarisation. **(b)** Simple normalisation: the distribution is preserved.

(c) Equal probability: the values are redistributed.

Figure B.1: Pixel value distribution for the case of Kilauea (VH polarisation). The equal probability quantisation method does not preserve the original distribution.

of certain intensity ranges.

- Robustness to Monotonic Transformations: Because EPQ is based on the CDF, it is less sensitive to monotonic transformations like brightness changes, preserving the overall texture characteristics better.

B.1.3. Disadvantages

- Loss of Original Distribution: The primary drawback is the loss of the original relative distribution of pixel intensities. This can lead to a different perception of contrast and texture compared to the original image.

B.1.4. Mathematical Formulation

Step 1: Normalise the Image

Given an image I with intensity values, normalise the pixel values to a common range, such as $[0, 255]$:

$$I_{\text{normalised}} = \left(\frac{I}{\text{global\_max}} \right) \times 255$$

Here, global_max is the predefined global maximum intensity value.

Step 2: Compute Histogram and CDF

Calculate the histogram H of the normalised image and the cumulative distribution function (CDF) F:

$$H(i) = \sum_{x,y} \delta(I_{\text{normalised}}(x, y) - i)$$

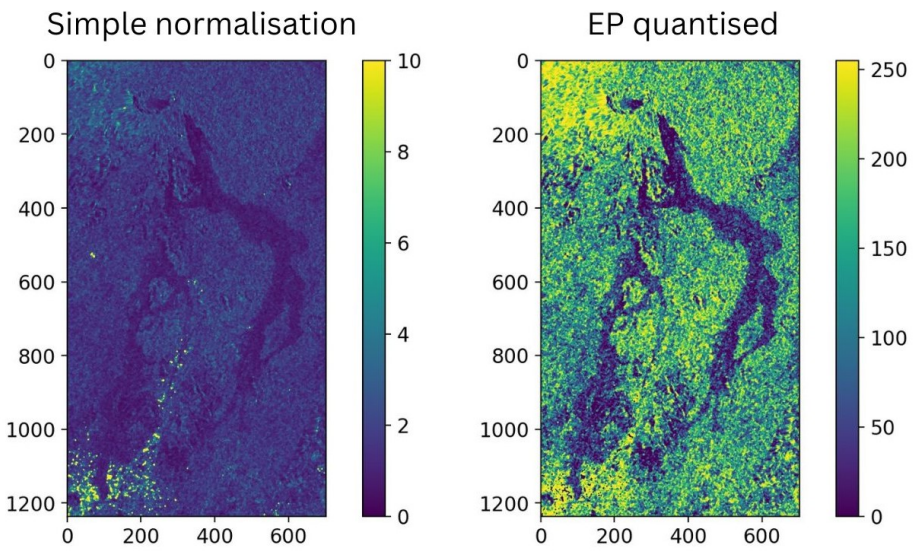

Figure B.2: Nyiragongo case. Left: simple normalisation; right: equal probability. The texture features have been preserved better in the right image. Note that with simple normalisation the values are concentrated on the low end of the grayscale.

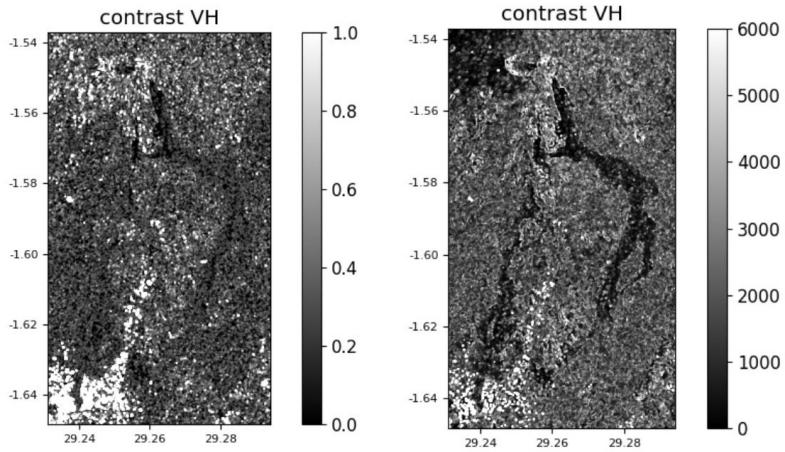

Figure B.3: Contrast VH - Nyiragongo case. Left: simple normalisation; right: equal probability. In this case, the texture features have been preserved better in the right image.

$$F(i) = \sum_{j=0}^{i} H(j)$$

Normalise the CDF:

$$F_{\text{normalised}}(i) = \frac{F(i)}{F(255)}$$

Step 3: Determine Quantisation Thresholds

Establish quantisation thresholds T based on the normalised CDF to ensure equal probability levels:

$$T_k = \text{interp}\left(\frac{k}{L}, F_{\text{normalised}}, \text{bin\_edges}\right)$$

Here, L is the number of quantisation levels, bin_edges are the edges of the histogram bins, and interp denotes linear interpolation.

Step 4: Quantise the Image
Assign pixel values to quantised levels based on the determined thresholds:

$$I_{\text{quantised}}(x,y) = \sum_{k=0}^{L-1} \left[\frac{k}{L-1} \times 255 \right] \cdot (T_k \leq I_{\text{normalised}}(x,y) < T_{k+1})$$

B.2. Gray Level Co-occurrence Matrix (GLCM) computation

In this study, the GLCM is computed for sub-images obtained through a sliding window approach.

The original image was first normalised by dividing each pixel value by the polarisation-specific global maximum and scaling the result to a range between 0 and 255; commonly referred to as the greyscale range. Then, using Equal Probability Quantisation (EPQ) as described above, the quantised image used as input for the GLCM can be constructed. Using the *scikit-image* library, one can obtain the four-dimensional (4D) array representing the grey-level co-occurrence histogram. The histogram $P[i,j,d,\theta]$ defines how frequently a pixel with grey-level i occurs at a distance d and angle θ from a pixel with grey-level j [75]. To facilitate reading, a visual example is presented in Figure B.4 and Figure B.5.

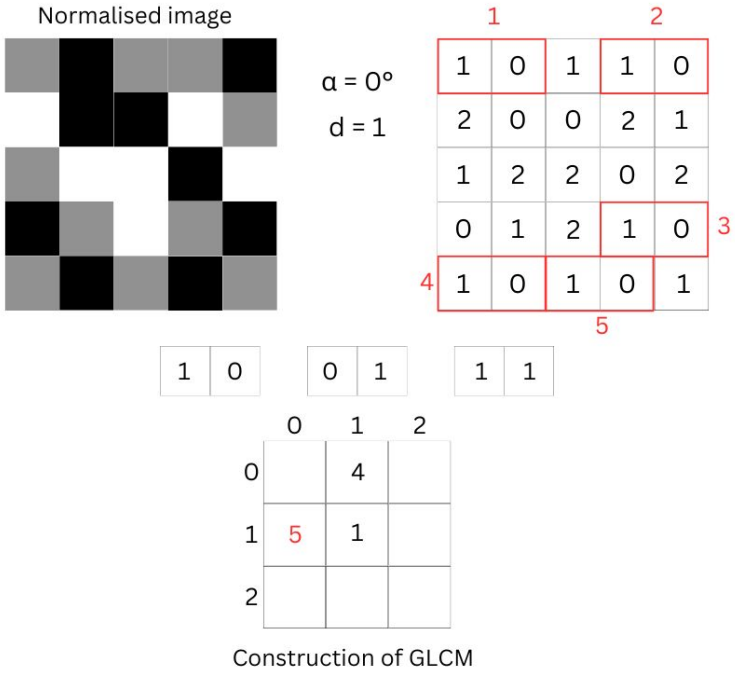

Figure B.4: Simple GLCM construction example within a 5x5 window for angle 0° and distance 1. On the left, the normalised image, where it is represented by values between 0 and 255. To construct the matrix, one counts how many times a pixel with value i has a pixel with value j next to it in that sequence. There are five (5) instances of the pair (1,0).

The user may select the distance(s) and angle(s) at which the spatial relationships are most prominent. For this study, all four principal angles were used, with the pixel relationship set at adjacent pixels (d=1). According to Haralick, Shanmugam, and Dinstein [42], the four directions are:

- **0° (Horizontal)**: Pairs of pixels are analyzed horizontally.

- **45° (Diagonal)**: Pairs of pixels are analyzed from bottom-left to top-right.
- **90° (Vertical)**: Pairs of pixels are analyzed vertically (bottom to top).
- **135° (Anti-Diagonal)**: Pairs of pixels are analyzed from bottom-right to top-left.

In the example of Figure B.4 the GLCM is constructed for a distance one and angle zero degrees(0°). Using multiple angles helps assess the directional texture without varying the spatial relationship distance, which is helpful in understanding texture variations in different directions across a localised area. In addition to the principal directions, the mean texture values across all angles are also calculated to obtain a fifth map. Calculating the mean of the texture features across multiple angles ensures rotation invariance, which is important because, while not strictly necessary, the definition of texture does not imply knowledge of orientation but could be presumed to include it [62]. This averaging process provides a generalised and robust representation of the texture features that captures the overall textural properties of the image without being biased towards any particular orientation. In the context of classification, this approach eliminates the need for aligning images to a common orientation, ensuring consistent and accurate analysis regardless of the image's directional alignment.

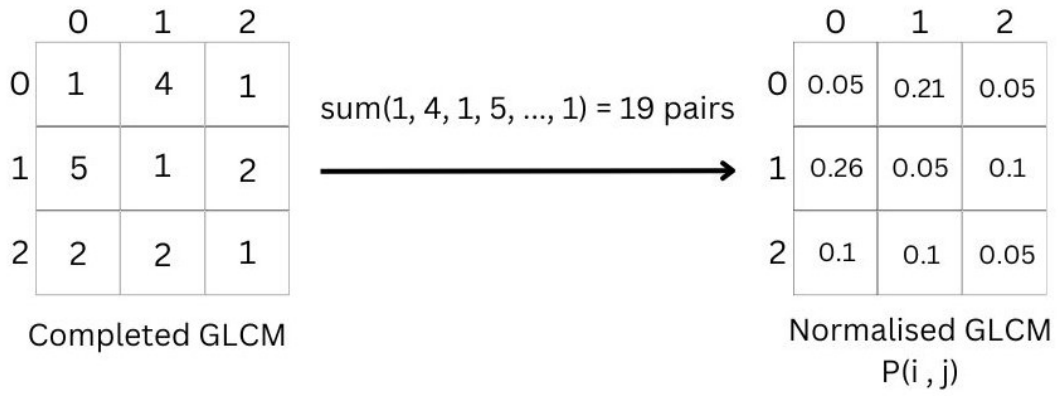

Figure B.5: Completed and normalised GLCM P(i,j). The normalised matrix values represent the probability of a certain pair occurring in a given image, following a certain positional relationship. It sums up to one (1).

Each matrix is then normalised to sum to one (1) as shown in Figure B.5, converting it into a probability distribution of pixel pair occurrences. This normalisation ensures that the GLCM reflects relative frequencies or probabilities rather than absolute counts, making the texture measures derived from the GLCM more comparable across different images or regions within an image, especially when those images or regions have varying scales, brightness, or contrast levels.

The window size used to create the textural map is centred around the target pixel to include a symmetrical area. The size of the window determines the extent of the surrounding area considered in the texture analysis. A larger window size includes more of the surrounding context but may be less sensitive to small-scale texture variations.

Deriving Texture Features

Four texture features were selected to create texture maps to aid in classification. Each feature provides different information about the spatial distribution of pixel intensities within the image.

- **Contrast:** It measures the intensity contrast between a pixel and its neighbour over the entire image, highlighting areas of high variability in intensity values [48]. It is computed as:

$$\text{Contrast} = \sum_{i,j} (i-j)^2 P(i,j) \tag{B.1}$$

- **Homogeneity:** Also known as the inverse difference moment [58]. It measures smoothness of the intensity distribution in the image. Its values range between zero (0) and one (1), with one indicating regions of uniform intensity [57]. Clearly, if contrast is low, homogeneity will be high. It is mathematically described by:

$$\text{Homogeneity} = \sum_{i,j} \frac{P(i,j)}{1+(i-j)^2} \tag{B.2}$$

- **Dissimilarity:** This feature is similar to contrast but less sensitive to significant differences in intensity. It is a linear measure of the local variations in the image [58]. Calculated as:

$$\text{Dissimilarity} = \sum_{i,j} |i-j| P(i,j) \tag{B.3}$$

- **Angular Second Moment (ASM):** It measures textural uniformity in an image. Its values, similar to homogeneity, range between zero and one. Higher values indicate homogeneous regions with low complexity and appear when the gray level distribution exhibits a consistent periodic pattern [58]. Equation B.2 shows how this metric is computed.

$$\text{ASM} = \sum_{i,j} P(i,j)^2$$

C

Appendix C

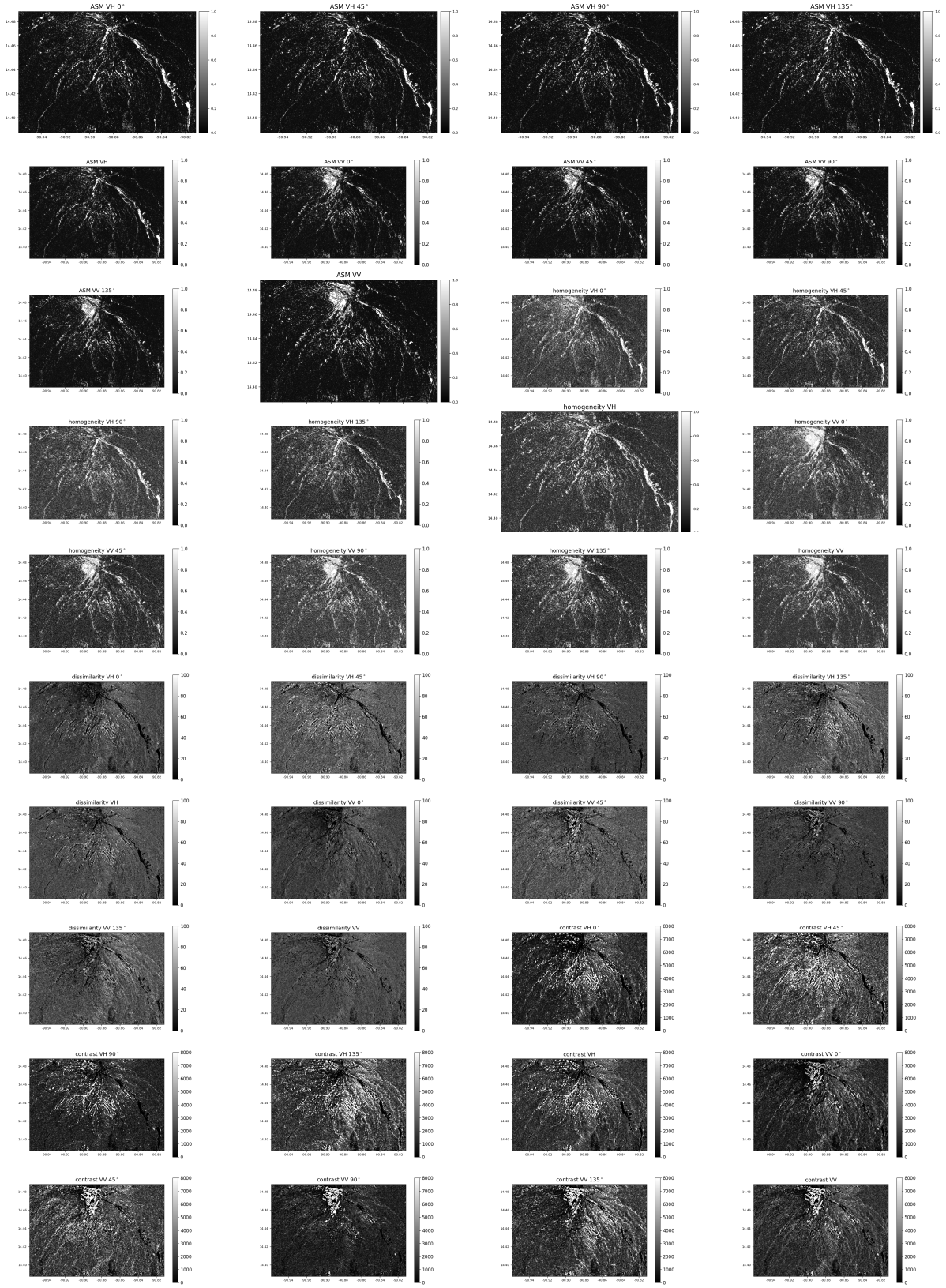

Figure C.1: Fuego Case Study GLCM feature maps.

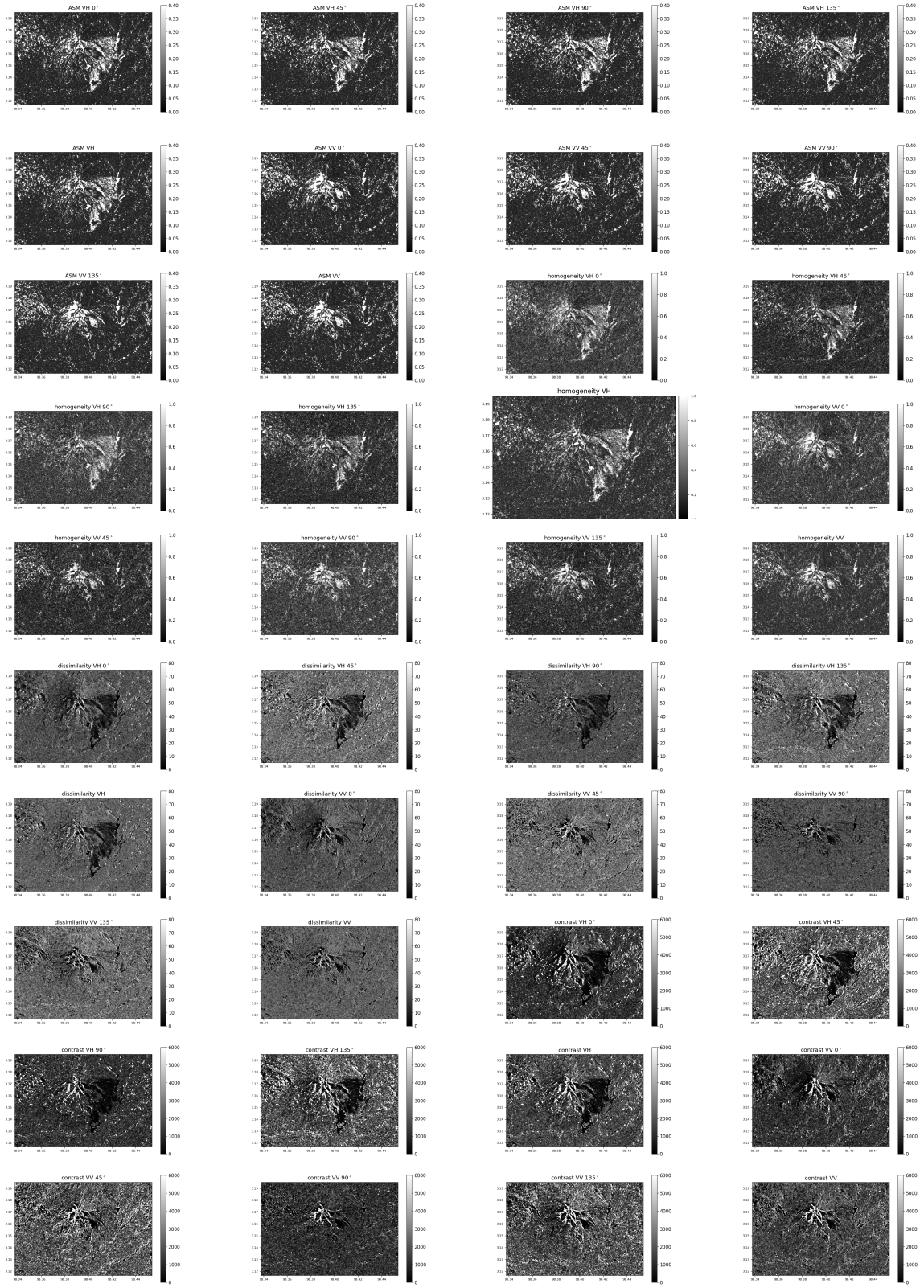

Figure C.2: Sinabung Case Study GLCM feature maps.

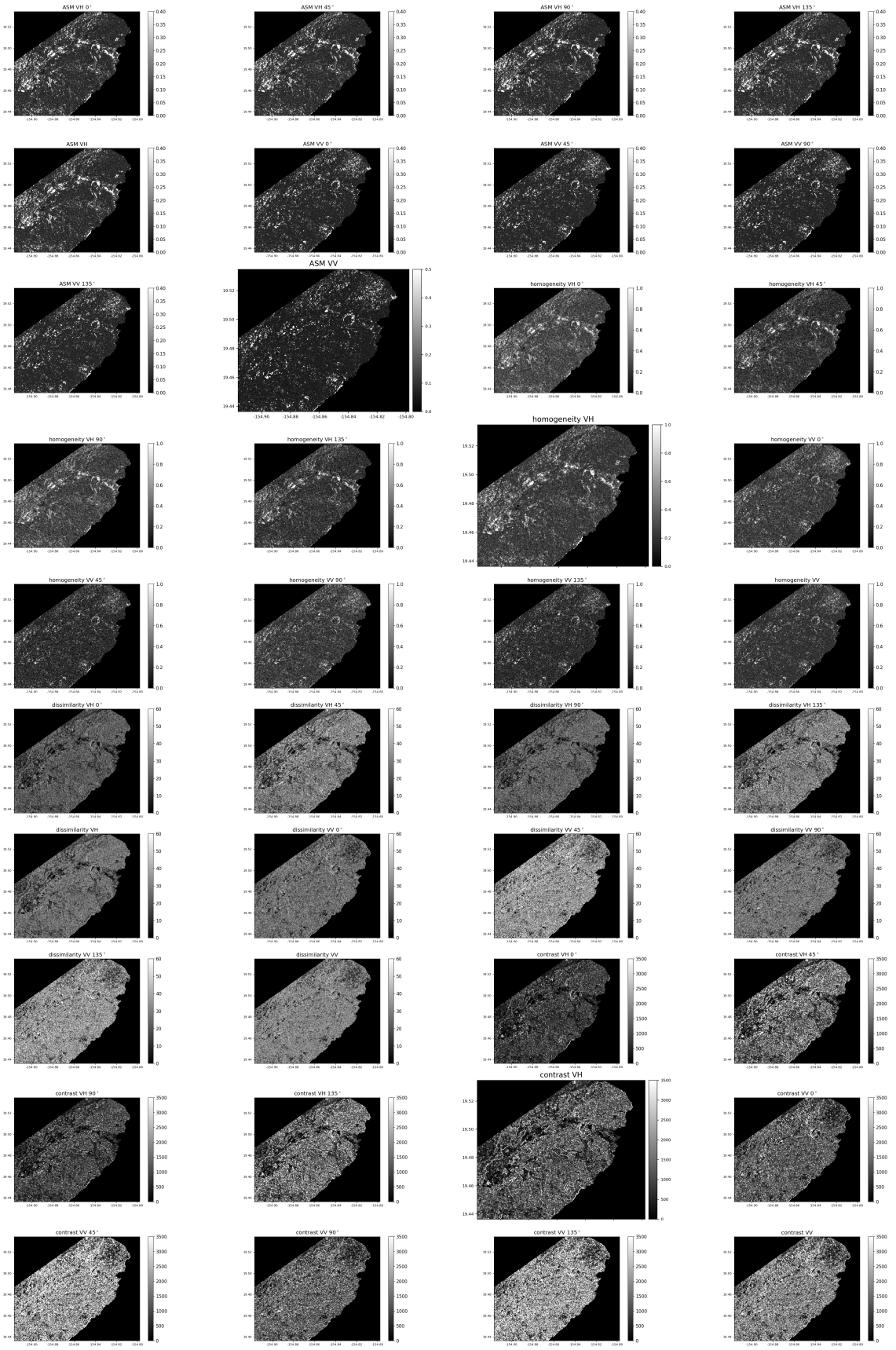

Figure C.3: Kilauea Case Study GLCM feature maps.

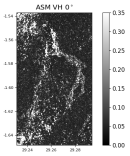
ASM VH 0°

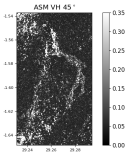
ASM VH 45°

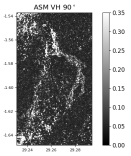
ASM VH 90°

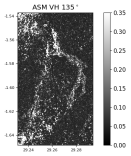
ASM VH 135°

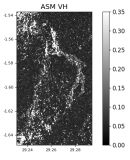
ASM VH

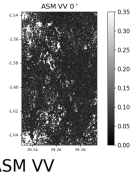
ASM VV 0°

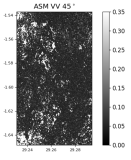
ASM VV 45°

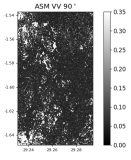
ASM VV 90°

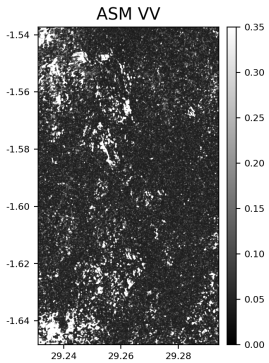
ASM VV
-1.54
-1.56
-1.58
-1.60
-1.62
-1.64
29.24
29.26
29.28
0.35
0.30
0.25
0.20
0.15
0.10
0.05
0.00

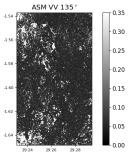
ASM VV 135°

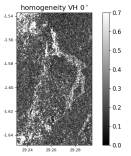
homogeneity VH 0°

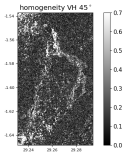
homogeneity VH 45°

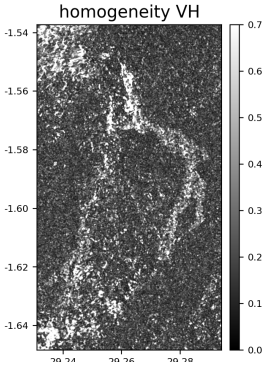
homogeneity VH
-1.54
-1.56
-1.58
-1.60
-1.62
-1.64
0.7
0.6
0.5
0.4
0.3
0.2
0.1
0.0

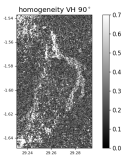
homogeneity VH 90°

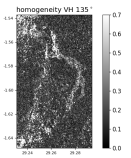
homogeneity VH 135°

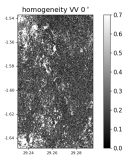
homogeneity VV 0°

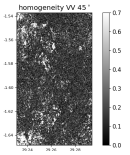
homogeneity VV 45°

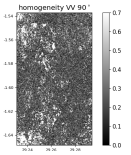
homogeneity VV 90°

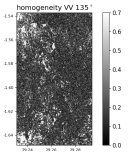
homogeneity VV 135°

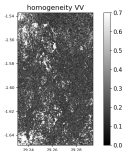
homogeneity VV

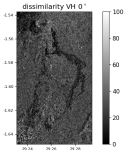
dissimilarity VH 0°

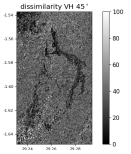
dissimilarity VH 45°

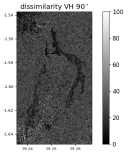
dissimilarity VH 90°

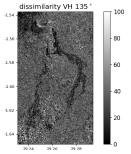
dissimilarity VH 135°

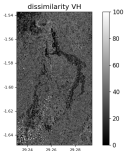
dissimilarity VH

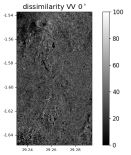
dissimilarity VV 0°

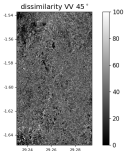
dissimilarity VV 45°

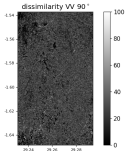
dissimilarity VV 90°

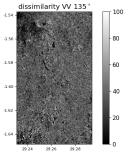
dissimilarity VV 135°

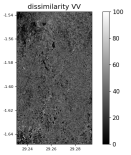
dissimilarity VV

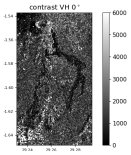
contrast VH 0°

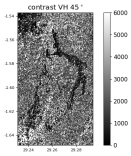
contrast VH 45°

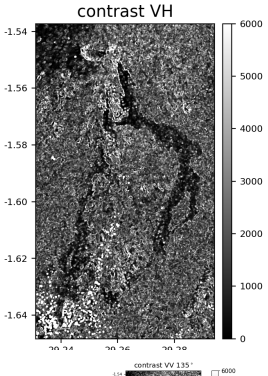
contrast VH
-1.54
-1.56
-1.58
-1.60
-1.62
-1.64
6000
5000
4000
3000
2000
1000
0

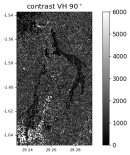
contrast VH 90°

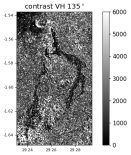
contrast VH 135°

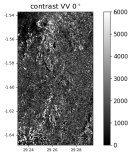
contrast VV 0°

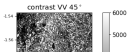
contrast VV 45°

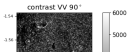
contrast VV 90°


contrast VV 135°

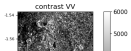
contrast VV